Functional Magnetic Resonance Spectroscopy (fMRS) for the Investigation of Brain Metabolism during Neural Activation at 3T and 7T

DISSERTATION
zur Erlangung des akademischen Grades
Dr. rer. nat.

an der Medizinischen Fakultät
der Universität Leipzig

eingereicht von:
Master of Science (M.Sc.) Miguel Martínez Maestro

angefertigt an / in:
Max Planck Institut für Kognitions- und Neurowissenschaften, Leipzig

Betreuer:
Prof. Dr. Hellmuth Obrig
Prof. Dr. Harald E. Möller

Beschluss über die Verleihung des Doktorgrads vom:
19. März 2019

Contents

Figures

Tables

Abbreviations and Symbols

^{1}H	hydrogen nucleus (proton)
[X]	concentration of compound X;
$[X]_0$	baseline concentration of compound X;
Δ[X]	concentration change of compound X.
20-HETE	20-hydroxyeicosatetraenoic acid
2D	two-dimensional
3D	three-dimensional
AA	arachidonic acid
AFP	adiabatic full passage
Ala	alanine
AMPA	α-amino-3-hydroxy-5-methyl-4-isoxazole propionic acid
Asp	aspartate
ATP	adenosine triphosphate
$\boldsymbol{B}_0$	external magnetic field
$\boldsymbol{B}_1$	time-varying magnetic field
$\boldsymbol{B}_e$	effective magnetic field in the frequency frame
$\boldsymbol{B}'_e$	effective magnetic field in the rotaing frame
BOLD	blood oxygenation level dependent
ΔBOLD	percent BOLD signal change
CBF	cerebral blood flow
CBV	cerebral blood volume
cGMP	cyclic guanosine monophosphate
CHESS	Chemical Shift Selective
CMR_{Glc}	cerebral metabolic rate of glucose
CMR_{O2}	cerebral metabolic rate of oxygen
Cr	creatine
CRLB	Cramér-Rao lower bound
CSDA	chemical shift displacement artifact
δ	chemical shift
$\Delta\nu$	frequency shift in Hz
dHb	deoxygenated hemoglobin
EAAT	excitatory amino acid transporters
ECS	extracellular space
EEG	electroencephalography
EET	epoxyeicosatrienoic acid

EP4	prostaglandin E2 receptor 4
EPI	Echo-Planar Imaging
ER	endoplasmic reticulum
FA	pulse flip angle;
FAST(EST)MAP	Fast Automatic Shim Technique using Echo-planar Signal readouT for Mapping Along Projections
FASTMAP	Fast Automatic Shimming Technique by Mapping Along Projections
FID	free induction decay
fMRI	functional magnetic resonance imaging
fMRS	functional MRS
FOV	field of view
FWHM	full width at half maximum
GABA	γ-aminobutyric acid
γ	gyromagnetic ratio
Glc	glucose
Gln	glutamine
Glu	glutamate
Gly	glycine
GPC	glycerophosphocholine
GRAPPA	GeneRalized Autocalibrating Partially Parallel Acquisitions
GRE	gradient-recalled echo
GSH	glutathione
h	Planck constant
i	imaginary unit;
I	spin quantum number
k	Boltzmann constant
L	angular momentum
Lac	lactate
LASER	Localization by Adiabatic SElective Refocusing
LONG	long blocks (32 seconds) visual stimulation paradigm
$\boldsymbol{M}$	net macroscopic magnetization
$\boldsymbol{M}_0$	macroscopic magnetization vector
Mr	residual magnetization
MEG	magnetoencephalography
MET	water-suppressed acquired spectrum
mGluRs	metabotropic glutamate receptors
mI	*myo*-inositol
MP2RAGE	Magnetization-Prepared 2 RApid Gradient Echoes
MR	magnetic resonance
MRI	magnetic resonance imaging

MRS	magnetic resonance spectroscopy
$\boldsymbol{\mu}$	magnetic moment
n	number of cases
n_{ch}	number of RF receive channels
n_{rep}	number of repetitions
n_t	number of time points
NAA	*N*-acetylaspartate
NAAG	*N*-acetylaspartatyl glutamate
NAD	nicotinamide adenine dinucleotide
NAD^+	oxidized form of NAD
NADH	reduced form of NAD
NBR	negative BOLD response
NMDA	*N*-methyl-D-aspartate
NMDAR	*N*-methyl-D-aspartate receptors
NMR	nuclear magnetic resonance
nNOS	neuronal nitric oxide synthase
NO	nitric oxide
p	error probability
PBR	positive BOLD response
PBS	phosphate-buffered saline
PCh	phosphocholine
PCr	phosphocreatine
PFC	prefrontal cortex
PGE2	prostaglanding E2
φ_{wat}	phase of the water unsuppressed spectrum
PLA2	phospholipase A2
PRESS	Point REsolved Spectroscopy
R	pearson correlation coefficient
REST	rest periods of the visual stimulation paradigm
RF	radiofrequency
S	time domain signal amplitude
S_0	original signal amplitude;
S_{ecc}	eddy current-corrected signal amplitude;
S_{fc}	frequency-corrected signal amplitude;
sGC	soluble guanylate cyclase
SHORT	short blocks (32 seconds) visual stimulation paradigm
SMC	smooth muscle cells
SNR	signal-to-noise ratio
STEAM	Stimulated Echo Acquisition Mode

STIM	stimulation peridos of the visual stimulation paradigm
SVD	singular value decomposition
T	absolute temperature
T1	spin-lattice longitudinal relaxation time
T2	spin-spin transverse relaxation time
T2*	effective transverse relaxation time
TA	acquisition time
τ	interpulse delay
τ_p	pulse length
Tau	taurine
TCA	tricarboxylic acid
tCh	total choline
tCr	total creatine
TE	echo time
θ	nutation angle
TI	inversion time
TM	delay between the 2nd and 3rd RF pulses on the STEAM sequence
TR	repetition time
uSHORT	32/4 seconds REST/STIM visual stimulation paradigm
V1	primary visual cortex
VAPOR	VAriable pulse POwer and optimized Relaxation delays
VOI	volume of interest
WAT	non-water-suppressed acquired spectrum
WET	Water suppression Enhanced through T1 effects

Chapter 1

Introduction

1.1 Background

Understanding brain function has been a challenge for more than 100 years (Lisman 2015; Di Salle et al. 1999). Applications today range from Cognitive Neuroscience to Medical Sciences (Faro and Mohamed 2007). Magnetic resonance (MR) techniques provide structural, functional and metabolic information of a tissue or organ of interest non-invasively, as well as information on how they interrelate (Mekle et al. 2017; Logothetis 2008) allowing the identification of biomarkers of normal and pathological brain states (Öz et al. 2014).

Blood oxygenation-level dependent (BOLD) functional magnetic resonance imaging (fMRI) is the most widely used method for studying human brain activity (Logothetis 2002) although its physiological and biomolecular basis is still not well understood (Attwell et al. 2010; Girouard and Iadecola 2006; Logothetis 2010; Sirotin and Das 2009). Understanding how changes in neural activity alter hemodynamics is crucial for a meaningful interpretation of fMRI results (Logothetis and Wandell 2004).

Magnetic resonance spectroscopy (MRS) methodologies are sensitive to different aspects of neuronal activation and provide complementary tools for investigating the human brain at work. In recent years, several functional MRS

(fMRS) studies have been performed to characterize the relationship between neuronal activation and energy or neurotransmitter metabolism.

1.2 Purpose and structure of this thesis

The main objectives of this dissertation are: 1) to identify the brain metabolic changes happening during brain activation and deactivation, and 2) to characterize the limits of detection of those changes in terms of duration and kind of stimulus, and field strength and acquisition protocol used.

The outline of this thesis, after the introductory **Chapter 1**, is as follows:

Chapter 2 and **Chapter 3** describe the physical, biochemical and physiological background. The physical principles of nuclear magnetic resonance (NMR), magnetic resonance imaging (MRI) and spectroscopy (MRS) and the state of the art of brain molecular mechanisms during activation are briefly discussed.

Chapter 4 explains the methods used for the acquisition, post-processing and analysis of the MRS experiments, and the imaging techniques used. The increased sensitivity at higher fields improves the detection of very subtle metabolic changes, after addressing a set of challenges as $\boldsymbol{B}_0$ and $\boldsymbol{B}_1$ inhomogeneities and the Chemical Shift Displacement Artifact (CSDA).

Chapter 5 performs a detailed study of the variances between different length of stimuli (32 seconds and 5 minutes) and different field strength (3 T and 7 T).

Chapter 6 explores the limits of detection of fMRS during short periods of stimulation (4 seconds) by applying a novel periodic averaging technique.

Chapter 7 presents the dynamic metabolic changes found on regions of neuronal activation and deactivation.

Chapter 8 contains the summary and general conclusion.

Chapter 2

Physical Background

2.1 Physical principles of NMR and MRS

Some isotopes of chemical elements are said to be magnetically active because they have magnetic moment, i.e. can behave as small magnets and their energy state can be altered when placed on an external magnetic field. Nuclear magnetic resonance (NMR) is a technique based on the resonance (i.e. matching) effect between the Larmor frequency (explained below) of those magnetically active atomic nuclei and of a magnetic field. The nucleus of the most abundant isotope of Hydrogen, ^{1}H, is compound of a single proton and is magnetically active. That makes ^{1}H-NMR a very convenient technique for non-invasively imaging living organisms, since the major compound is water and lipids, rich in hydrogen. E.g. on the human brain, a 1 μL volume can have up to 6×10^{19} hydrogen protons. Also, because the basic skeleton of biomolecules consists of chains of carbon and hydrogen, ^{1}H-MRS is the most used modality in NMR spectroscopy for detecting and quantifying metabolites *in vivo.*

The NMR phenomenon can be explained in two ways: the classical description based on the observations of Bloch (Bloch, Hansen, and Packard 1946) and the spectroscopic or quantum mechanical based on the discoveries of Purcell (Purcell, Torrey, and Pound 1946).

2.1.1 The quantum mechanical description

The angular momentum $\boldsymbol{L}$ associated to a spin is a quantum mechanical quantity and its magnitude is described by:

$$L = \left(\frac{h}{2\pi}\right)\sqrt{I(I+1)} \quad [1]$$

where I is the spin quantum number and h the Planck constant.

And the component of $\boldsymbol{L}$ on the z direction is:

$$L_z = \left(\frac{h}{2\pi}\right)m \quad [2]$$

where m can have $2I+1$ values (I, I-1, I-2, … - I) and is, therefore, quantized.

For protons, neutrons and electrons $I = \frac{1}{2}$. For nuclei of:

- odd mass number I is a half integral ($\frac{1}{2}$, $\frac{3}{2}$, $\frac{5}{2}$…)
- even mass number and even charge number I = 0
- even mass number and odd charge number I is an integer (1,2…)

Elementary particles also have a magnetic moment $\boldsymbol{\mu}$ related to the angular momentum $\boldsymbol{L}$ by:

$$\boldsymbol{\mu} = \gamma \boldsymbol{L} \quad [3]$$

where γ is the gyromagnetic ratio.

The magnetic moment $\boldsymbol{\mu}$ is therefore also quantized and its component along the z axis is:

$$\mu_z = \gamma\left(\frac{h}{2\pi}\right)m \quad [4]$$

In the presence of an external applied magnetic field $\boldsymbol{B}_0$ the nuclear spins acquire a magnetic energy given by:

$$E = -\boldsymbol{\mu}\boldsymbol{B}_0 \quad [5]$$

That for the $\boldsymbol{\mu}_z$ component of $\boldsymbol{\mu}$ is:

$$E = -\mu_z B_0 = -\gamma\left(\frac{h}{2\pi}\right)mB_0 \quad [6]$$

Because the protons have a quantum spin number of I = $\frac{1}{2}$, the nuclei distribute themselves into two energy states: parallel or anti-parallel to the applied magnetic field, i.e. m = $\frac{1}{2}$ or m = $-\frac{1}{2}$. And the energy difference ΔE between the two energy states is given by:

$$\Delta E = \gamma\left(\frac{h}{2\pi}\right)B_0 \quad [7]$$

From equation [7] can be seen that the separation between energy levels is proportional to the strength of the applied magnetic field **(Figure 1)**. The intensity of the signal increases with the strength of the field because two reasons:

a) The increase in energy separation between the two states
b) The increase in the number of nuclei in the lower energy state that can be excited to the higher energy state

A Radio Frequency (RF) pulse is a secondary magnetic field, which we can refer to as $\boldsymbol{B}_1$, that is applied for a finite time and turned off again (that is why it is called pulse) and oscillates in the radio frequency range (MHz). The condition of "resonance" occurs when an RF pulse oscillating at a frequency ν that exactly matches the energy separation between the two energy levels is applied. At this moment nuclei in the lower energy level absorb this energy and are promoted to the higher level. The energy of the applied pulse corresponds to:

$$\Delta E = h\nu \quad [8]$$

So, combining equations [7] and [8] the **Larmor equation** can be obtained:

$$\nu = \frac{\gamma}{2\pi} B_0 \qquad [9]$$

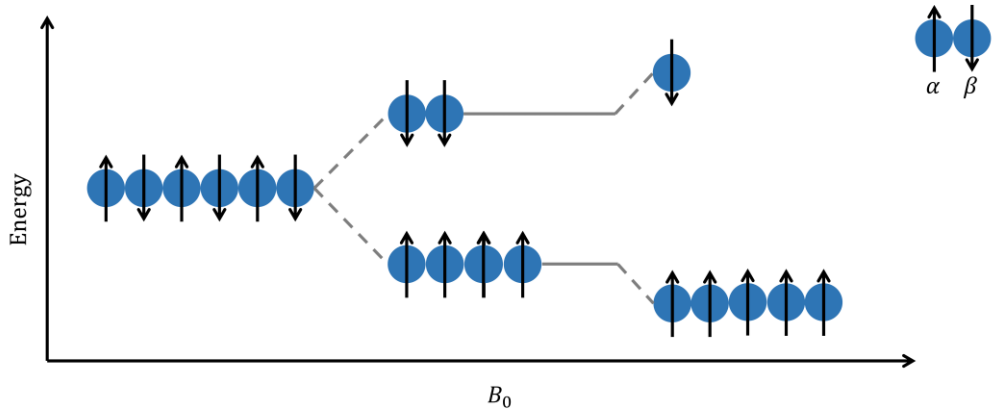

Figure 1: The energy difference between magnetic energy levels increases with an increase in magnetic field (equation [7]). The number of spins that adopt an energetically lower α orientation (parallel to B_0) over a β orientation (antiparallel to B_0) also increases.

2.1.2 The classical description

Nuclei with a non-zero spin possess a magnetic moment $\boldsymbol{\mu}$, which makes them behave as small magnets. Consider the hydrogen nuclei present in the human brain. In the absence of an external magnetic field their $\boldsymbol{\mu}$ will be randomly oriented, resulting in no net macroscopic magnetization. In the presence of an external magnetic field, each of the nuclear spins start to precess with a frequency called the Larmor Frequency (equation [9]). The gyromagnetic ratio γ (megahertz per tesla) is unique for that nuclear spin.

Let's consider that, on a Cartesian frame of reference, the external field $\boldsymbol{B}_0$ is applied parallel to the +z axis. The spins orient either parallel (lower energy state) or antiparallel (higher energy state) to the applied magnetic field. The number of spins that is oriented parallel is slightly higher than the spins oriented

anti-parallel. On the xy plane no net macroscopic magnetization is found because each individual spin has a different phase. And on the +z axes, a small net macroscopic magnetization is found, corresponding to the small fraction (on the order of one in a million) of spins that are preferentially oriented parallel to $\boldsymbol{B}_0$.

At thermal equilibrium, the magnitude of the macroscopic magnetization vector $\boldsymbol{M}_0$ is:

$$M_0 = \left(\frac{\gamma h}{2\pi}\right)^2 \left(\frac{nB_0}{4kT}\right) \qquad [10]$$

where h is the Planck constant, n the total number of spins of our sample, k is the Boltzmann constant and T the absolute temperature. Some characteristics of NMR experiments can be deduced from equation [10]:

Nuclei with a higher γ generate more intense NMR signals.

Higher magnetic fields improve the sensitivity.

Lower temperature increase sensitivity (not an option *in vivo*).

2.1.2.1 T1, T2 AND T2* RELAXATION

The net macroscopic magnetization $\boldsymbol{M}_0$ at equilibrium is a static vector. To observe nuclear magnetization, the precessional motion needs to be detected. For that, the net macroscopic magnetization needs to be flipped into the xy transverse plane, so the precessing magnetization can induce a signal (Free Induction Decay, FID) in a receiver coil thanks to Faraday's law of induction. The strength of the induced NMR signal is determined by the magnitude of $\boldsymbol{M}_0$ (equation [2]). To flip the magnetization into the transverse plane, a Radio Frequency (RF) pulse needs to be applied. If a $\boldsymbol{B}_1$ that matches the Larmor frequency of the net macroscopic magnetization at equilibrium $\boldsymbol{M}_0$ is applied perpendicular to $\boldsymbol{B}_0$, there will be a net macroscopic magnetization $\boldsymbol{M}$ precessing about $\boldsymbol{B}_0$ and $\boldsymbol{B}_1$, i.e. $\boldsymbol{M}$ will rotate towards the transverse plane due to $\boldsymbol{B}_1$ while precessing about $\boldsymbol{B}_0$ at the Larmor frequency. Depending on the duration and the amplitude of the applied RF pulse,

$\boldsymbol{M}$ will be flipped in the transverse plane xy (90°) or completely inverted into the -z axis (180°). When $\boldsymbol{B}_1$ is switched off, $\boldsymbol{M}$ goes back to the position at equilibrium precessing around $\boldsymbol{B}_0$ at the Larmor frequency.

In the presence of $\boldsymbol{B}_0$ and $\boldsymbol{B}_1$ the magnetization $\boldsymbol{M}$ in the absence of relaxation can be expressed as:

$$\frac{d\boldsymbol{M}(t)}{dt} = \boldsymbol{M}(t) \times \gamma \boldsymbol{B}(t) \quad [11]$$

Where $\boldsymbol{B}$ includes $\boldsymbol{B}_0$ and the time-varying component $\boldsymbol{B}_1$. That can be expanded in the static laboratory frame of reference to:

$$\frac{dM_x(t)}{dt} = \gamma[M_y(t)B_0 - M_z(t)B_{1y}] \quad [12]$$

$$\frac{dM_y(t)}{dt} = \gamma[M_z(t)B_{1x} - M_x(t)B_0] \quad [13]$$

$$\frac{dM_z(t)}{dt} = \gamma[M_x(t)B_{1y} - M_y(t)B_{1x}] \quad [14]$$

Relaxation is the process of return to thermal equilibrium after a perturbation. The perpendicular ($\boldsymbol{M_x}$ and $\boldsymbol{M_y}$) and parallel ($\boldsymbol{M_z}$) to $\boldsymbol{B}_0$ components of $\boldsymbol{M}$ relax with different time constants. Including the relaxation terms on equations [12],[13] and [14]:

$$\frac{dM_x(t)}{dt} = \gamma\left[M_y(t)B_0 - M_z(t)B_{1y}\right] - \frac{M_x(t)}{T2} \quad [15]$$

$$\frac{dM_y(t)}{dt} = \gamma[M_z(t)B_{1x} - M_x(t)B_0] - \frac{M_y(t)}{T2} \quad [16]$$

$$\frac{dM_z(t)}{dt} = \gamma\left[M_x(t)B_{1y} - M_y(t)B_{1x}\right] - \frac{(M_z(t) - M_0)}{T1} \quad [17]$$

T1 is the longitudinal (or spin-lattice) relaxation time constant. It describes the return of longitudinal magnetization to equilibrium after a perturbation. If an RF pulse that flips $\boldsymbol{M}$ into the transverse plane is applied, the amplitude of the component of $\boldsymbol{M}$ along the z axis M_z is equal to 0 at a time t = 0 (right after the RF pulse is stopped). Immediately after, as $\boldsymbol{M}$ comes back to its orientation at equilibrium (parallel to $\boldsymbol{B}_0$) there is an increase of M_z defined by T1 by the equation:

$$M_z(t) = M_0(1 - e^{-\frac{t}{T1}}) \quad [18]$$

T2 is the transversal (or spin-spin) relaxation time constant. It describes the decay of transverse magnetization. The net macroscopic magnetization perpendicular to $\boldsymbol{B}_0$ that is generated when a 90° RF pulse is applied, happens because individual spins acquired phase coherence. When $\boldsymbol{B}_1$ is switched off, spins start to dephase and the transversal component of $\boldsymbol{M}$, M_{xy} decreases according to:

$$M_{xy}(t) = M_{xy}(0)e^{-\frac{t}{T2}} \quad [19]$$

T2 is the transversal relaxation time for a homogeneous field. The time constant that includes dephasing due to field inhomogeneities is T2*.

T1 and T2 relaxation times reflect the tissue environment, i.e. the binding and mobility of water within tissues and are responsible for most contrast in MR images.

2.1.3 Imaging

By convention, the main magnetic field, $\boldsymbol{B}_0$, is aligned with z (usually along the bore of the magnet). A field gradient along x means that the strength of the magnetic field varies with position along x.

The addition of a magnetic field gradient **G** to the static magnetic field $\boldsymbol{B}_0$, generates a total magnetic field at position **r** given by:

$$\boldsymbol{B}(\boldsymbol{r}) = \boldsymbol{B}_0 + \boldsymbol{r} \cdot \boldsymbol{G} \qquad [20]$$

The scanner hardware can create gradients in x, y, and z directions. If the field increases linearly with position, the resonant frequency increases also linearly with position (equation [20]), allowing to use the frequency to spatially encode the signal.

Creating an image requires encoding of spatial positions in 3 dimensions:

Slice selection. When a shaped RF pulse, typically sinc, is applied in the presence of a gradient, only a specific section (slice) of the sample being imaged resonates at a frequency that matches the bandwidth of the RF pulse and is excited.

Frequency Encoding. If a readout gradient is applied during data acquisition, spins at different positions experience slightly different local fields and therefore precess at different rates. The resulting signals have different frequencies and can be disentangled using a Fourier Transform.

Phase Encoding. As for the frequency encoding, the application of a gradient before data acquisition (phase encoding gradient) makes spins at different positions experience slightly different local fields and, thus, precess at different rates leading to a spatially dependent phase.

Signals are received on a receiver coil after inducing an echo (spin echo or gradient echo). **Spin Echo** is the basis for many structural images. An initial 90° pulse can flip the equilibrium magnetization from the +z axis perpendicularly into the xy plane, along the +y axis. Due to field inhomogeneities and T2 and T2* relaxation, spins start to dephase on the xy plane. A second RF pulse, now of 180°, flips all spins into the -y axes. This process rewinds the phases, so the spins will eventually rephase and form a net magnetization along the -y direction, at a time

TE (echo time). Immediately spins start to dephase again, and the FID can be recorded. In the case of a **gradient echo,** a gradient is applied to manipulate the dephasing of the spins when flipped into the xy plane. If the gradient is then reversed, the spins rephase forming an echo. Gradient echo-based sequences are used for structural and functional imaging.

The repetition time or TR is the time between the application of the first excitation pulse in a sequence, and the successive one (for signal averaging, or for collecting the next phase encoding step). Different combinations of TE and TR can be used to produce different degrees of contrast (intensity difference) between tissues; changes of TR lead to different contrasts between tissues with different T1 relaxation times, and changes in TE to different contrasts between tissues with different T2.

2.1.4 Electronic shielding and chemical shift

The **Larmor frequency equation** (equation [9]) states that the resonance frequency of a magnetic nuclei (the radiofrequency needed to excite a given nuclei) is directly proportional to the magnetic field applied. Different nuclei resonate at different Larmor frequencies, but even for a given magnetic nuclei chemical compounds containing it can have slightly different Larmor resonance frequencies as the result of the electron cloud that surround them.

Let's consider a nuclear spin. The applied $\boldsymbol{B}_0$ field and the effective field that the nucleus experiences are identical, leading to a certain Larmor frequency. If an RF pulse that matches this Larmor frequency is applied, this nucleus will be excited, and its net macroscopic magnetization flipped into the xy transverse plane. The precessing magnetization about the z-axis will induce a signal (FID) in a receive coil. That signal corresponds to an exponential decay on the Time Domain (according to T2 and T2* relaxation as in equation [19]). A Fourier

transformation of this signal gives a Lorentzian peak resonating at the Larmor Frequency on the Frequency Domain or spectrum.

However, the nuclear spin is not isolated. It has electrons surrounding it that will produce a magnetic field $\boldsymbol{B}'$ in the opposite direction to the external magnetic field $\boldsymbol{B}_0$. This effect is called **electronic shielding**. The effective field $\boldsymbol{B}_e$ that our nucleus experiences is therefore lower, the Larmor frequency is lower, and the peak appears at a lower frequency on the spectrum. The magnitude of $\boldsymbol{B}'$ and in consequence the magnitude of the effective field $\boldsymbol{B}_e$ ($B_e = B_0 - B'$) that our nucleus will feel depends on the chemical environment of the nucleus, referring to the chemical environment as the chemical group that the nuclei is being part of. Different molecules give rise to different peaks resonating at different Larmor frequencies. This phenomenon is called the **chemical shift** and is the basis of MRS.

To illustrate this with an example we can think of the lactate molecule. Lactate is an important metabolite of cellular energetics in general and brain energetics in particular and can be detected with *in vivo* MRS. The molecule consists of a carboxyl, a hydroxyl and a methyl group **(Figure 2).** The possible proton resonances correspond to the proton of carbon 2 and the 3 protons of carbon 3. The electrons surrounding the carbon 2 are pulled by the nearby oxygen atoms (while the electrons of carbon 3 are not affected by this). Therefore, the chemical shielding on the proton of carbon 2 is smaller than the chemical shielding on the protons of carbon 3. As a result, the effective field that experiences the proton of carbon 2 is larger than the effective field that the protons of the carbon 3 experience, i.e. the protons of the methyl group resonate at a lower Larmor frequency than the proton bound to carbon 2. In conclusion, we observe 2 peaks for lactate, resonating at 127.500523 MHz and 127.500166 MHz at B_0 = 3 T, and 298.001201 MHz and 298.000387 MHz at 7 T.

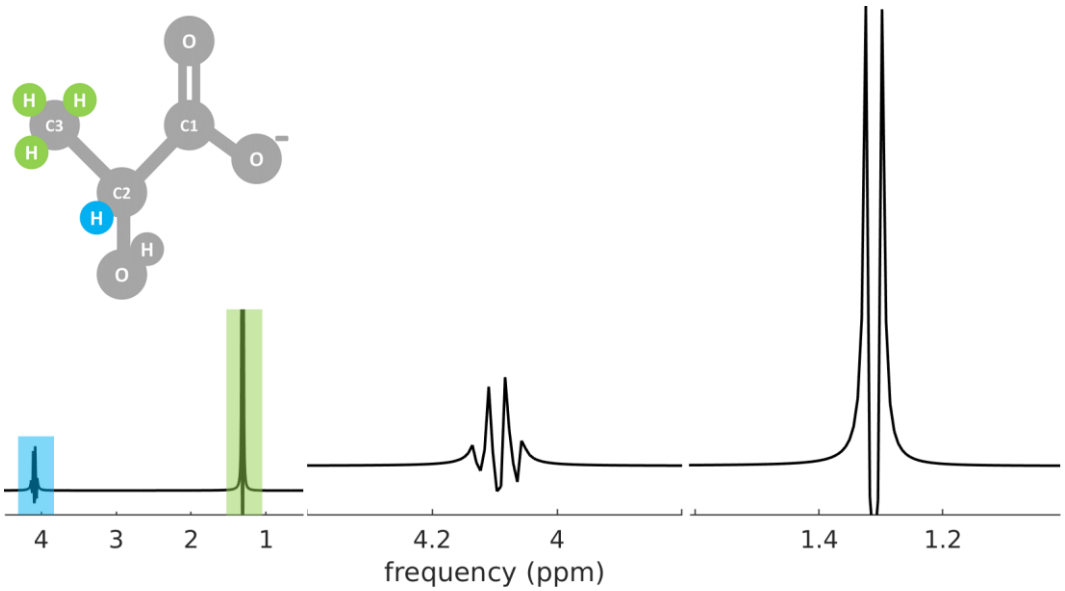

Figure 2: Chemical shift and splitting patterns of the lactate molecule. LEFT: The 3 protons of carbon 3 resonate at lower frequency (1.31ppm) than the proton of carbon 2 (4.10ppm). RIGHT: zooming into these peaks shows that they are actually a doublet and a quartet due to the J-coupling AX3 system. The peak at 4.1ppm splits 3 times due to the 3 protons of carbon 3, while the peak at 1.31ppm splits once due to the proton of carbon 2. Lactate spectrum simulated with the FID-A toolbox (https://github.com/CIC-methods/FID-A).

To have a frequency axis independent of the field strength, the units are conventionally converted to parts per million (ppm). To do that, a reference compound need to be chosen (e.g. N-acetyl-aspartate (NAA) at 2.01 ppm is a good reference *in vivo*) and the following formula is applied:

$$\delta(ppm) = \frac{\nu\,(MHz) - \nu_{reference}(MHz)}{\nu_{reference}(MHz)}\,10^6 \qquad [21]$$

On this new common axis, the two peaks of lactic acid appear now at 4.1 and 1.3 ppm, respectively. Being γ= 42,576 (MHz/T) the gyromagnetic ratio of 1H, the corresponding 1H Larmor frequencies and typical spectral acquisition bandwidth (needed to cover the full spectrum up to 8 ppm or more) at representative field strengths are on **Table 1**. The resolution (separation between

resonant peaks) increases linearly as the field strength increases, but the distance expressed in ppm remains constant.

$\boldsymbol{B_0}$	$\boldsymbol{\nu}$ *(MHz)*	*Bandwidth (Hz)*
1.5 T	63.864	600
3 T	127.728	1200
7 T	298.032	2800

Table 1: Larmor frequencies and typical spectral acquisition bandwidth (wide enough to cover a range from at least 0 to 8 ppm) at frequently used field strengths

2.1.5 Spin-spin coupling

Taking a closer look at the practical example of lactate, we can observe that the peak resonating at 1.31 ppm is actually a doublet and the peak resonating at 4.1 ppm is a quartet. The NMR resonance frequencies of the nuclei are influenced by the chemical environment and usually don't appear as a single peak but are splitted into several, due to what is called scalar coupling, J coupling or spin-spin coupling. Nuclei with magnetic moments influence each other through space (dipolar coupling) and through the electrons in the chemical bonds (scalar coupling). The first one average to zero in liquids and the second one leads to the scalar coupling phenomenon. Scalar coupling only operates to a limited number of chemical bonds, typically up to 3 or 4 bonds maximum, after that, the coupling is so weak that can be neglected.

Let's consider a set of ^{13}C nuclei resonating at a certain Larmor frequency, ν_c, that gives a single peak in the NMR spectrum. Assuming that this ^{13}C is chemically bound to a proton, which can be either in a spin state α (parallel to the external magnetic field $\boldsymbol{B}_0$) or β (antiparallel to the external magnetic field $\boldsymbol{B}_0$). If the proton is in the β state, it adds a small frequency to the Larmor frequency of the ^{13}C (ν_c+ J/2) however the α state substract the same small frequency (ν_c- J/2). In

conclusion, the ^{13}C of our example does not display a single peak on the NMR spectrum anymore, but a pair of peaks (each with half the intensity of the original theoretical single peak) at the frequencies ν_c+ J/2 and ν_c- J/2. These two peaks are separated by a constant frequency J that is the J coupling constant, and its independent of the external magnetic field $\boldsymbol{B}_0$ that is applied and characteristic of each pair of nuclei (C-H, H-H…). Similarly to how the proton splits up the peak of the ^{13}C, the ^{13}C splits the peak of the proton by the same J coupling constant.

This situation is only valid when the frequency difference between the two scalar-coupled spins is much larger than the scalar coupling between them, i.e. $|\nu_A - \nu_B| \gg J_{AX}$. When this condition is fulfilled, the two-spin AX spin system is called **weakly coupled** spin system and the spectrum it generates is called **first-order spectrum**. However, when $|\nu_A - \nu_B| \approx J_{AX}$ the spin system is **strongly coupled** and produces a **second-order spectrum**, whose characteristics cannot be explained with a classical description, but require density matrix calculations (Goldman 1988).

Two nuclei A and B with the same chemical shift δ coupled to a third nucleus C with a different chemical shift δ' are chemically equivalent (but not magnetically equivalent) if the scalar coupling constants that each has with the third nuclei are different, i.e. $J_{AC} \neq J_{BC}$ and magnetically and chemically equivalent (and chemically equivalent) if their J constant are the same, i.e. $J_{AC} = J_{BC}$. In light of this, the rules of the splitting patterns of first-order spectra can be explained as:

- Magnetically equivalent nuclei do not produce observable splitting.
- When there are more than two magnetic nuclei on a molecule, the pattern for a given nuclei can be explained by successive splitting. First, the condition $|\nu_A - \nu_B| \gg J_{AX}$ must occur between each pair in order to produce splitting. Nuclei with very close chemical shifts will not produce an observable effect. But when the splitting is

possible, e.g. on a system AMX with three sufficient separated nuclei in the spectrum A, M and X, the patterns consist of: A and X are splitted once based on the J constant that each one of them has with M, while M suffers two consecutive splittings, resulting in a "doublet-of-doublets" (four peaks of equal intensity).

- On a group with n equivalent nuclei (AX_n), the nucleus A is splitted n times. The distance between the peaks is the J_{AX} constant and their relative intensities follows a Pascal's pyramid. e.g. if n = 3, A is splitted 3 times and the relative intensities of the 4 peaks generated are 1 3 3 1. On the other hand, the signal that is produced by the n X nuclei, is splitted only once by A with the constant J_{AX}.

Back to the lactic acid spectrum, we have a AX_3 system. The proton at 4.1 ppm splits 3 times influenced by the three protons of the methyl group, while the resonance peak that is produced by the three protons of the methyl group is splitted once due to the J coupling from the proton of the carbon 2. Additionally, looking at the area under the curve of the peaks (i.e. the integral of the peaks) the total area under the 4 peaks of the quartet has a relative value of 1 (signal from a single proton) whereas the total area of the doublet has a relative value of 3 (signal from 3 protons), confirming the -CH next to the -CH3 group (**Figure 2**).

The more complicated splitting patterns of second-order spectra include:

- On an AB two-spin system, the relative intensity and frequency of resonance change.
- A "roof effect" appears (the relative intensities of the peaks increase towards the center of the spectrum, generating an imaginary roof if we would draw a line on top of the peaks at the left and another one on top of the peaks at the right).
- On a A_2B_2 four-spin system, additional resonances can appear.

2.2 Pulse sequences for single-voxel MRS

A voxel is a three-dimensional pixel. Single-voxel MRS means that only signal from a defined region of interest is being detected. For that purpose, selective RF pulses are needed. A sinc pulse gives an approximately squared frequency profile (**Figure 3**). When applied in the presence of a gradient, the selected range of frequencies excited (Δν) are related to a selective range of spatial positions Δx by the equation:

$$\Delta x = \frac{\Delta \nu}{\frac{\gamma}{2\pi} Gx} \qquad [22]$$

Which is the same principle that is used in MR imaging to obtain spatial localization. The intersection of three orthogonal slices gives as a result a cube (or rectangular prism) that is our MRS voxel.

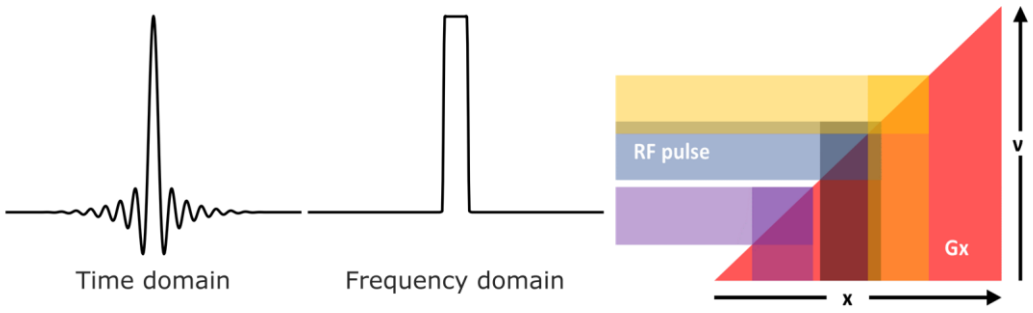

Figure 3: Slice selection with a sinc pulse and Chemical Shift Displacement Artifact (CSDA). An RF pulse with a sinc shape (LEFT) in the time domain has a rectangular shape (CENTER) in the frequency domain after Fourier transformation. Applied in the present of a gradient excite the spins of a specific spatial position (RIGHT, equation [22]). In the spectrum, that occurs only for the peaks resonating at the specific frequency of the RF pulse (RIGHT, blue band). For the peaks resonating at slightly higher or lower frequency, the signal will be taken from slightly shifted spatial positions from where our voxel was initially placed (RIGHT, purple and yellow bands).

However, by this principle, our voxel will be only on the desired spatial position for the compound that resonates at the same frequency as the frequency of the applied RF pulse. For the rest of components of our spectrum, resonating at

higher or lower frequencies, the voxel will be slightly shifted **(Figure 3).** This is called **chemical shift displacement artifact (CSDA).** Since the chemical shift (the separation between resonance peaks) increases linearly with the external magnetic field $\boldsymbol{B}_0$, the CSDA is more severe at higher fields. Some solutions to minimize this artifact are to increase the gradient strength or RF pulse bandwidth or use 90° pulses instead of 180° pulses if possible, since the bandwidth of a 90° pulse is larger.

2.2.1 PRESS

The Point RESolved Spectroscopy (PRESS) sequence (Bottomley 1987) consists of a slice selective excitation pulse (90° or $\frac{\pi}{2}$ in radians) followed by two slice-selective refocusing pulses (180° or π, **Figure 4**). The application of these three pulses together with three gradients perpendicular between them, induce the formation of a spin echo while spatially selecting our volume of interest (VOI). According to the classical model that considers the magnetic moments as vectors, PRESS acquisition can be described as follows (**Figure 4**):

At the beginning, the magnetic moments of the spins of an object placed in the scanner are aligned towards the z axis. When the first excitation pulse is applied they are flipped into the xy plane. Once on the xy plane they start to de-phase after a certain time until a 180° refocusing pulse is applied, so they re-phase and form the first echo. This echo contains signal from a column that is the intersection of two slices. The spins de-phase again to be again re-focused by the application of the second 180° pulse. Therefore, the second echo will contain signal from the desired voxel. The signal outside the voxel is nor excited, nor refocused, leading to rapid de-phasing of signal by the 'crusher' gradients surrounding the 180° refocusing pulses. The decaying signal that is acquired is the 'de-phasing' echo: all spins converged together after the second 180° pulse that start to de-phase faster or slower according to their T2 constants.

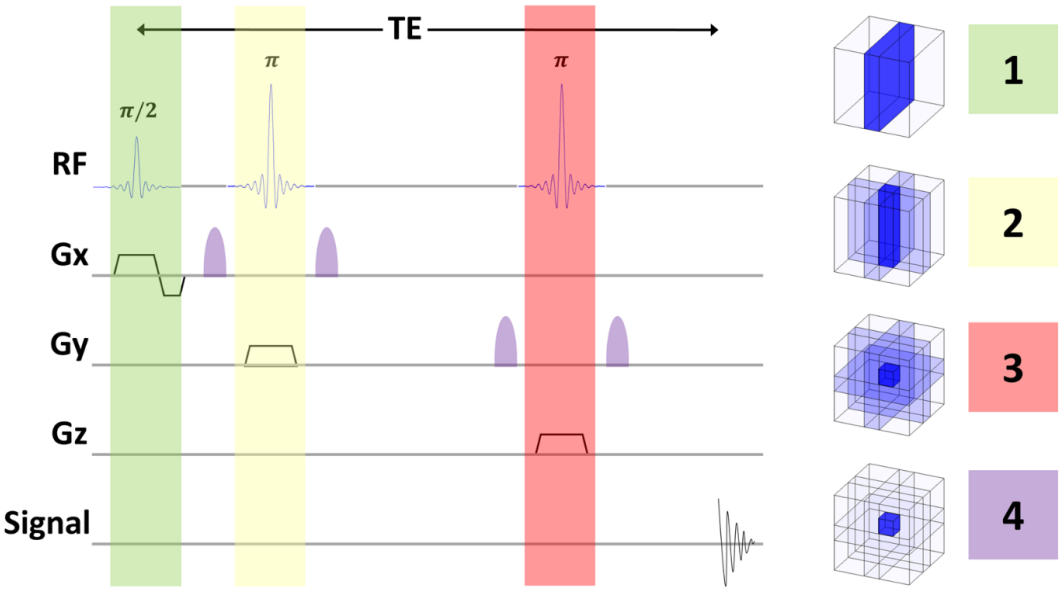

Figure 4: PRESS sequence diagram and rectangular single voxel selection.

2.2.2 STEAM

The Stimulated Echo Acquisition Mode (STEAM) sequence (Frahm et al. 1989) uses the same principle of orthogonal gradients as PRESS for the selection of the volume of interest, but the echo formation occurs differently (**Figure 5**). In this case, three consecutive 90° pulses create a stimulated echo. As it can be seen in **Figure 5**, the first part would occur exactly as in PRESS. Spins will start dephasing following the application of the first 90° pulse that flipped them into the xy plane. But now, a second 90° pulse flips them again into the zx plane. At this step, T1 relaxation occurs with a resulting net growth in components along the z-axis. The third 90° pulse flips the z-components back into the transverse xy plane. There, the magnetization is re-focused forming the stimulated echo, which is only half of the initially excited magnetization because the rest was not in the longitudinal axis before the third 90° pulse was applied.

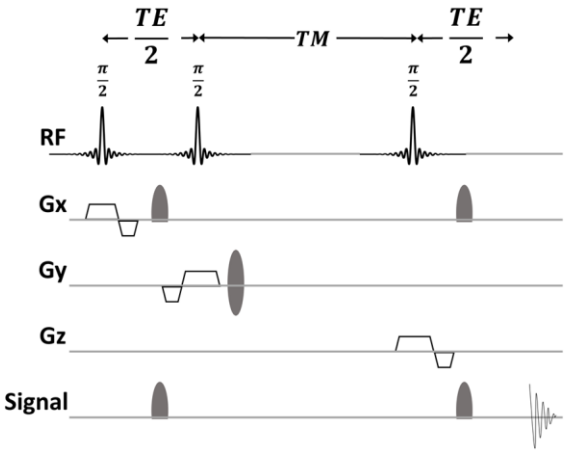

Figure 5: STEAM sequence diagram.

The theoretical SNR of PRESS is twice the SNR of STEAM. However, STEAM allows shorter TEs (important for quantification of metabolites with very short T2) and higher flexibility for extensions during the TM. This flexibility can be used for a more effective water suppression, for example. Another advantage of STEAM is that 90° pulses lead to a better slice profile than 180° and the CSDA is lower.

2.2.3 (semi) LASER

2.2.3.1 THE ADIABATIC CONDITION

For an excitation, the nutation or flip angle is proportional to the RF amplitude (B_1):

$$\theta = \gamma B_1 \tau_p \qquad [23]$$

where τ_p is the pulse length.

An adiabatic pulse is a frequency (or phase) modulated pulse that generate a uniform nutation angle independent of the RF amplitude.

The cartesian xyz frame of reference is usually called static or laboratory frame of reference. Let's consider a frame of reference x'y'z' rotating along the z' with a frequency that varies as a function of time and we call frequency frame. $\boldsymbol{B}_1$ (t) does not precess in the transverse plane but has a constant orientation (e.g. along x'). The frequency of the adiabatic pulse, $\omega(t)$, deviates from the Larmor frequency ($2\pi\upsilon_0$ or ω_0) as a function of time. The effective magnetic field $B_e(t)$ in the frequency frame is:

$$B_e(t) = \sqrt{{B_1}^2(t) + \left(\frac{\Delta\omega(t)}{\gamma}\right)^2} \qquad [24]$$

Different to conventional pulses where $\boldsymbol{B}_e$ is static, on adiabatic pulses it changes in time.

A second rotating frame where the effective field of the adiabatic pulse is static (as the effective field of a non-adiabatic pulse is static in the first rotating frame or frequency frame) helps to better understand the motion of the magnetization. The second rotating frame changes its orientation with $\boldsymbol{B_e}$(t) relative to the frequency frame at an instantaneous angular velocity of dα(t)/dt, where α(t) is:

$$\alpha(t) = \arctan\left(\frac{\Delta\omega(t)}{\gamma B_1(t)}\right) \qquad [25]$$

Resulting in an additional term to the effective field of the second rotating frame, that will be defined as:

$$B'_e(t) = \sqrt{{B_e}^2(t) + \left(\frac{d\alpha(t)}{\gamma dt}\right)^2} \qquad [26]$$

However, if the magnetic field component attributed to the angular velocity of $\boldsymbol{B_e}$(t) is much smaller of the amplitude of $\boldsymbol{B_e}$(t) i.e.:

$$\left|\left(\frac{d\alpha(t)}{\gamma dt}\right)\right| \ll |B_e(t)| \qquad [27]$$

the adiabatic condition is fulfilled and the additional term dα(t)/ γdt can be neglected ($\boldsymbol{B'}_e(t) \approx \boldsymbol{B}_e(t)$).

2.2.3.2 SLICE SELECTION

The principle of localization with semi-LASER (Öz and Tkáč 2011; Scheenen et al. 2008) and LASER (Garwood and DelaBarre 2001) is similar to localization with PRESS (three orthogonal slices and a spin echo). But the two refocusing pulses are replaced by two pairs of Adiabatic Full Passage pulses (AFP) for semi-LASER, and for LASER the excitation 90° pulse is also substitute by a pair of AFP pulses. The AFP pulses fulfil the adiabatic condition, are amplitude and frequency modulated and generate a uniform nutation angle independent of the RF amplitude. AFP pulses are applied in pairs instead of individually (like normal RF pulses) because a single AFP pulse induce a nonlinear phase shift that can be corrected by applying a second identical one.

The main advantage of the LASER and semi-LASER localization sequences over PRESS and STEAM is that the method is completely adiabatic. Therefore, the excitation is immune to $\boldsymbol{B}_1$ inhomogeneities, the localization can be better defined, the chemical shift displacement artifact is eliminated, and the sharpness of the voxel's edges is improved. One disadvantage is the needed increase of the echo time (TE). Nevertheless, LASER is an excellent method to detect strongly coupled spins systems like glutamate or glutamine.

Chapter 3

Biochemical and Physiological Background

3.1 MRI and MRS for the study of brain function

The proper understanding of brain function has been a challenge of great interest for the scientific community for more than 100 years (Lisman 2015; Di Salle et al. 1999), having today multiple applications that can be grouped into two major areas. On one side, the field of Cognitive Neuroscience, focused on the mental processes involved in awareness, reasoning, acquisition of knowledge and behavior (Faro and Mohamed 2007). On the other side, the Medical Sciences (Faro and Mohamed 2007) with a large variety of clinical applications as brain tumor surgery, epilepsy, Alzheimer's disease, traumatic brain injury or psychiatric disease (Orringer, Vago, and Golby 2012).

The investigation of the functional organization of the brain started in the 19th century (Raichle 1998; Mosso and Simarro Lacabra 1881; Donders 1851; Roy and Sherrington 1890). A potential correlation between regional cerebral blood flow (CBF) and neuronal activity was observed in humans (Mosso and Simarro Lacabra 1881) and in animals (Donders 1851; Roy and Sherrington 1890). But it was not until 1955 when new research in the topic was done. Kety and Sokoloff (Landau et al. 1955) developed an autoradiographic method for measuring

cerebral blood flow and metabolism that was further optimized by Ingvar and Lassen (Lassen et al. 1963). Lately, magnetic resonance imaging (MRI) (Lauterbur 1973) of the human brain, initially used for the study of neuroanatomy and neuropathology, appeared as a new technique to visualize human brain function (Ogawa, Lee, Nayak, et al. 1990; Ogawa and Lee 1990; Ogawa, Lee, Kay, et al. 1990).

The introduction of MRI in the 1980s and functional magnetic resonance imaging (fMRI) in the 1990s, together with magnetic resonance spectroscopy (MRS), found vast application. MR-based techniques proved advantages with respect to electroencephalography (EEG) or magnetoencephalography (MEG), because they could provide structural, functional and metabolic information of a tissue or organ of interest non-invasively, as well as information on how they interrelate (Mekle et al. 2017; Logothetis 2008). MRS allows the identification of biomarkers of normal and pathological brain states (Öz et al. 2014). Additionally, MRS and MRI are sensitive to neuronal activation and therefore can be used as tools for investigating the human brain at work (Mangia et al. 2006; Mangia et al. 2009).

3.2 Positive and negative blood oxygenation level dependent (BOLD) response

Functional magnetic resonance imaging (fMRI) is nowadays the most used technique in the field of human cognitive neuroscience. Brain MR scanners are available at hundreds of research sites and the number of studies using fMRI for the investigation of human brain function is steadily increasing (Stelzer et al. 2014).

Blood oxygenation-level dependent (BOLD) functional magnetic resonance imaging (fMRI) is the most widely used method for studying human brain activity (Logothetis 2002). Even though it has been routinely applied over the last 20 years, the underpinnings of fMRI BOLD signal changes are still poorly

understood (Attwell et al. 2010; Girouard and Iadecola 2006; Logothetis 2010; Sirotin and Das 2009). They reflect regional changes of cerebral blood flow (CBF) cerebral blood volume (CBV) and blood oxygenation. These three vascular responses are an indirect measurement of local increases in neuronal activity (Logothetis and Wandell 2004).

The origin of the BOLD signal has a biophysical and a physiological component. The biophysical component arises from the magnetic properties of the hemoglobin molecule. Deoxygenated hemoglobin (dHb) is paramagnetic and become diamagnetic when bound to oxygen. Deoxyhemoglobin produces magnetic field gradients that accelerate the MR signal decay. An increase of blood oxygenation means an increase in oxygenated hemoglobin and therefore an increase in MR signal. Hence, a local increase of the BOLD signal on a specific brain region is reflecting an increase of the oxygen concentration in that region. The physiological component that leads to an increase of the oxygen concentration is related to the brain energetics during brain activation. At rest, the brain metabolism is principally oxidative. The cerebral metabolic ratio of oxygen (CMR_{O2}) and glucose (CMR_{Glc}) present a constant ratio CMR_{O2}/CMR_{Glc} close to the theoretical maximum of 6 (6 O_2 are needed to oxidize 1 glucose). However, during activation, CBF and CMR_{Glc} increase drastically while CMR_{O2} increases moderately. There is consequently a mismatch between the oxygen that is being supplied by the blood and the oxygen that is being consumed by the brain (Paulson et al. 2010; Dienel and Cruz 2016) and the increase of blood oxygenated hemoglobin concentration is reflected in an increase of the BOLD signal. The reason behind the preference of a less efficient glycolytic metabolism (1 glucose molecule produces 2 adenosine-triphosphate molecules, ATP) over the complete oxidative phosphorylation (1 glucose molecule produces 36 ATP) in a situation of oxygen oversupply, is still not understood. Later studies showed that there is not much difference between glucose and O_2 uptake rates (Madsen et al. 1999) and that 60% (Mangia et al. 2009) or almost the entirety (A.-L. Lin et al. 2010) of the extra

ATP produced upon activation derives from oxidative phosphorylation. In any case, BOLD fMRI signal reflects functional hyperemia.

The percentage of BOLD signal change, ΔBOLD, is a dimensionless quantity that refers to the relative MR signal change normalized to the baseline signal. In the presence of a certain stimulation paradigm, a Positive BOLD Response (PBR) is when the BOLD signal increases over a baseline level (Ogawa, Lee, Kay, et al. 1990), and a Negative BOLD Response (NBR) when it decreases. The NBR has been observed in animal and humans (Huber et al. 2014), in motor (Allison et al. 2000; Hamzei et al. 2002; Newton, Sunderland, and Gowland 2005; Stefanovic, Warnking, and Pike 2004), somatosensory (Hlushchuk and Hari 2006; Kastrup et al. 2008; Klingner et al. 2010; Klingner, Ebenau, et al. 2011; Klingner, Huonker, et al. 2011) and visual cortex (Bressler et al. 2007; Pasley, Inglis, and Freeman 2007; Shmuel et al. 2002; Smith, Williams, and Singh 2004; Tootell et al. 1998; Wade and Rowland 2010), in regions adjacent to the PBR. Although initially hypothesized to just represent a mechanism of blood stealing (Harel et al. 2002; Woolsey et al. 2017) in favor of regions of PBR, later publications show a correlation of the NBR with neuronal activity (Shmuel et al. 2006; Mullinger et al. 2014), characterized by a different neurovascular coupling than PBR (Huber et al. 2014). Similarly to the PBR being used to map activated brain regions in scientific or clinical studies, it is of interest to elucidate whether the NBR can be used to map regions of neuronal inhibition in humans *in vivo* non-invasively.

3.3 The neurovascular coupling

Understanding how changes in neural activity alter hemodynamics is crucial for a meaningful interpretation of fMRI results (Logothetis and Wandell 2004). The neurovascular coupling is the active process that links the local neuronal activity to an increase in local blood flow (Phillips et al. 2015). So far, a range of candidate mechanisms have been proposed but a consensus has not been

reached yet and the topic has been recently reviewed by different authors (Lourenço et al. 2017; J. A. Filosa et al. 2016; Kowiański et al. 2013; Phillips et al. 2015; Hillman 2014; Attwell et al. 2010). The three principal components of the neurovascular unit are the vascular smooth muscle, the neuron and the astrocyte glial cell (**Figure 6**). Both neurons and astrocytes alter vascular tone independently, playing a synergistic or antagonistic role, depending on the physiological environment (Iadecola and Nedergaard 2007; Attwell et al. 2010; Lecrux and Hamel 2011). The proper knowledge of how neurons and astrocytes regulate blood flow is crucial in order to understand neuronal computation, interpret functional imaging and develop treatments for neurological disorders (Attwell et al. 2010).

Initial studies proposed that hyperemia is controlled by a negative feedback loop to fulfil the energy demands of brain activation (Attwell et al. 2010; Tian et al. 1995; Attwell and Laughlin 2001). However, the absolute level of energy usage does not directly regulate CBF, since hypoglycemia and hypoxia have been shown to have no effects on the local CBF responses to physiological brain stimulation (Powers, Hirsch, and Cryer 1996; Mintun et al. 2001). The increase in CBF is up to 4 times greater than the ATP consumption during sustained neuronal activation (A.-L. Lin et al. 2010). A negative-feedback system cannot produce a sustained increase in energy supply that is larger than the increase in energy consumption. Currently, there is enough evidence for a feedforward mechanism signaled by glutamatergic neurotransmission (Offenhauser et al. 2005; Attwell et al. 2010). The vasodilation happening during the functional brain activation, with an increase in CBF and blood oxygen, is indirectly triggered by an increase of extracellular glutamate.

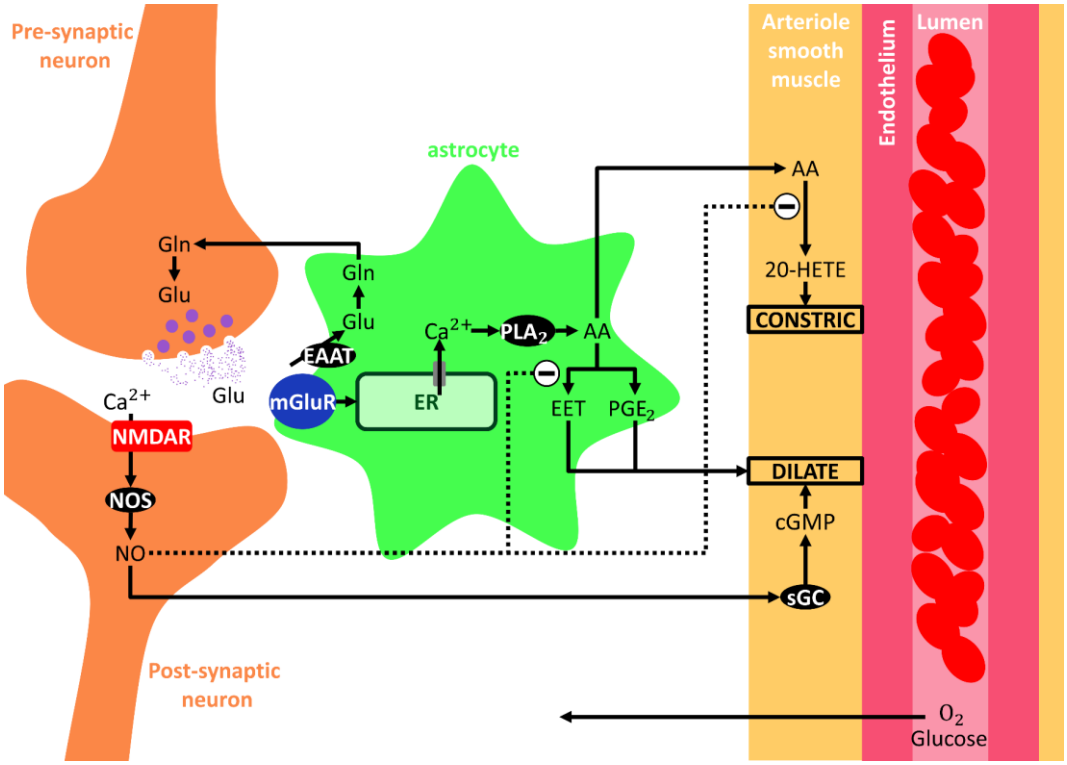

Figure 6: The neurovascular coupling. Schematic representation of some of the mechanisms triggered after glutamatergic neurotransmission. Synaptically released glutamate can bind the ionotropic N-methyl-D-aspartate receptors (NMDAR) on the post synaptic neurons or the mGluR metabotropic receptors on astrocytes. Binding to NMDAR allows the entrance of Ca^{2+}, increasing its intracellular concentration and activating nitric oxide synthase (NOS) that produces nitric oxide (NO). NO activates soluble guanylate cyclase (sGC) on arteriole Smooth muscle cells (SMC) that generates cyclic guanosine monophosphate (cGMP) leading to dilation. On the astrocytes, activated mGluR receptors via intracellular signaling induce the release of Ca^{2+} form endoplasmic Reticulum (ER) into the cytosol. The increased Ca^{2+} cytosolic concentration activates phospholipase A2 (PLA2) that generates arachidonic acid (AA) and its derivates: epoxyeicosatrienoic acid (EET) and prostaglandin E2 (PGE2). EET and PGE2 diffuse into the SMC and cause dilation. AA on SMC is transformed into 20-hydroxyeicosatetraenoic acid (20-HETE) that produces contraction. NO can inhibit the production of EET and 20-HETE (dashed lines). Glutamate is recycled via uptake by excitatory amino acid transporters (EAAT) on astrocytes, where it is metabolized to glutamine, that is transported back to neurons. Adapted from (Phillips et al. 2015; Lourenço et al. 2017; Attwell et al. 2010).

3.3.1 Neuronal glutamatergic signaling

The excitatory neurotransmitter glutamate is the neurotransmitter that possesses the greatest number of receptors, heterogeneously distributed along the central nervous system (Siegel 2006). In the cerebral cortex, 80% of the neurons and synapses are glutamatergic (Shepherd 2004). Neurotransmitter receptors can be

classified into two main groups: **ionotropic** or **metabotropic**. **Ionotropic** receptors activate ligand-gated ion channels, are fast and integrate thousands of inputs temporally and spatially. **Metabotropic** receptors trigger second messenger cascading signaling, and are distinguished by a slow response and a long-term output, as it could be genetic expression (Siegel 2006). Glutamatergic ionotropic receptors are cationic, i.e. produce an excitatory potential (depolarization) of the post synaptic neuron. There are three functional subgroups named after their main artificial agonist: kainate, AMPA (α-amino-3-hydroxy-5-methyl-4-isoxazole propionic acid) and NMDA (N-methyl-D-aspartate). Kainate and AMPA induce Na^+ currents while NMDA induce Ca^{2+} currents.

In the context of the neurovascular coupling, glutamate released from the pre-synaptic neuron can trigger different signaling pathways depending on the kind of post-synaptic receptor. The binding to the neuronal NMDA receptors results in Ca^{2+} entry, that induces the production and release of nitric oxide (NO) via the activation of neuronal nitric oxide synthase (nNOS). Released NO dilates the parenchymal arterioles (**Figure 6**) (Busija et al. 2007). This has been observed *in vivo* in animals (Ma et al. 1996), where inhibition of cortical nNOS reduces the CBF increase associated with activation. The response is then restored by the addition of constant concentration of NO, which indicates that a dynamic rise of NO concentration in response to neuronal activity does not directly mediate neuron-to-vessel signaling (Lindauer et al. 1999). More likely NO modulates the astrocytic signaling pathways for dilate and constrict blood vessels.

3.3.2 Astrocytic glutamatergic signaling

The *nutrition theory* presented by Golgi in 1903 (Golgi 1903), in which astrocytes serve as a mere trophic and structural support unit for neurons, has been consistently confirmed during the last 100 years (Bélanger, Allaman, and Magistretti 2011). However, recent evidence points in the direction that neuroglia

possesses additional functions, as already hypothesized also at the beginning of the 20th century by Cajal (S. R. y Cajal 1895; S. y Cajal 1897). Astrocytes display cellular excitability based on variations in intracellular calcium concentration evoked by synaptic activity and sensory stimuli (Wang et al. 2006; Perea, Navarrete, and Araque 2009; Takata et al. 2011; Navarrete et al. 2012; Alfonso Araque et al. 2014). Astrocytes do not only respond to neurotransmitters but can also release neuroactive substances (gliotransmitters) including glutamate, γ-aminobutyric acid (GABA), ATP/adenosine or D-serine (Volterra and Meldolesi 2005; Alfonso Araque et al. 2014; Perea, Navarrete, and Araque 2009). In fact, astrocytes have been re-discovered as integral elements of the synapses that actively exchange information with the neuronal elements, a physiological concept known as the Tripartite Synapse (Halassa, Fellin, and Haydon 2009; A Araque et al. 1999; Perea, Navarrete, and Araque 2009).

Regarding the neurovascular coupling, astrocytes' endfeet envelop blood vessels and can signal to the smooth muscle cells that control vessel diameter. *In situ* experiments on brain hippocampal slices showed that synaptic released Glutamate joins the mGluRs metabotropic receptors on the astrocytes, inducing an intracellular increase of Ca^{2+} (Porter and McCarthy 1996). Later, brain cortical slices (Jessica A Filosa et al. 2006) suggested that astrocytic Ca^{2+} waves trigger the release of K^+ locally into the perivascular space to activate smooth muscle cells (SMC) Kir channels (Knot, Zimmermann, and Nelson 1996; McCarron and Halpern 1990). Activation of SMC Kir channels results in SMC hyperpolarization (Knot, Zimmermann, and Nelson 1996; Zaritsky et al. 2000), which closes voltage-dependent Ca^{2+} channels in the SMCs and leads to decreased SMCs intracellular Ca^{2+} and vasodilation (Knot, Zimmermann, and Nelson 1996; Knot and Nelson 1998). Nevertheless, it remains to be determined whether this K^+ release mechanism contributes to the regulation of blood flow *in vivo*.

On the other hand, the increase of intracellular Ca^{2+} in astrocytes evoked by the binding of Glutamate to the receptors mGluRs, activates phospholipase A2,

that triggers the production of arachidonic acid from membrane phospholipids. Arachidonic acid can then be metabolized into prostaglandins and epoxyeicosatrienoic acids (EETs) which dilate nearby arterioles (Zonta et al. 2002; Metea and Newman 2006; Gordon et al. 2008; Peng et al. 2002; Peng et al. 2004). The prostaglandin PGE2 can relax vascular smooth muscle by binding to EP4 prostaglandin receptors (Davis et al. 2004). The dilation produced by PGE2 and other arachidonic acid metabolites also partly reflects their activation of K^+ channels in SMCs (Serebryakov et al. 1994; Campbell et al. 1996), making the membrane potential more negative and therefore decreasing the entry of Ca^{2+} through voltage-gated channels. EETs may also elicit dilation by inhibiting receptors for thromboxane (Behm et al. 2009), a vasoconstricting metabolite (also derivative of arachidonic acid). *In vivo*, 70% of astrocytic-dependent vasodilation is mediated by prostaglandins (Takano et al. 2017). Astrocytic Ca^{2+} increases have been observed to also induce vessels constriction *ex vivo* (Metea and Newman 2006; Mulligan and MacVicar 2004) and in pathological conditions *in vivo* (Chuquet, Hollender, and Nimchinsky 2007). Whether an astrocytic intracellular increase of Ca^{2+} induces vasoconstriction or dilation may be controlled by the pre-existing tone of the vessels (Blanco, Stern, and Filosa 2008) and the O_2 concentration.

A third astrocytic pathway of CBF modulation independent of K^+ or Ca^{2+} waves and arachidonic products involving neurotransmitter uptake has been proposed (Petzold et al. 2008; Schummers, Yu, and Sur 2008), but further validation is necessary.

It is still not clear which pathway (neuronal or astrocytic) has a bigger contribution to CBF regulation, since intracellular calcium waves induced by synaptic glutamate occur in both cell types (Lauritzern 2005). Moreover, this is difficult to determine, since the different signaling pathways interact between them. It is possible that the percentage of neural and astrocytic vasoactive contribution differs across different brain regions or different neural pathways of the same region.

3.3.3 Vasoactive modulators

NO and O_2 concentration can regulate whether vasodilation or vasoconstriction is produced. NO regulates the arachidonic acid pathways, and O_2 can influence functional hyperemia in three ways. First, O_2 is needed for the synthesis of NO and arachidonic acid derivatives, so limited O_2 concentration will affect these signaling pathways. Second, at low O_2 concentrations the lack of energy for ATP synthesis will derivate in an increase of extracellular adenosine, inhibiting SMCs constriction. Third, also when O_2 concentration decreases, the glycolysis products will continue in favor of the production of lactate instead of the oxidative phosphorylation, and extracellular released lactate promote vasodilation (Gordon et al. 2008). The role of O_2 as a vasoactive modulator could be one of the reasons for the preference of anaerobic brain metabolism in the presence of sufficient or excess of oxygen during activation.

3.3.4 Other cell types

Pericytes are isolated contractile cells on capillaries that have been suggested as additional regulators of cerebral blood flow (Zehendner, Wedler, and Luhmann 2013; Fernandez-Klett et al. 2010). They can be constricted and dilated by neurotransmitters in vitro (Zehendner, Wedler, and Luhmann 2013; Puro 2007) and a recent study demonstrated that they are the first vascular elements to dilate during neuronal activity, making them the initiators of functional imaging signals (Hall et al. 2014).

GABA interneurons, located between glutamatergic pyramidal cells, also project a variety of vasoactive substances into micro vessels that lead to both constriction and dilation of cerebral microvasculature (Cauli et al. 2004).

3.4 Brain energetics and functional MRS (fMRS)

The cellular basis of energy metabolism during brain activation has being a matter of debate during the last 20 years (L Pellerin and Magistretti 1994). The problem, originated by spatial-temporal technical limitations, is centered on understanding astrocyte-neurons interactions and the interpretation of cellular contributions to brain imaging. In 1994 Pellerin and Magistretti (L Pellerin and Magistretti 1994) proposed the astrocyte-to-neuron lactate shuttle hypothesis. This model claims that the energy needed to take the synaptic released glutamate by the astrocytic glutamate transporters (1 ATP) and to recycle it to glutamine (1 ATP) is fulfilled by the astrocytic glycolysis. The product lactate is then transported to the neuron where it is completely oxidized by conversion to pyruvate and entry into the tricarboxylic acids cycle (TCA). Therefore, the energy demands of glutamatergic neurotransmission (higher than resting state) are satisfied. Glucose consumption was proposed as the main mechanism to fuel of neurons at rest, that cannot be increased during activation (Magistretti and Allaman 2015), when lactate is the major and necessary fuel. Although its authors have reviewed the evidences supporting this model in several occasions afterwards (Bélanger, Allaman, and Magistretti 2011; Luc Pellerin and Magistretti 2012; Magistretti and Allaman 2015) it has also received numerous criticisms (Hertz, Gibbs, and Dienel 2014; Dienel 2012; DiNuzzo et al. 2010; Mangia et al. 2009; Dienel and Cruz 2004). A recent publication even argues that the model is stoichiometrically incorrect and not possible (Dienel 2017). In addition, most of the current hypothesis about brain metabolic fluxes have been obtained from *in vitro* studies of cultured cells or mathematical formulation. Consequently, further *in vivo* studies need to be done for understanding physiological and metabolic basis of brain energetics.

MRS methodologies are sensitive to different aspects of neuronal activation and provide complementary tools for investigating the human brain at work. In

recent years, several functional magnetic resonance spectroscopy (fMRS) studies have been performed to characterize the relationship between neuronal activation and energy or neurotransmitter metabolism. Those studies attempt to get a non-invasively direct measurement of brain energetics and neurotransmission by tracking the dynamic concentration changes of the different metabolites from the ^{1}H MRS spectrum. Initial studies (Maddock et al. 2006; Prichard et al. 1991; Sappey-Marinier et al. 1992) showed changes in the lactate concentration at low fields (1.5-2T) in the visual cortex. Dynamic changes of metabolite concentrations in the human brain were successfully detected at 7 T in response to visual, motor, or auditory stimulation. Mangia et al. (Mangia, Tkác, et al. 2007) investigated the metabolic changes on visual cortex during prolonged periods of visual stimulation. Increases in lactate (Lac) and glutamate (Glu) by 23% and 3% and decreases by 15% on aspartate (Asp) were found, respectively. A few years later, Lin et al. (Y. Lin et al. 2012) demonstrated significant increases (2% to 11%) in Lac, Glu and glutathione (GSH) and decreases in Asp, glutamine (Gln) and glycine (Gly) in visual cortex. Later on, Schaller et al. (Schaller et al. 2014) observed similar dynamic changes of Glu and Lac during the stimulation of the motor cortex and Bednarik et al. (Bednařík et al. 2015) showed that BOLD-fMRI signal changes were positively correlated with the concentration changes of these two metabolites. However, BOLD signals did not correlate with Glu dynamics at 3 T with an event-related suppression paradigm (Apšvalka et al. 2015) and another recent 7 T study found a 5% decrease in GABA and 7% increase on Lac as the only significant changes during visual stimulation (Mekle et al. 2017). Finally, a novel sequence, capable of acquiring simultaneously fMRS and fMRI BOLD, was presented, which showed that the Glu dynamics of concentration changes correlated with the BOLD percental of signal change (Ip et al. 2017).

Chapter 4

Methods

4.1 Purpose

For detecting very subtle metabolic changes as in fMRS experiments it is of interest moving to higher magnetic fields, where the increased SNR and resolution help for a better quantification. However, higher magnetic fields introduce a set of challenges that needs to be addressed in order to make the expected theoretical gain in sensitivity effective.

On the first place $\boldsymbol{B}_0$ and $\boldsymbol{B}_1$ inhomogeneities increase. That implies the necessity of a careful pre-scanning optimization of shimming and B_1 amplifier calibration (**Figure 7**) for a better SNR, water suppression and slice definition. Secondly, the CSDA also increases. At 3 T and lower fields, PRESS seems to be a better choice over STEAM thanks to the two-fold increase in SNR. However, at 7 T and higher fields, due to the 90° refocusing pulses STEAM allows a better slice definition and reduces the CSDA. On the other hand, the 180° adiabatic pulses of LASER and semi-LASER address this issue without any SNR penalty.

This chapter discusses the methodology to be adopted before, during and after MRS acquisitions to obtain good quality spectra **(Figure 8).** Among the different aspects that define the quality of an NMR spectrum, we could highlight a good SNR, good resolution of the chemical shifts of the different metabolites, narrow, well-defined linewidths of the resonance peaks, good suppression of

unwanted (spurious) signals, and a flat baseline. A complete gallery or artifacts and parameters for quality assessment can be found in the literature (Roland Kreis 2004; De Graaf 2007). Below, the most important aspects which we have focused on are presented.

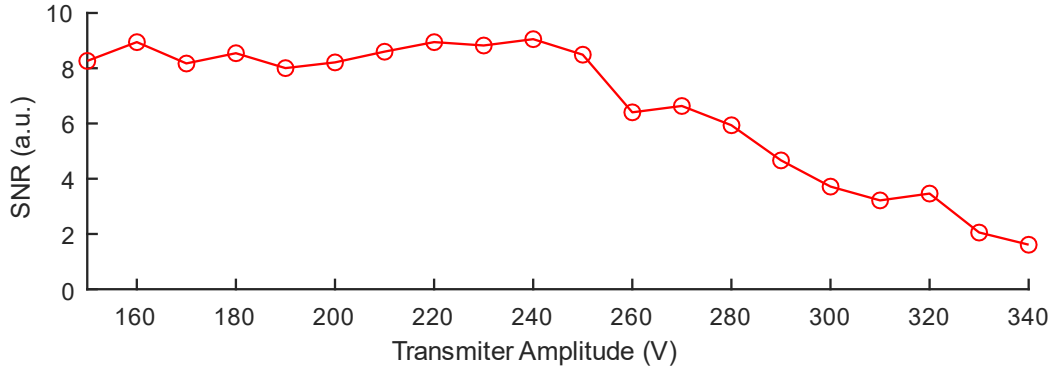

Figure 7: SNR varying with B_1. The optimum SNR is achieved after carefully adjusting the transmitter amplitude. The values refer to a spherical water phantom. STEAM acquisition, TR/TE = 2000/11ms, 8 ml voxel on isocenter, 16 averages, MAGNETOM 7 T scanner (Siemens Healthcare, Erlangen, Germany).

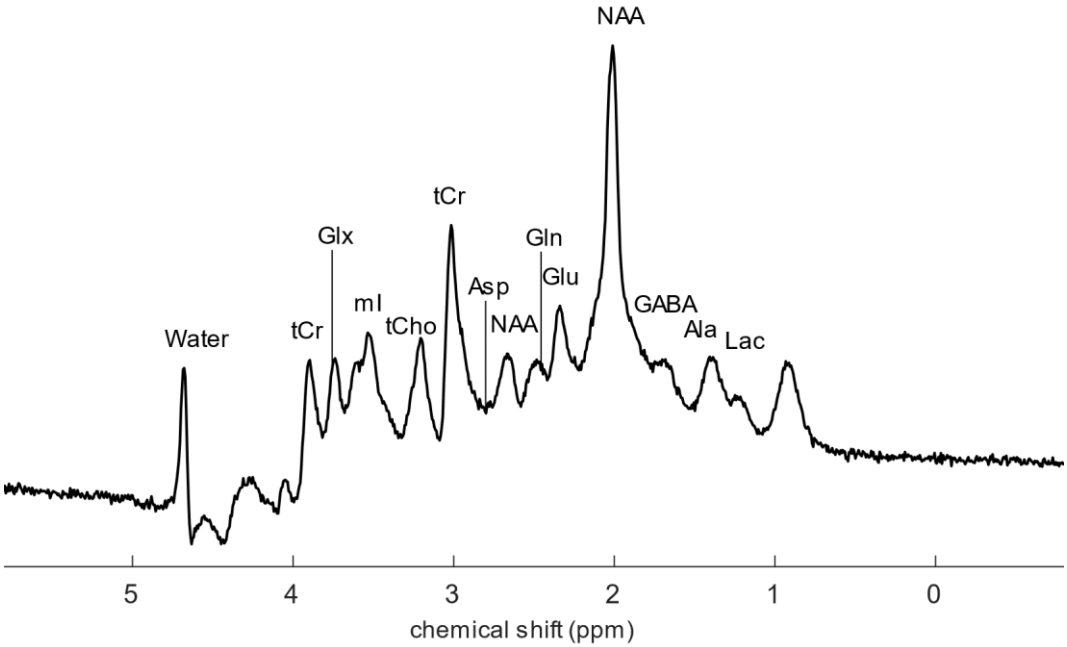

Figure 8: STEAM spectrum from a human visual cortex (female, 27 years old). 7 T, TR/ TE = 4500/4.62ms. The resonance peaks of a set of metabolites can be appreciated. The water peak is efficiently suppressed.

4.2 Full width at half maximum (FWHM)

The linewidth of a resonance peak is most commonly expressed in terms of full width at half maximum (FWHM). For metabolic quantification, the fit error scales with the linewidth. Therefore, a broader peak increases the fit uncertainty. A homogeneous $\boldsymbol{B_0}$ field provokes a slow T2* decay and therefore a narrow linewidth of the resonance peaks. And the opposite applies for an inhomogeneous $\boldsymbol{B_0}$. The way of improving $\boldsymbol{B_0}$ homogeneity prior to acquisition is by shimming the sample. The process of shimming is explained in detail later in this chapter.

Other factor that can influence the linewidth of a spectrum after averaging all acquisitions is the $\boldsymbol{B_0}$ frequency drift. During an MRS acquisition, the $\boldsymbol{B_0}$ frequency undergoes a progressive drift. This drift can become relevant if the acquisition is long. The drift causes a progressive frequency shift of the peaks of interest for successive repetitions. In turn, if the drift is not corrected, the linewidth of the final averaged spectrum is broadened (**Figure 19**). This frequency drift can be corrected either prospectively or retrospectively. Later in this chapter a method for retrospective frequency drift correction is explained.

4.3 Spurious signals

Applying a shim gradient when a sample is placed inside the magnet, a shift in resonance frequencies in regions outside the MRS voxel can be produced, which may be more pronounced in regions more distant from the selected volume of interest (VOI). Hence, the local water resonance may shift outside the suppression band in such regions. A similar effect may be produced by anatomy-related susceptibility variations in the object (e.g. a human head) (R. Kreis 1997; Collins et al. 2002; Li et al. 1996). Such shifts in the local Larmor frequency will be different for the different slices excited in single-voxel localization schemes.

Therefore, spurious signals due to unsuppressed water can appear at apparently random chemical shifts in the spectrum.

$\boldsymbol{B_0}$ inhomogeneities and local susceptibility effects provoke cancellation of gradient crusher pulses. Thus, crushers must be adjusted in strength, duration, and/or distribution in order to avoid refocusing of unwanted coherences (Starck et al. 2009).

Some solutions to avoid spurious signals are to apply:

- More and/or stronger crusher gradients.
- **Phase cycling**. RF phase cycling can eliminate unwanted echoes. The effect may be degraded by experimental instabilities, phase inaccuracies, or motion.
- **Wider frequency selectivity.** Increasing the bandwidth of the water suppression pulse may avoid the refocusing of the water signal from regions with increased frequency offset. However, this might also produce unwanted suppression of metabolite resonances in the vicinity of the water line.
- **Less second-order shimming.** By higher-order shims, improved homogeneity inside the VOI may be obtained at the cost of increased associated frequency offsets in regions distant to the VOI. Nevertheless, for insufficient shimming, spectral resolution and SNR might be too low for reliable quantification.
- **Filtering.** Applying filters during post-processing helps to mitigate artifacts at the price of correspondingly increased linewidth.
- **Different orientations.** Positioning the slices defining the VOI should be done in a way that avoids anatomy-related susceptibility variations.

4.4 Influence of B_1 inhomogeneity on WET water suppression at high fields

At high field, the standard water suppression scheme employing 3 RF pulses (WET) is challenged by the broad $\boldsymbol{B}_1$ inhomogeneity. In this study, we simulated the residual water based on measured T1 distributions of the whole brain obtained with MP2RAGE (Marques et al. 2010) and values of $\boldsymbol{B}_1$ homogeneity at 3 T and 7 T from the literature. Our results suggested that 5 RF pulses are required at 7 T for sufficient water suppression.

4.4.1 Introduction

Water is the most abundant compound in mammalian tissue (10000 times more concentrated than metabolites). The peak at ca. 4.7 ppm originated from its two protons dominates the H^1 MRS spectrum of almost all tissue. The presence of a large water resonance leads to baseline distortions that may make the detection and/or quantification of metabolites unreliable. Efficient suppression of the water signal eliminates baseline distortions and spurious signals, leading to a more reliable and consistent detection of metabolite spectra (De Graaf 2007).

The water signal is typically suppressed by series of chemical-shift-selective RF pulses each followed by a dephasing gradient (CHESS) (Frahm et al. 1989). At low fields (3 T and below), this approach was improved by optimizing the flip angles of three to four RF pulses to reduce effects of T1 and $\boldsymbol{B}_1$ inhomogeneities (WET) (Ogg, Kingsley, and Taylor 1994).

For a proper water suppression during the preparation time using a frequency-selective excitation + gradient dephasing method (Haase et al. 1985; Moonen and Van Zijl 1990; Frahm et al. 1990; Ogg, Kingsley, and Taylor 1994; Tkáč et al. 1999), it is needed the nulling of the longitudinal water magnetization (affected by T1 relaxation, RF-pulse flip angles -which depend on $\boldsymbol{B}_1$ -, and

sequence timing) followed by the complete dephasing of the transverse water magnetization. A single water-suppression sequence is made of a frequency-selective RF excitation pulse followed by a delay period containing a gradient dephasing pulse. This sequence can be repeated to improve the water suppression.

Repeating this sequence with the appropriate choice of flip angles each repetition, can make water suppression independent of $\boldsymbol{B}_1$ and T1.

At high fields, reliable water suppression has been achieved by increasing the number of RF pulses up to seven, and by varying interpulse delays (VAPOR) (Tkáč et al. 1999). These methods have been optimized using monotonic ranges of T1 values and $\boldsymbol{B}_1$ variations.

4.4.2 Purpose

In this study, we measured the distribution of T1 in the whole brain at 3 T and 7 T with MP2RAGE and used standard deviations values of $\boldsymbol{B}_1$ homogeneity obtained from the literature to optimize the WET method. Up to five RF pulses separated by a typical interpulse delay, τ, of 60 ms were applied.

4.4.3 Methods

Whole brain T1 distribution: whole brain MP2RAGE scans were obtained from 3 healthy volunteers (age range; 23 – 31 years, male) with a MAGNETOM Verio 3 T (Siemens Healthcare, Erlangen, Germany). Sequence-specific parameters were: TE/TR = 2.98/5000 ms, TI 700/2500 ms, FA = 4°/5°. The same volunteers were scanned on a MAGNETOM Investigational 7 T (Siemens Healthcare, Erlangen, Germany) with the same sequence and following parameters: TE/TR = 3.33/5000 ms, TI 800/2700 ms, FA = 4°/5°). T1 distribution (histograms calculated from T1 maps) were computed for logarithmically spaced T1 bins between 350 and 3800 ms, then normalized (**Figure 9**).

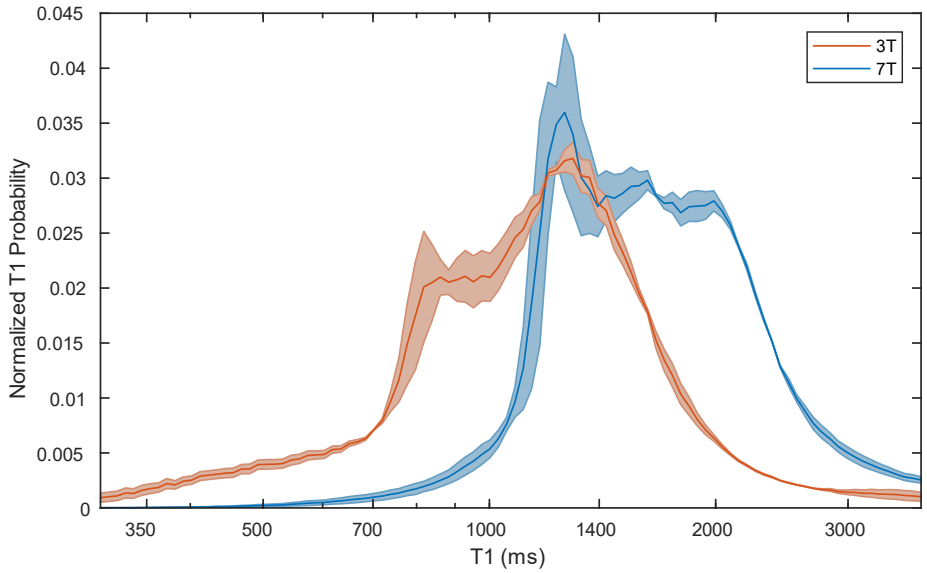

Figure 9: Whole brain normalized distributions of T1 measured with MP2RAGE at 3 T and 7 T (average of 3 volunteers) exhibit a significant shift of the longitudinal relaxation at higher field.

$\boldsymbol{B_1}$ **distribution**: $\boldsymbol{B_1}$ homogeneity was simulated as a scaling factor, b, applied on RF pulse flip angles. It was modelled with a Gaussian distribution centered at 1.0 and with standard deviations of 0.11 and 0.25 for a field strength of 3 T and 7 T, respectively (Pohmann, Speck, and Scheffler 2016).

Simulation: Following a single RF pulse with nominal flip angle θ, the longitudinal magnetization is:

$$M_z(t) = M_z(0)\exp\left(\frac{-\tau}{T1}\right)\cos(b\,\theta) + M_0\left(1 - \exp\left(\frac{-\tau}{T1}\right)\right) \qquad [28]$$

where b is the scaling factor of RF pulse flip angles and M_0 is the equilibrium magnetization. The initial magnetization was adjusted assuming a TR of 3000 ms (Ogg et al. 1994). The residual magnetization, *Mr*, was computed by recursively applying equation [28], scaled by the unsuppressed longitudinal magnetization (**Figure 10**).

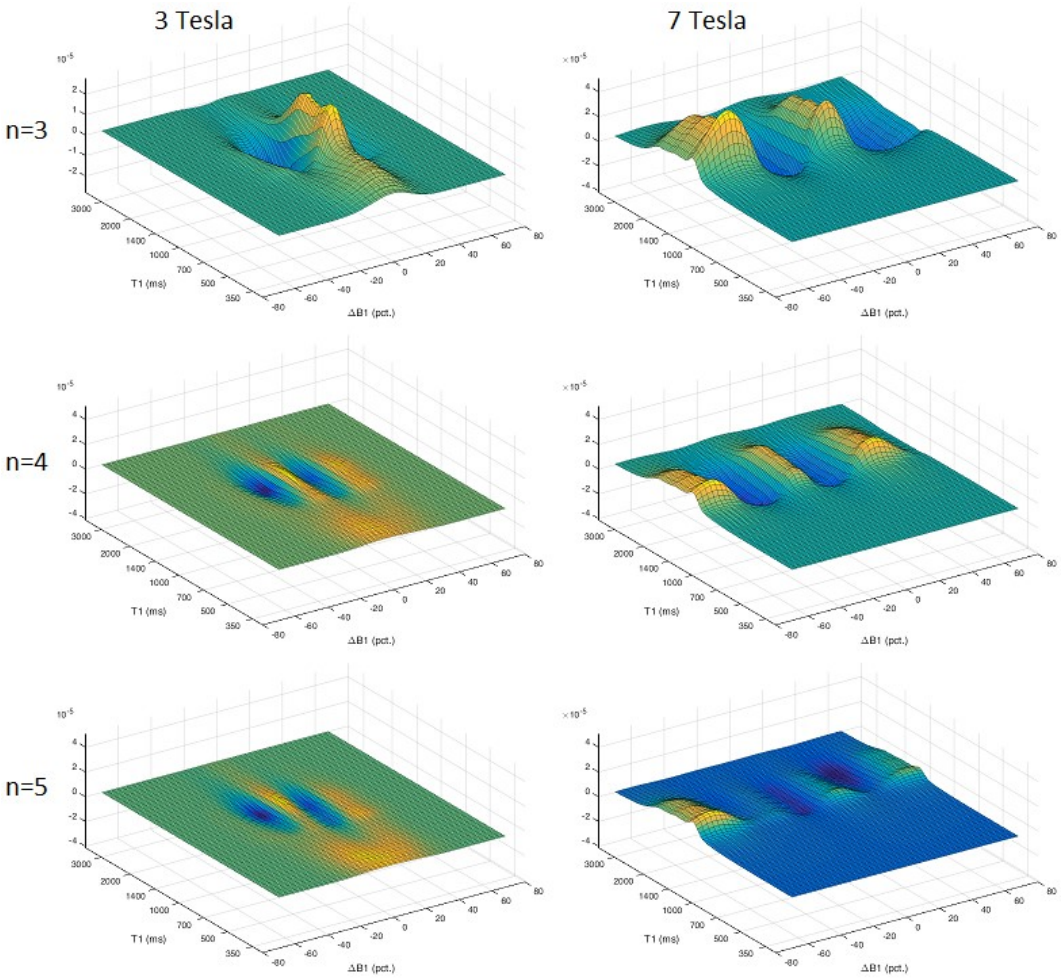

Figure 10: Residual of water simulated at 3 and 7 T with optimized flip angles for 3, 4 and 5 water suppression pulses (**Table 2**) as function of T1 distributions (**Figure 9**) and Gaussian distribution of $\boldsymbol{B}_1$ homogeneity (variation of nominal B_1, ΔB_1, expressed in percentage).

Flip-angle optimization: Upon increasing the number of RF pulses, n, several combinations of flip angles may achieve comparable water suppressions. The effects of flip angle combination on the water suppression was compared by repeating a non-linear least square optimization with a grid of starting parameter values for the RF pulse flip angles (lsqnonlin, MATLAB). The optimized flip angles are reported along with the residual magnetization (**Table 2**).

n	3 T	*Mr*	7 T	*Mr*
3	84.86° ± 0.71 80.87° ± 0.70 135.00° ± 0.28	0.01124 (*0.01559*)	91.41° ± 0.21 71.99° ± 0.15 142.25° ± 0.38	0.04024 (*0.04604*)
4	101.71° ± 0.14 80.90° ± 0.08 74.97° ± 0.08 154.14° ± 0.19	0.00270 (*0.00382*)	117.69° ± 0.25 82.18° ± 0.15 68.13° ± 0.18 175.96° ± 0.47	0.01600 (*0.01772*)
5	74.59° ± 3.30 73.06° ± 3.03 105.24° ± 0.16 70.14° ± 0.30 160.42° ± 0.18	0.00163	90.28° ± 9.21 85.35° ± 9.65 119.32° ± 0.75 79.50° ± 1.48 175.04° ± 0.25	0.00845

Table 2: Flip angles of n water suppression RF pulses separated by an interpulse delay of 60 ms, optimized for TR of 3000 ms using a whole brain distribution of T1 (**Figure 9**) and assuming a B_1 inhomogeneity following a Gaussian distribution with standard deviation of 0.11 and 0.25, respectively at 3 T and 7 T. Mr designates the residuals scaled by the unsuppressed signal. For comparison Mr values for 3 (89.2°, 83.4°, 160.8°) and 4 pulses (81.4°, 101.4°, 69.3°, 161.0°) published by Ogg et al. (Ogg, Kingsley, and Taylor 1994) are given in parenthesis.

4.4.4 Discussion

Although a slight improvement of the residual water magnetization (*Mr*) is achieved by optimizing the flip angles (compared to values reported by Ogg et al. assuming T1 of 800 ms), our results highlight the deteriorating effect of a wide distribution of B_1 at high field. This translate at 7 T in the formation of residual magnetization at the edge of the B_1 distribution which requires additional RF pulses compared to the standard WET at 3 T. Our numerical simulations suggest that at least 5 RF pulses are needed to implement the WET water suppression scheme at 7 T.

4.5 Shimming

4.5.1 Purpose

Magnetic field inhomogeneities, arising from susceptibility differences, chemical shifts, or fabrication imperfections of the magnet, are a major problem in MRI and MRS. Susceptibility artifacts become particularly serious in case of brain imaging of specific areas where interfaces between air and tissue are located (for instance, in the prefrontal cortex, PFC) and when ultra-high fields (≥ 7 T) are involved (Seifert et al. 2007). For these reasons a renewed focus on the "art" of shimming is proposed in this work, based on and motivated by the fact that shimming techniques are sometimes unjustifiably taken for granted in MRI routines. In particular, the question to be addressed is: what is the best shimming strategy for high fields MRS applications? The idea is to compare different shimming techniques, proceeding on a route through history. Image-based shimming is perfect for MRI, but is the resulting peak lineshape sufficient for MRS? Should lineshape-based shimming be (re)considered?

4.5.2 Historical review

The very first active shimming was described in 1958 by Golay in a paper called "Field Homogenizing Coils for Nuclear Spin Resonance Instrumentation" (Golay 1958). Based on the fact that, in the bore of the magnet, the magnetic field can be described by an expansion in spherical harmonics, he designed a set of coils (each pair associated with a specific spherical harmonic) to correct field inhomogeneity. A few years later, in 1968, considering that the spectral line shape reflects the homogeneity of the field, Ernst developed a semi-automatic iterative method for shimming, based on a simplex method (R. R. Ernst 1968). Nevertheless, manual techniques did not lose popularity, at least not until the nineties, when a couple of papers about shimming by interactive adjustment of spectral lineshape

appeared (Chmurny and Hoult 1990). Van Zijl et al. in 1994 developed a technique based on the 3D mapping of magnetic field variations (Maudsley, Simon, and Hilal 1984) that could adjust automatically the shim coils at different orders (Moonen and Van Zijl 1990). Meanwhile, FASTMAP routines were proposed (Gruetter 1993), which could adjust both first- and second-order shim coils in 2 minutes. In the years to come, a great emphasis was given to automated shimming and several different strategies were proposed; in particular, dynamic shimming based on a field mapping scan seems promising (Sengupta et al. 2011). Automated shimming substantially replaced the previous techniques, so that the new experimenters do not acquire familiarity with interactive and simplex-based methods. However, while this might have little impact when imaging at fields up to 3 T, we may wonder if it is still the most satisfactory option in terms of time efficiency and resolution when ultra-high fields are employed. A paper by Weiger et al. (Weiger, Speck, and Fey 2006) points out the relevance of the spectral lineshape for an improved shimming quality.

4.5.3 Shimming strategies in vivo

Shimming strategies *in vivo* can be divided in: 1) fieldmap-based shimming, 2) projection-based shimming i.e. FASTMAP/FASTESTMAP (Gruetter 1993; Gruetter and Tkáč 2000), 3) dynamic shim updating and 4) interactive shimming. Regarding the interactive shimming there is not a universal procedure and it is advisable to start with a fieldmap-based shimming, follow a systematic approach, and allocate a pre-defined shimming duration.

A proposed interactive shimming procedure consist on the following:

1) **Pre-shim by fieldmap**. A fieldmap is computed by phase measurement and an algorithm compensates field inhomogeneities by linear combination of all shims; appropriate control functions.

2) **Interactive first-order shimming** judged by lineshape (X, Y, Z). Improve linewidth by changing (in both directions) X, Y, Z shims, followed by more refined changes on the more reactive X, Y, Z shims.
3) **Interactive second-order shimming** (Z2, ZX, ZY, X2-Y2, XY). During step **1)** determine the second-order shim(s) that are most varying and start reducing them. Then re-adjust the first-order shims. Next increase selected second-order shim in opposite direction re-adjust the first-order shims again. Keep the best shims after trying to adjust the selected second order shims in both directions and repeat with the following second-order shims. **Table 3** compiles a list of interactions and Cartesian functions to consider for second-order shimming.

order	Shim	equation for Field Generated	update in combination with
0	1	1	
1	X	x	
1	Y	y	
1	Z	z	
2	Z2	$2z^2$- $(x^2 + y^2)$	X, Y, Z
2	ZX	zx	X, Z
2	ZY	zy	Y, Z
2	X2-Y2	$x^2 - y^2$	X, Y
2	XY	xy	X, Y

Table 3: Interactions and Cartesian functions for second-order shimming. Adapted from De Graaf R.A., "In vivo NMR Spectroscopy – Principles and Techniques", Second Edition, Wiley (2007), chapter 10.(De Graaf 2007).

4.5.4 Results

To answer the questions of which shimming strategy to choose at 3 T and which at 7 T and if we should consider using interactive shim *in vivo*, different strategies were tested: FASTESTMAP (Siemens WIP479), FIELDMAP (Siemens gradient echo shim WIP452B) and interactive shimming (compare FWHM of water

peak and PRESS spectra, TE/TR = 30/1500 ms, n_{rep}= 128). The voxel locations to test were *In vivo* human brain on different regions (striatum, white matter, visual cortex), at different field strengths.

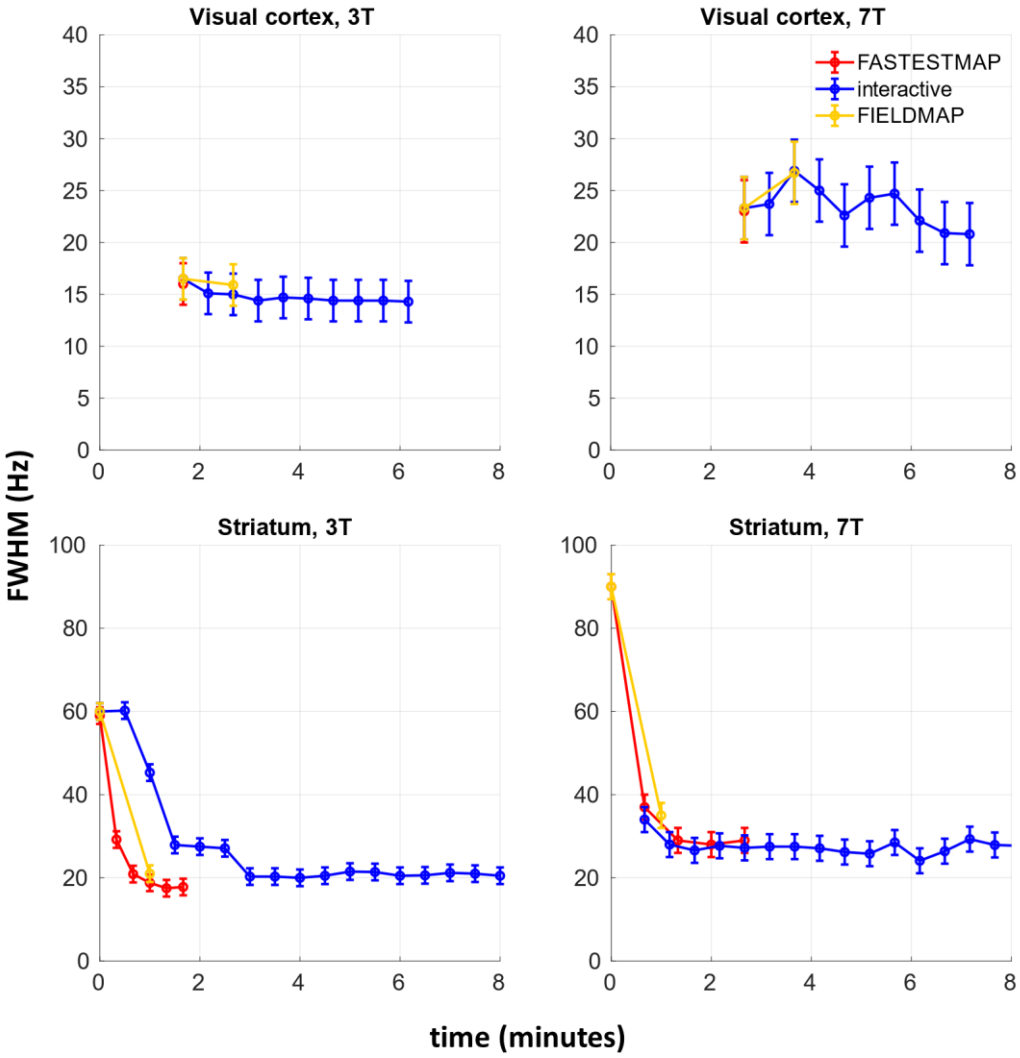

Figure 11: Efficiency of different shimming strategies. FASTESTMAP: red. FIELDMAP: yellow. Interactive: blue.

On **striatum**, FASTESTMAP achieves the best values for FWHM and in a shorter time (about 1 min) at 3 T, while at 7 T FASTESTMAP and interactive shimming are comparable; in both cases, the narrowest FWHM is achieved in less

than 2 min. On **visual cortex,** FIELDMAP and first-order interactive shimming made no obvious improvements in comparison with the shim obtained with FASTESTMAP (**Figure 11**).

4.5.5 Discussion

At 3 T, FASTESTMAP achieves the best SNR and linewidth in ca. 2 min. The interactive second-order shimming reaches similar spectral quality in 10 to 15 min (in terms of LCModel's (Provencher 1993) percentage of Cramér-Rao lower bound (CRLB) of metabolite concentration). At 7 T, FASTESTMAP and interactive shimming reach comparable linewidth in ca. 2 min. The second-order interactive shimming greatly improves SNR, linewidth, and percentage of CRLB of metabolite concentrations, but requires 10 to 15 min.

4.5.6 Conclusions

FASTMAP/FASTESTMAP can provide reliable and excellent results at 3 T while at 7 T, second-order interactive shimming appears to further improve spectrum quality. Consequently, interactive shimming could be considered in single-voxel spectroscopy applications. The first-order shimming is relatively fast and straightforward, and the second-order shimming achieves better results, but is time-consuming. On the other hand, the shim quality and reliability strongly depend on the operator's skills. Therefore, shimming by lineshape would benefit from automated assistants, as recently proposed in high-resolution NMR (Schlenke et al. 2013).

4.6 Optimization of single-voxel MRS sequence acquisition parameters at 7T

4.6.1 Methods

The optimum single-voxel MRS acquisition sequence and parameters at 7 T were investigated with the goals of 1) having the shortest TR possible, in order to increase the temporal resolution of the fMRS experiments, 2) having the shortest TE possible, to increase the number of detectable metabolites, 3) having good spectral quality (based on parameters explained before), 4) having a well-define voxel to increase the spatial resolution and avoid contamination of external signals and partial volume effects, 5) reducing as much as possible the CSDA also to improve spatial resolution.

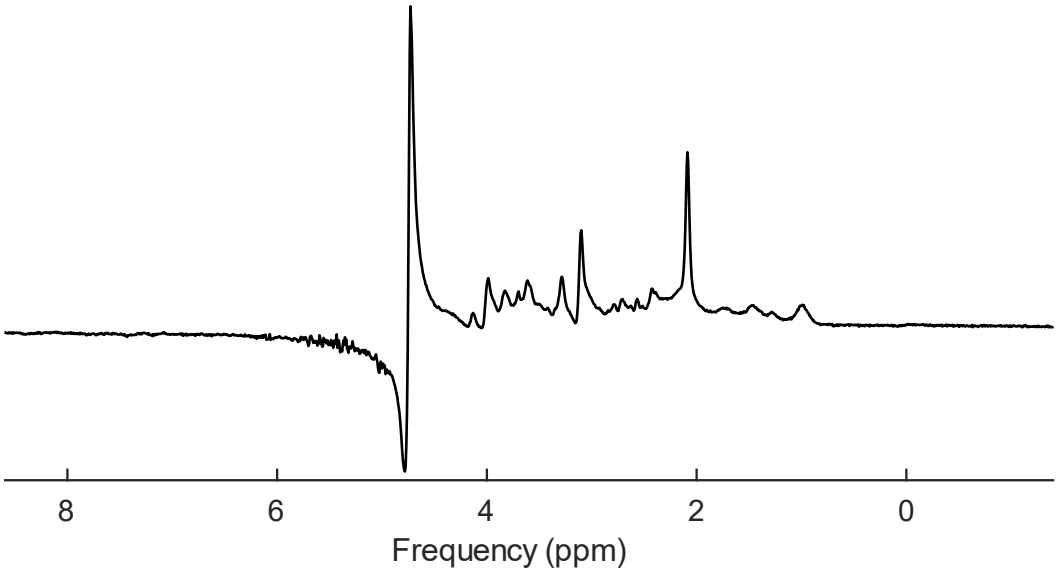

Figure 12: semi-LASER acquisition on human visual cortex (8 ml voxel, 64 averages, TE/TR = 34.68/4160ms, female, 26 years old).

LASER, semi-LASER, STEAM and PRESS sequences were tested on 6 volunteers (visual cortex, 8 ml voxel, 64 averages). The TR was always adjusted to the minimum required within allowed SAR limits. The SNR was measured from the NAA peak (baseline corrected magnitude divided by the standard deviation of the noise from -2 to 0 ppm) and the efficiency of the water suppression calculated as the ratio between the amplitude of the water peak and the NAA peak (the smaller the ratio, the better the water suppression).

4.6.2 Results

Independently of any acquisition parameter the maximum SNR (363.16) was found for semi-LASER (Öz and Tkáč 2011; Scheenen et al. 2008). The lowest mean SNR was found for STEAM. However, it also showed the highest water suppression efficiency **(Figure 8, Figure 14)**.

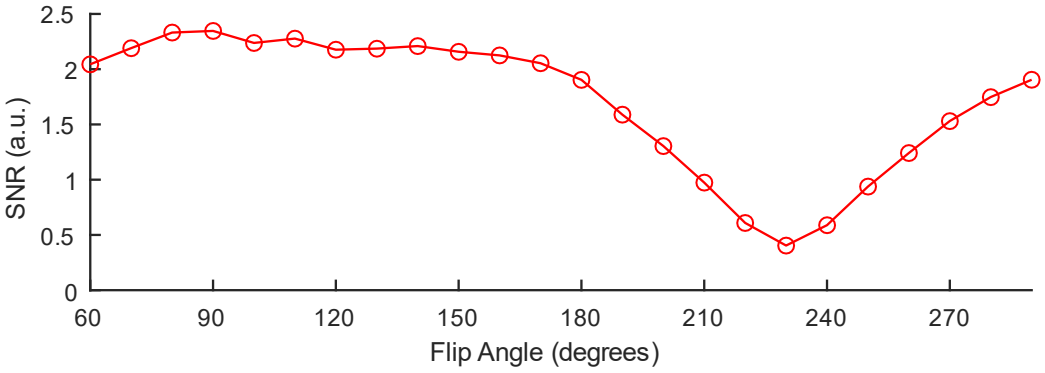

Figure 13: SNR as a function of flip angle (FA) with semi-LASER.

The amplitude of the excitation flip angle for semi-LASER was generally adjusted to show the expected maximum SNR with 90° **(Figure 13)** but the water suppression flip angle could be improved adjusting it to 130° for semi-LASER and 140° for STEAM **(Figure 15).**

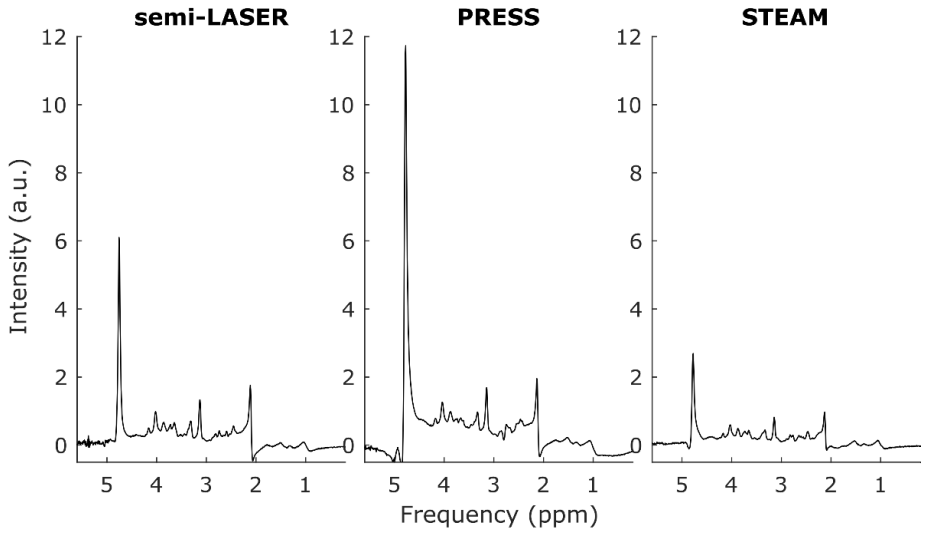

Figure 14: Comparison between semi-LASER, PRESS and STEAM (human visual cortex, 8 ml voxel, 64 averages, female, 26 years old). semi-LASER shows a slightly higher SNR than PRESS, approximately double than STEAM. However, STEAM achieves the best water suppression, while the worst is with PRESS.

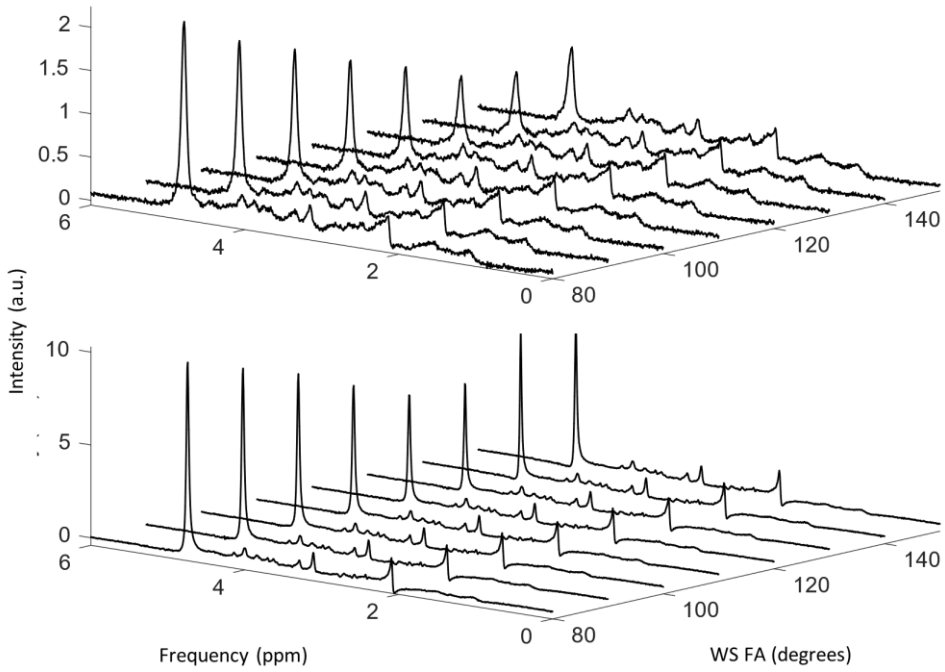

Figure 15: Efficiency of Water suppression dependent on the flip angle (FA). The optimum water suppression is achieved with 140° for STEAM (TOP) and 130° for semi-LASER (BOTTOM).

4.6.3 Discussion

It was shown that the mean SNR that can be obtain with LASER, semi-LASER and PRESS is very similar, although slightly higher for semi-LASER. LASER and semi-LASER present the advantage over PRESS of performing a better slice profile avoiding contamination form signals outside the volume of interest (VOI). However, semi-LASER allows a much shorter TE than LASER because the 90° excitation RF pulse of semi-LASER is a normal sinc pulse while LASER presents two adiabatic pulses.

Considering these previous aspects, the best performance would be given by semi-LASER and STEAM. The advantages of STEAM are the improved water suppression and the possibility of a much shorter TE (up to 6 ms approx.) while it is difficult to obtain a TE shorter than 30 ms for semi-LASER. It is in any case not a major difference since, as explained in the second chapter of this dissertation the j evolution of strongly coupled metabolites like glutamate and glutamine obtained with adiabatic refocusing pulses is similar to normal RF refocusing pulses with shorter TE. Nevertheless, shortening the TE may require an increase of the TR (shorter RF pulses to achieve shorter TE increase SAR and TR need to be increased), and our goal for fMRS experiments is to have the shortest TR possible, to increase temporal resolution. Additionally, a better SNR is obtained with semi-LASER. Making a balance of the pros and cons of each sequence we concluded that the sequence that better fitted our current requirements was semi-LASER.

4.7 Basis set preparation

4.7.1 Purpose

A basis set is a set of model spectra used to fit and quantify the acquired spectra. When using software packages as LCModel (Provencher 1993) for metabolic quantification it is important for model spectra to be as close as possible to the measured data. The basis sets can be either simulated or acquired. A good simulation should consider the shape of the adiabatic RF pulses (Pradhan et al. 2015) or, alternatively, look for the apparent TE from non-adiabatic pulses that would lead to a similar evolution of the metabolites peaks (Giapitzakis et al. 2018; Öz and Tkáč 2011).

		TE (ms) PRESS basis sets							
Volunteer	**TE (ms) LASER acquired**	**0**	**1**	**5**	**10**	**15**	**20**	**25**	**30**
1	**33,4**	31	28	30	34	43	49	39	26
2	**34,7**	29	26	28	31	41	52	45	29
	36	26	24	26	28	35	47	44	31
3	**36,3**	28	27	28	31	39	45	42	29
4	**37,1**	25	27	28	31	39	56	**60**	42
5	**38,7**	23	23	24	27	32	44	48	34
	40	23	21	23	25	31	41	46	35
6	**43**	21	20	21	23	27	35	44	39

Table 4: LCModel 'SNR' on visual cortex as an indication of the goodness of the fit (higher 'SNR' means less residual).

A good approximation for a basis set is to use short TE PRESS spectra. The J evolution of strongly coupled metabolites is very similar with short TE non-adiabatic RF pulses and with longer TE adiabatic pulses (Öz and Tkáč 2011; De Graaf 2007). To find out which TE from PRESS model spectra better fits semi-LASER acquired spectra, we compared simulated PRESS basis sets for different TEs (TE = 0, 1, 5, 10, 15, 20 and 25 ms) to different semi-LASER acquisitions on

different volunteers and TEs. For some specific cases on this dissertation we refer to the SNR output that is given by LCModel. The LCModel SNR is defined as the ratio of the maximum in the spectrum (after baseline substraction) over the analysis window divided by twice the rms residuals. This is a rough estimate that depends on offsets in the model spectra and baseline but gives a general idea of the overall quality of the spectrum being analyzed and the goodness of the fit to the basis set. **Table 4** shows the "SNR" output given by LCModel as an indication of the goodness of the fit (i.e. better fit means less residual and higher SNR) that was obtained for each TE of semi-LASER analyzed with different TE PRESS basis. All spectra were acquired in the visual cortex with 64 averages. It can be observed that the fit is good but not optimal (there is still some residuals) and it can still be improved with an acquired or simulated semi-LASER basis set as can be seen on **Figure 16**. Therefore, we decided to acquire our own basis set.

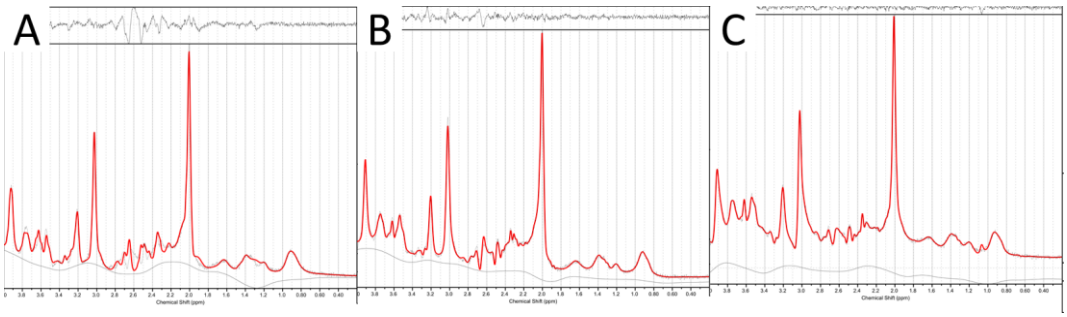

Figure 16: LCModel fit of a semi-LASER acquisition with different basis sets. **A**: LCModel 'SNR' of the fit is 23 using a simulated basis set of PRESS TE = 0 ms. **B**: 'SNR' = 46 with PRESS TE = 25 ms basis set. **C**: 'SNR' = 72 for semi-LASER TE = 40 ms acquired basis set. Although a short TE PRESS basis set is a good approximation to fit semi-LASER acquisitions the importance of having the exact same parameters (RF pulses used, pulse length…) on the basis set (Simulated or acquired) and the experimental data is here appreciated. Residuals can be seen on top of the spectra. The better the fit, the smaller residual and better concentrations estimation.

4.7.2 Acquired basis set for semi-LASER

The basis set for the 7 T semi-LASER LCModel analysis included the acquired spectra of 13 metabolites: Alanine (Ala), Asp (Asp), Creatine (Cr),

Phosphocreatine (PCr), γ-Aminobutyric Acid (GABA), Glucose (Glc), Glutamine (Gln), Glutamate (Glu), Glutathione (GSH), Lac (Lactate), myo-Inositol (mI), N-Acetylaspartate (NAA) and Taurine (Tau); and the simulated spectra of 5 metabolites: Phosphocholine (PCh), Glycerophosphocholine (GPC), N-Acetylaspartylglutamate (NAAG), scyllo-Inositol (Scyllo) and Glycine (Gly). Simulations were performed with the Simulation Toolbox of the FID-A software package (https://github.com/CIC-methods/FID-A) that uses spin-system definitions published by (Govindaraju, Young, and Maudsley 2000).

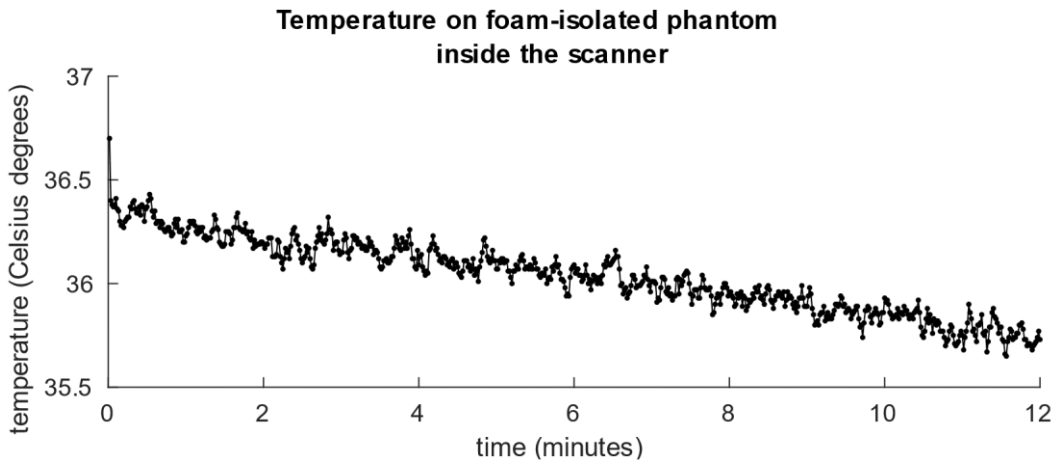

Figure 17: Decay of the temperature on the foam-isolated phantom over time inside the 7 T scanner, measured with an optic thermometer. The decay is less than 1 degree Celsius during the 10-minutes total acquisition time needed for each phantom (including pre-acquisition adjustments as frequency adjustment and shimming, and acquisition of water-suppressed and water-unsuppressed spectra).

Each metabolite was dissolved in a 100-ml phantom containing the LCModel stock solution (http://s-provencher.com/lcm-manual.shtml) and pH was carefully calibrated to pH = 7.2 with a pH-meter. **Table 5** indicates vendors and concentrations used. Each phantom was warmed to 37°C on a water bath and its temperature during measurement was kept constant by isolating the phantom with a foam shell. **Figure 17** shows the decay of the temperature on a phantom

over time inside the scanner, measured with a wired optic thermometer (FOT Lab Kit Fluoroptic Thermometer, Luxtron®) adhered to the phantom.

metabolite	Allowed LCModel name(s)	Concentration (mM)	Manufacturer	Product Number
L-Alanine,	Ala	100	Sigma	A7627
L-Aspartic acid	Asp	40	Sigma	A9256
Creatine	Cr, Cre	50	Fluka	27890
Phosphocreatine	PCr	50	Sigma	P7936
γ-Aminobutyric acid	GABA	200	Sigma	A2129
D-(+)-Glucose	Glc	200	Sigma	49139
L-Glutamine	Gln	100	Fluka	49419
L-Glutamic acid	Glu	50	Fluka	49449
L-Glutathione reduced	GSH	70	Sigma	G4251
Sodium L-lactate	Lac	100	Aldrich	71718
myo-Inositol	Ins, mI	200	Sigma-Aldrich	57570
N-Acetyl-L-aspartic acid	NAA	50	Sigma-Aldrich	920
Taurine	Tau	200	Sigma	T0625
LCModel stock solution				
3-trimethylsilyl-1-propanesulfonic acid sodium salt		1	Sigma	178837
Sodium formate		200	Fluka	71540

Table 5: List of metabolites with concentrations and vendors' references used for the acquired basis set. Each metabolite was dissolved on a phantom containing 100 ml of the LCModel stock solution. The stock solution contained 3-trimethylsilyl-1-propanesulfonic acid sodium salt, NaFormate and 1 g/L NaN3 dissolved on PBS. 2 liters of stock solution were prepared.

A dielectric pad was positioned around the foam shell to improve B_1 homogeneity. Two sand bags filling the gap on the coils ensured that the phantom was always placed on the same position. For each phantom a 16-averaged water-suppressed spectrum was acquired (semi-LASER, TE = 40 ms, TR = 10000 ms). Details of the procedures to generate the basis set can be found in the LCModel User's Manual (http://s-provencher.com/lcm-manual.shtml). **Figure 18** shows the acquired 13 model spectra**.**

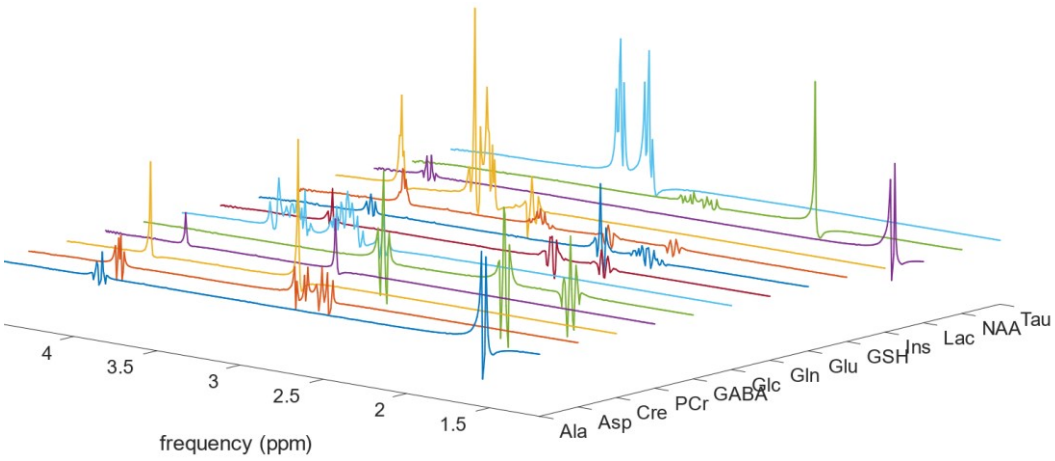

Figure 18: Acquired model spectra for the semi-LASER basis set.

4.8 MRS post-processing

The following section presents different post-processing strategies that were tested in order to improve spectral quality.

4.8.1 Eddy currents correction

Fast switching of gradients and/or high amplitude gradients induces so-called eddy currents. Faraday's law of induction states that a time-varying magnetic field generates an electrical current in conducting materials. In the magnet, the currents are, thus, generated on the nearby conducting structures as the cryostat, heat shields, magnet and shim coils. The gradient-induced currents on these structures generate in turn a new time-varying magnetic field. Therefore, the resultant gradient present during an MR acquisition is the sum of the main gradient and the second generated gradient. If eddy currents are not eliminated or compensated for, the resultant NMR spectrum is distorted.

In our fMRS experiments a pair of water suppressed (metabolic, MET) and unsuppressed (water, WAT) spectra was always acquired from every voxel position in order to have a water reference to perform water scaling for absolute

quantification with LCModel. To correct for eddy currents on our MET and WAT spectra the phase (φ_{wat}) of the mean WAT spectrum was calculated and applied to every single free induction decay (FID; i.e., the descending portion of the spin echo) S according to (Klose 1990):

$$s_{ecc} = s_0 e^{-i\varphi_{wat}} \quad [29]$$

where S_0 and S_{ecc} are the original and the corrected signal, respectively.

4.8.2 Coil channel combination

In Chapter 2 of this dissertation, the NMR signal acquisition was briefly explained. The receiver coil can be made of a single channel or a combination of channels, what is also called phased-array channel coils. The reason for having more than one channel is to increase the SNR, because the signal from each channel adds up, while the noise remains random. The signal that each of the channel receives depends on the distance and the orientation of the voxel of interest from the channel. The individual signals recorded with each channel must be magnitude and phase weighted before being added, in order to maximize the SNR that we can obtain.

There are different methods for weighted channel combination and the weights from each channel are usually calculated from the mean WAT spectra of each channel. We compared the performance of adaptive combine (Brown 2004) and Singular Value Decomposition (SVD) (Rodgers and Robson 2010) recombination. The mean SNR was very similar for both techniques, although slightly higher for SVD (**Table 6**). Therefore, we chose SVD for the post-processing of our experiments.

volunteer	ECc no Channel Weight	Adaptive Combine	SVD
1	287,68	395,15	396,37
2	220,19	306,11	307,73
3	248,12	329,67	330,71
4	287,68	396,06	398,64
5	220,93	318,04	318,30
6	263,89	342,47	345,78
Mean	**254,75**	**347,92**	**349,59**

Table 6: SNR of the averaged spectra after channel combination. SNR has been calculated from the creatine peak of the averaged spectra of 6 volunteers (visual cortex, semi-LASER, TR/TE = 4000/40 ms, n_{rep} = 320). Eddy currents corrected spectra were channel combined with no weighting, adaptive combine, and SVD. The mean SNR increased by a factor of 1.36 and 1.37 for adaptive combine and SVD, respectively.

4.8.3 Frequency drift correction (FDC)

The residual water peak position was determined from the (frequency domain) maximum of the real part in each individual scan and shifted to 4.7 ppm by applying to the time domain (Helms and Piringer 2001):

$$S_{fc} = S\, e^{i \cdot 2\pi \cdot \Delta\nu \cdot t} \qquad [30]$$

where S is the initial time domain signal (after the previous steps of eddy currents correction and channel coil combination), S_{fc} the frequency drift corrected signal, and $\Delta\nu$ is the obtained frequency shift in Hz. An example of a spectrum before and after frequency drift correction is presented on **Figure 19**.

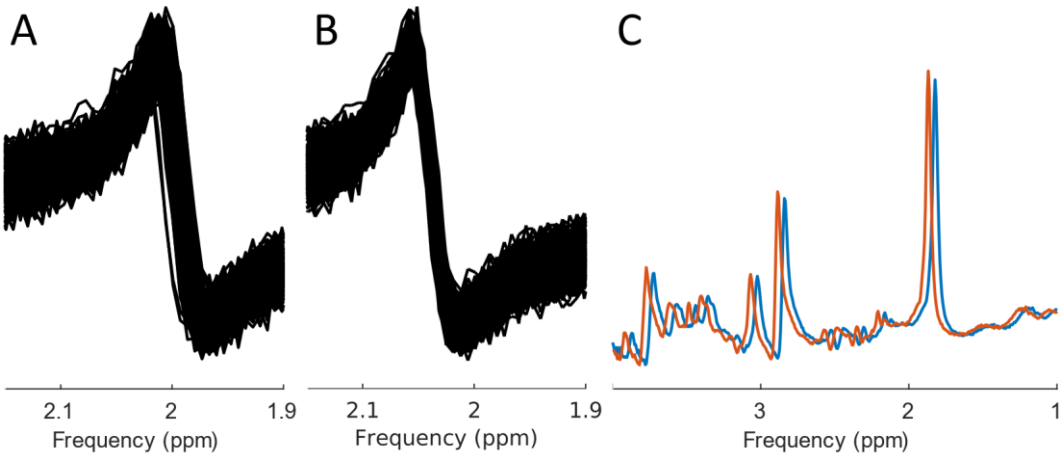

Figure 19: Frequency Drift Correction (FDC). Zoom on the NAA peak of the overlay of 320 individual acquisitions before **(A)** and after **(B)** the FDC. On the averaged spectrum **(C)** the linewidth of the peaks after FDC become narrower and the intensities higher (red) compared to the uncorrected spectrum (blue).

4.9 Visual stimulation paradigms and BOLD response maps

The main goal of this dissertation is to study the underlying metabolic response of different BOLD responses by using fMRS. For that purpose, a strong and wide enough BOLD activation must be achieved and localized at first, in order to allow placing an 8-ml voxel for the subsequent fMRS experiments. Different visual stimulation paradigms were tested for that purpose. Visual stimulation paradigms were programmed with Presentation® (Neurobehavioral Systems Inc). Three different visual stimuli were prepared: full-field flickering checkerboard and moving stars (Huk, Dougherty, and Heeger 2002) for a Positive BOLD Response (PBR) and centered small flickering checkerboard for a Negative BOLD Response (NBR) **(Figure 20).** Various paradigms alternating stimulation and rest periods with different timings were programmed for each experiment. The presentation during the rest periods consisted on a fixation cross for the checkerboards and a fixation point for the moving stars visual challenges. Every paradigm included a

randomly changing colored dot in the center to track the attention of the volunteers. **Figure 20** shows the extent and the amplitude of the BOLD response (activation maps and time courses) with moving stars and flickering checkerboard paradigms at 7 T for a given volunteer (female, 26 years old). both paradigms induce similar activation on primary visual cortex and both are equally valid for experiments of the Positive BOLD Response (PBR). The activation map for a Negative BOLD Response with a small centered flickering checkerboard is also shown. Maps are calculated with SPM after a gradient echo (GRE) Echo-Planar Imaging (EPI) BOLD sequence and overlaid on a 3D MP2RAGE (Marques et al. 2010) T1 image on three orthogonal slices. PBR maps and time courses are represented in red and NBR in blue.

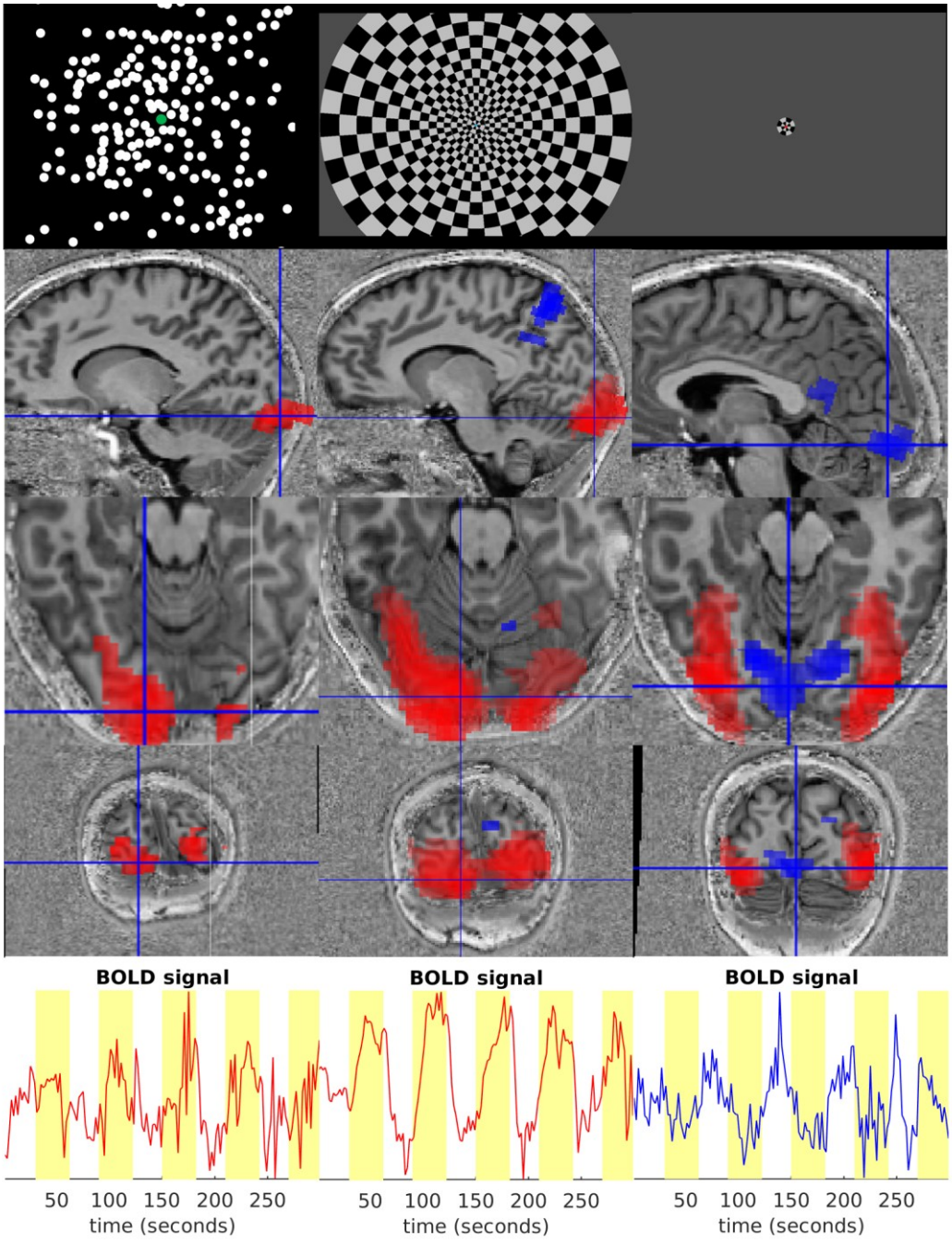

Figure 20: BOLD activation maps and time courses with the three visual stimuli (TOP) used on a representative volunteer (female, 26 years old, 7 T). LEFT, CENTER, and RIGHT columns correspond to the moving stars, flickering checkerboard and small flickering checkerboard respectively. PBR is shown in red and NBR in blue. Overlays with the activation maps and T1-weighted mp2rage anatomical images are shown on sagittal, transversal and coronal slices for the three stimuli. Yellow boxes on the time courses indicate when the stimulus was presented (BOTTOM).

Chapter 5

3T and 7T fMRS with Diverse Duration of Stimuli

5.1 Purpose

During the last decade, several functional magnetic resonance spectroscopy (fMRS) studies have been performed to characterize the relationship between neuronal activation and energy or neurotransmitter metabolism (see Chapter 3, 3.4). Due to higher SNR and chemical shift dispersion offered at 7 T, dynamic changes of metabolite concentrations in the human brain were successfully detected in response to visual, motor, or auditory stimulation (Mangia, Tkác, et al. 2007; Y. Lin et al. 2012; Schaller et al. 2013; Schaller et al. 2014). The goal of the present study was to characterize the detection limits of metabolic changes and their correlation with activation by a visual stimulus at a lower, but more widespread magnetic field strength of 3 T as compared with 7 T.

The current chapter performs a detailed analysis with a group of volunteers to whom different kinds of visual stimulation are presented in different order. A comparison between short and long blocks (32 seconds and 5 minutes) of stimulation paradigm and between high and low field strength (3 T and 7 T) is performed.

5.2 Methods

5.2.1 Participants and NMR scanners

All participants gave informed written consent prior to the experiments, which had been approved by the Ethics Committee of the University of Leipzig. 9 healthy volunteers (6 women and 3 men, age range 21-33 years) participated in the **3 T study** and scans were performed on a MAGNETOM Verio system (Siemens Healthcare, Erlangen, Germany) with a transmitter body coil and a 32-channel receive head-coil. For the **7 T measurements**, 14 healthy volunteers (5 women and 9 men, age range 22-33 years) participated and scans were performed on a MAGNETOM 7 T scanner (Siemens Healthcare, Erlangen, Germany) with a single-channel transmit/32-channel receive radiofrequency (RF) head coil (Nova Medical, Wilmington, MA, USA).

5.2.2 Visual stimulus and fMRI acquisitions

The stimulus used for fMRI and fMRS at 3 T consisted of a moving stars paradigm (Huk, Dougherty, and Heeger 2002) and, at 7 T, of a full-field radial 25.5% grey/black flickering checkerboard (**Figure 20**). On both cases an additional colored fixation point was added, which changed its color randomly (red, blue, purple, green, yellow) during the task, in order to keep track of the attention of the volunteers via a response button. The rest periods consisted on a fixation cross (for the flickering checkerboard) and a dot (for the moving stars) on a grey background. A block design (5 repetitions) with alternation of 30 seconds of rest and 30 seconds of activation during gradient-echo EPI scanning (TE 30 ms, TR 2 sec) was used as a functional localizer and a standard SPM12 processing scheme was employed to obtain BOLD activation maps (**Figure 20**). The preprocessing steps included realignment, slice-time correction, and spatial smoothing using an 8 mm FWHM Gaussian kernel.

5.2.3 fMRS acquisitions

Localization of a single 8ml voxel for fMRS was done by co-registration of the thresholded BOLD activation map to an anatomical image (MPRAGE at 3 T and MP2RAGE at 7 T). **At 3 T**, the fMRS acquisition was done with a PRESS sequence (Bottomley 1987) (TE/TR = 30/2000 ms, 16-step phase cycle, 640 repetitions, 21:28 min). **At 7 T**, a semi-LASER sequence (Öz and Tkáč 2011; Scheenen et al. 2008) (TE/TR = 40/4000 ms, 4-step phase cycle, 320 repetitions, 22:22 min) was used. The twice as long TR needed for semi-LASER with respect to PRESS provoked that the number of repetitions at 7 T were reduced to half compared to those acquired at 3 T in order to keep the total stimulus duration constant. On either cases (3 T and 7 T) first- and second-order shims were adjusted using FAST(EST)MAP (Gruetter 1993; Gruetter and Tkáč 2000), and a water-unsuppressed spectrum (16 repetitions, 0:40 min at 3 T and 1:26 min at 7 T) was acquired to perform water scaling with LCModel (Provencher 1993) for absolute quantification. The rest/stimulus (REST/STIM) block lengths employed for the fMRS paradigm were 5.3 minutes long for the "long" blocks and 32 seconds long for the "short" blocks. In the rest of the chapter we refer to them as LONG and SHORT respectively. Each LONG block contained 160 or 80 repetitions at 3 T and 7 T, respectively, and each SHORT blocks contained 16 or 8 repetitions at 3 T or 7 T, respectively.

At 3 T, each volunteer was subjected on every session to the two fMRS paradigms (LONG and SHORT) with auto alignment of the MRS voxel in between. The participants performed the complete fMRS study twice, inverting the order of the stimulus presentation (1st LONG and 2nd SHORT and vice versa) to account for potential adaptation effects. One volunteer repeated the experiment in the same order (two times first SHORT and second LONG). One SHORT measurement from one volunteer and two LONG from 2 volunteers needed to be discarded due to insufficient attention to visual presentation. In total, 16 measurements were

available for the LONG blocks study (6 times 1st LONG and 2nd SHORT + 10 times 1st SHORT and 2nd LONG) and 17 for the SHORT blocks study (8 times 1st LONG and 2nd SHORT + 9 times 1st SHORT and 2nd LONG).

At 7 T, the full group of subjects (14) participated in the LONG blocks experiment while only 8 subjects participated in the SHORT blocks experiment.

5.2.4 Post-processing and analysis

Siemens raw data (TWIX format) were post-processed in MATLAB as described in detail in the methods chapter of this dissertation (Chapter 4, 4.8 MRS post-processing): eddy Current correction, SVD channel coil combination and frequency drift correction were done in that order.

In order to have sufficient SNR for quantification, for the water-suppressed SHORT blocks spectra, the signals acquired during a REST condition were averaged together separated from the signals acquired during a STIM condition, thus having two spectra for LCModel per volunteer, each of which was the mean of 320 averages at 3 T and 160 averages at 7 T. That same averaging was also applied to the LONG acquisitions, to have a direct comparison SHORT vs. LONG.

As explained by Ip et al. (Ip et al. 2017) functional MRS studies have previously excluded up to 50% acquired of data to obtain stable metabolite measurements, by using the second half of prolonged visual stimulation blocks (Mangia et al. 2006; Mangia, Tkáč, et al. 2007; Schaller et al. 2013; Bednařík et al. 2015) or focused on specific experimental cycles (Just et al. 2013). Under the assumption that metabolite spectra are unstable during the period where the BOLD-amplitude is known to peak (Buxton et al. 2004). Ip et al. (Ip et al. 2017) excluded 12.5 % of the data. In our averaging approach, 0% of the data is excluded both for the LONG and the SHORT acquisitions for the 3 T and 7 T data.

Metabolite quantification was performed with LCModel (Provencher 1993), using water as internal reference by performing water scaling with the unsuppressed water acquisition. For the 7 T semi-LASER acquisitions, the mixed acquired-simulated LCModel basis set described previously on the methods chapter was used (see Chapter 4, 4.7.2 Acquired basis set for semi-LASER). For the 3 T PRESS acquisitions, the LCModel basis set included the simulated spectra of 17 metabolites: Ala, Asp, Cr, PCr, GABA, Glc, Gln, Glu, GPC, PCh, GSH, Ins, Lac, NAA, NAAG, Scyllo and Tau. **Figure 3** shows examples of LCModel fits for 3 T PRESS (320 averages) and 7 T semi-LASER (160 averages).

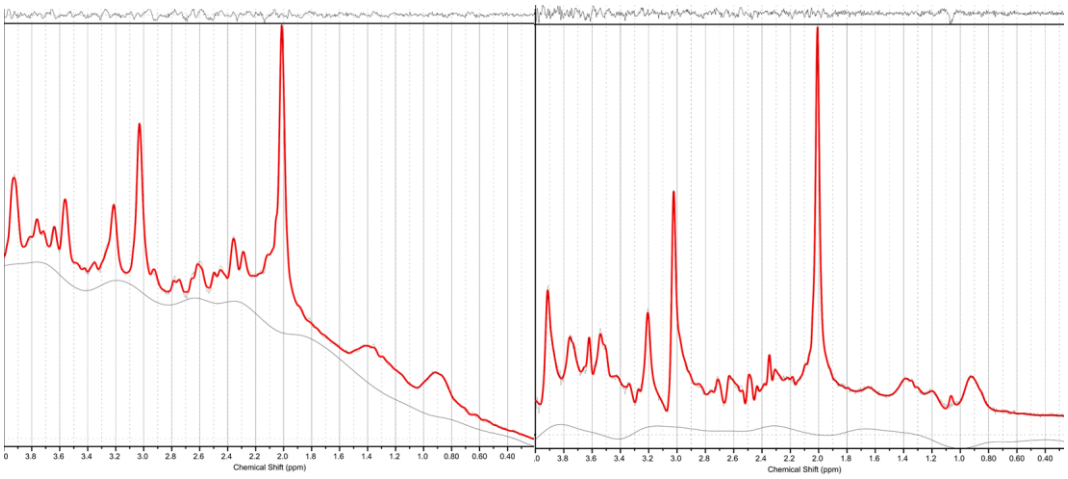

Figure 21: LCModel fit of the mean spectrum acquired during a REST condition at 3 T (LEFT) and 7 T (RIGHT).

As (de)activation-related metabolic changes were expected to be rather subtle according to previous fMRS studies, a step-wise procedure was adapted to identify fits of sufficient quality for inclusion in the final analysis: *(i)* spectra with a full width at half maximum (FWHM; as reported by LCModel) exceeding 16 Hz were completely rejected (i.e. no concentration estimate for any metabolite was included in further analyses). *(ii)* A concentration estimate of an individual metabolite in a single spectrum was only included if its Cramér-Rao lower bound

(CRLB; as reported by LCModel) was below 40%. *(iii)* If criteria 1 and 2 were not fulfilled for a particular metabolite in at least 50% of all analyzed spectra then this metabolite was excluded from further analysis for this type of experiment (i.e. SHORT or LONG blocks, 3 T or 7 T).

For each group of analysis, the investigations of stimulus-related metabolic changes consisted of a paired-sample t-test to assess the concentration differences between spectra acquired during the REST and the STIM condition (significance level set to $p = 0.05$).

In addition, the mean stimulus-related percent BOLD-signal change during the functional localizer was calculated with SPM12 in a volume that was adjusted in size to the spectroscopy voxel for each volunteer and (linearly) correlated with metabolic results from the fMRS experiments. These correlation analyses included averaged metabolite concentration changes during STIM compared to REST (for 3 T and 7 T, SHORT and LONG blocks).

5.3 Results

Figure 22 shows the mean concentration changes for each metabolite on each group of analysis and **Figure 24** the individual [Glu] changes.

At 3 T, no significant concentration changes were observed during the SHORT blocks from the full group of analysis while a significant increase of glutamate of 5.14% ($p < 0.001$) and a significant decrease of glucose of -10.85% ($p = 0.022$) appeared during the LONG blocks. However, a significant positive correlation of the glutamate percentage of signal change with the BOLD percentage of signal change during the SHORT paradigm was found (correlation coefficient $R = 0.54$, $p = 0.031$, **Figure 23**).

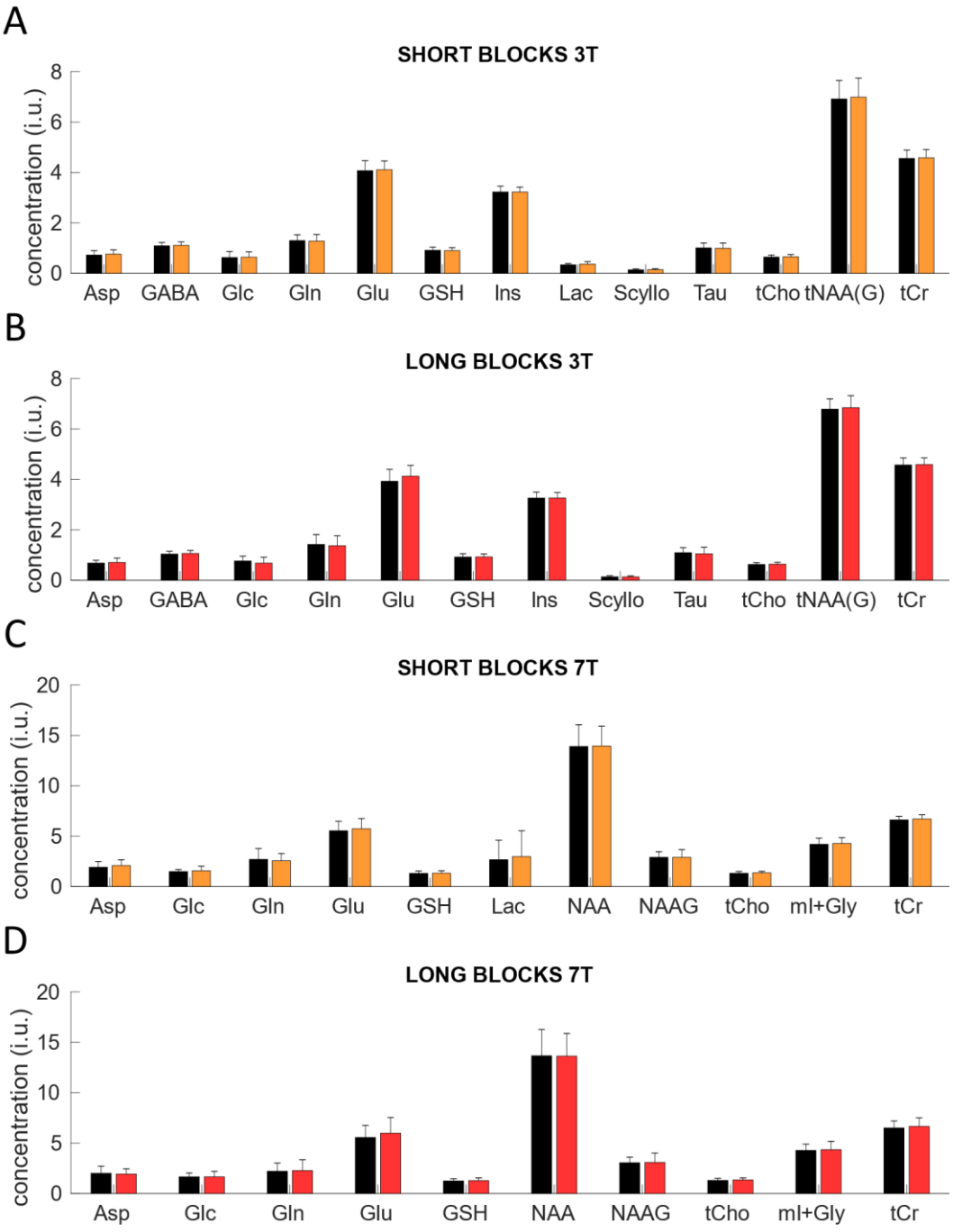

Figure 22: Mean inter-subject metabolic concentrations during the SHORT and LONG blocks stimulation paradigms at 3 T and 7 T. **A** and **B**: 3 T SHORT and LONG blocks, respectively. **C** and **D**: 7 T SHORT and LONG blocks, respectively. Black bars represent the mean concentrations during the REST periods while colored bars during the STIM periods (orange: SHORT, red: LONG). Error bars indicate one standard deviation of the mean values

Performing the statistical analysis after dividing the group of SHORT and LONG according to the order on which the paradigm was presented, the results were found to be slightly different:

- When the SHORT blocks paradigm is presented first, a significant increase of glutamate during the SHORT blocks is detected (+1.58%, p = 0.039), whereas during the LONG blocks the significant increase of glutamate remains (+5.70%, p = 0.017) and the decrease of glucose loses significance (-10.95%, p = 0.141).
- When the SHORT blocks come second, GABA increases significantly by 5.6% (p = 0.005) during the SHORT blocks, with the increase of glutamate being still significant during the LONG blocks (4.29%, p = 0.015) while again the decrease of glucose during the LONG blocks is not significant anymore (-10.76%, p = 0.129).

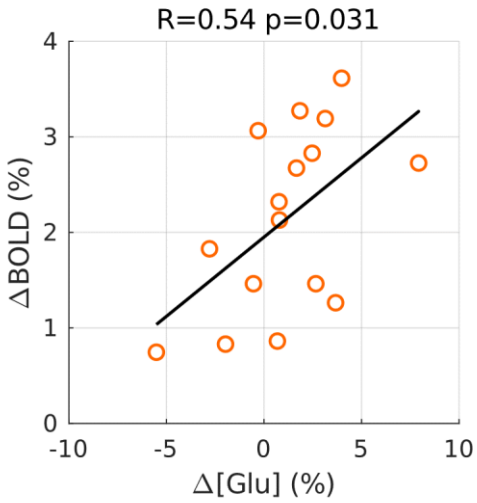

Figure 23: Correlation of the Glutamate concentration change with the BOLD response during the SHORT paradigm at 3 T.

At 7 T, the SHORT blocks show significant increases of glutamate and aspartate of 3.60% (p = 0.004) and 8.78% (p = 0.014), respectively. During the LONG blocks, the only significant concentration change is an increase of 7.61% of glutamate (P = 0.042).

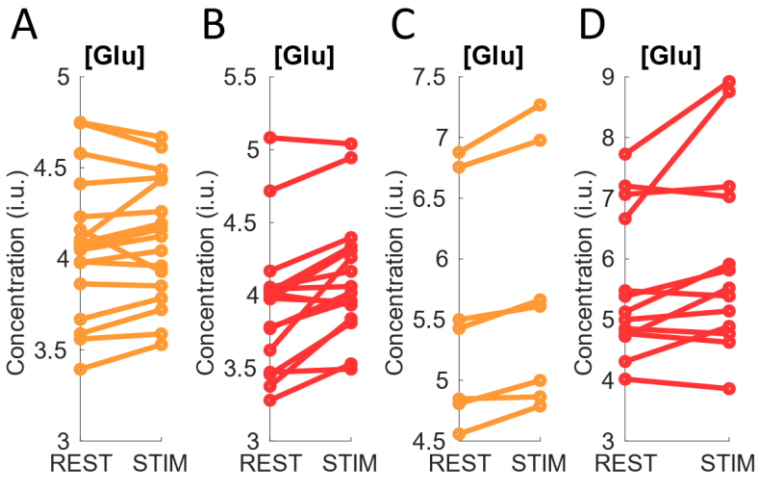

Figure 24: Individual [Glu] changes at 3 T and 7 T. Orange indicates measurement during the SHORT paradigm while red during the LONG paradigm. **A** and **B:** 3 T moving stars. **C** and **D:** 7 T flickering checkerboard.

5.4 Discussion

A robust significant increase of glutamate was observed independently of field strength and paradigm, which is consistent with previously published literature that used LONG blocks stimulation paradigms at high fields (Mangia, Tkác, et al. 2007; Y. Lin et al. 2012; Schaller et al. 2014; Bednařík et al. 2015; Ip et al. 2017). Increases of glutamate concentration ([Glu]) during functional activation do not directly reflect synaptic Glu release but represent adaptations of cerebral Glu metabolism and production (Mangia, Tkác, et al. 2007; Y. Lin et al. 2012; Schaller et al. 2014; Bednařík et al. 2015; Ip et al. 2017). The changes of [Glu] that we observed with the different conditions are within the range of reported changes

from those studies (2-12%). At 3 T with the moving stars paradigm, the changes observed during the LONG blocks are relatively consistent independently on the order on which the stimulus is presented (4.29% and 5.70% when the paradigm was presented first or second, respectively), suggesting that the REST periods of this paradigm are sufficient in length to recover basal conditions. It is also an indication of being a rather strong effect that remains quite consistent independently of the group size (the full group showed a mean increase of 5.14%) and can be used as a marker of regions of neuronal activation. With regards to the SHORT blocks, it is interesting to note that the increase is only significant when the SHORT paradigm was the first that was presented to the volunteers, being smaller (+1.58%) compared to the increased that occurred during the LONG paradigm on any of the situations previously described (4.29%, 5.70% or 5.14%). This could be an indication of two things: on one side, the basal concentration levels of glutamate might not have been recovered after presenting the LONG paradigm. Additionally to the inter-paradigms time (a few seconds), the LONG paradigm possesses a first REST period of 5.33 minutes while the first REST period of the SHORT paradigm is only 32 seconds. Therefore, the order on which the stimulus is presented to the volunteers seems to be relevant for this kind of studies. On the other side, the extent of metabolic activation with 32 seconds blocks appears to be smaller compared to the 5.33 minutes blocks.

Concerning the correlation of the percentage of glutamate concentration changes with the percentage of BOLD signal change, the positive correlation that we observed during the SHORT blocks at 3 T ($R = 0.54$, $p = 0.031$) is in line with the results obtained by (Bednařík et al. 2015) for 5 minutes blocks and (Ip et al. 2017) for 64 seconds blocks, corroborating Glu as a marker of the BOLD response and neural activation. The reason for not observing a significant correlation at 7 T could be due to the smaller group size. A bigger group combining different types of BOLD responses shows a significant correlation with the percentage of [Glu] change at 7 T on Chapter 7 of this dissertation. Regarding the bigger group at 3 T,

it could be the case that the percentage of change of [Glu] and BOLD is very well coupled for similar block lengths (32 seconds for fMRS and 30 seconds for fMRI) as observed by (Ip et al. 2017) and less correlated (and not significant under the detection limits of 3 T) during the LONG blocks (e.g. the higher SNR achievable at 7 T, with a bigger group of subjects, would help to obtain a significant correlation during the LONG blocks).

At 7 T, the changes observed are still within the previously mentioned range of 2 to 12% and are larger during the LONG paradigm (8.78) than during the SHORT paradigm (3.60%), as in the 3 T experiments.

Besides limitations in the precision of the measurement of relatively small concentration changes, some variability in the results from different studies may be due to differences in the employed stimuli and paradigm design, or in MRS acquisitions and post-processing. Varying degrees of partial voluming are further likely contributors to inter-study and inter-subject variability.

Despite the variability, both at 3 T and 7 T the [Glu] changes seem to be larger during the LONG paradigm than during the SHORT paradigm. And in turn, the increases at 7 T appear to be larger than those at 3 T. As explained previously on this dissertation (see Chapter 4, 4.9 Visual stimulation paradigms and BOLD response maps), for a study in which participants are exposed repeatedly to the same visual stimulus (four times in this case at 3 T, LONG and SHORT twice with reverse presentation order) a less demanding stimulus for the eyes was chosen (i.e. the moving stars). The level of comfort of the stimulus was assessed by collecting feedbacks from volunteers and it was ensured that the extent of BOLD activation was similar for both checkerboard and moving stars conditions (see Chapter 4, 4.9 Visual stimulation paradigms and BOLD response maps). Although the mean amplitude of the BOLD response (percentage of signal change) is similar with both paradigms (**Figure 20**) the underlying metabolic changes with the two paradigms possibly varies. That may be the one explanation for the larger changes in

glutamate at 7 T compared to 3 T. The different MRS acquisition used at 3 T and 7 T in our study (PRESS and semi-LASER, respectively) could be a source of variability on the estimated basal concentrations but shouldn't have an effect on the calculated percentage of concentration change during STIM with respect to REST. Furthermore, the same post-processing steps were applied to all acquisitions so that is not expected to represent a source of variability.

Overall, the 32-seconds SHORT blocks seem to be long enough to detect [Glu] changes and shorter stimulation blocks would help to identify the limits on which Glu can be a marker of this kind of brain activation.

Aforementioned studies of fMRS at high fields detected increases of [Glu] concomitant to decreases of the concentration of glucose ([Glc]) during functional stimulation indicating enhanced glycolytic flux. This is confirmed for lower fields on our results, where a significant decrease of -10.85% is observed during the LONG blocks.

At 3 T, on the subgroup of volunteers subjected to the SHORT paradigm presented after the LONG paradigm, an unexpected increase of GABA concentration ([GABA]) is observed. Any [GABA] changes related to neurotransmitter release wouldn't be detected by fMRS as in the case of glutamate. However, previous studies detected a negative correlation of basal [GABA] with the amplitude of the BOLD response (Bednařík et al. 2015) and decreases of [GABA] during stimulation with respect to the control condition (Mekle et al. 2017) supporting the role of inhibitory/excitatory balance in modulation of BOLD-fMRI responses (Muthukumaraswamy et al. 2009; Muthukumaraswamy et al. 2012; Donahue et al. 2010). Hence, we would expect to observe a decrease in [GABA] during the stimulation blocks of our paradigm. Nevertheless, it is interesting to note, that the significant increase in [GABA] is happening in the situation when no significant increase if [Glu] was found. For a tentative explanation of our observed

[GABA] increase, we can consider the aforementioned accepted hypothesis that the increases of [Glu] during activation are a reflection of increased neuronal activity over a baseline level. Increased metabolic neuronal activity implies an increased tricarboxylic acid (TCA) cycle rate to which Glu is linked via dynamic exchange with α-ketoglutarate. Being Glu a precursor of GABA on GABAergic neurons (Walls et al. 2015), an increase of [GABA] during stimulation could be an indication of increased metabolic activity on GABAergic interneurons, occurring after the new steady state is reached (after the LONG paradigm) and no net increase of [Glu] (from the larger pool of glutamatergic neurons with respect to GABAergic neurons) (Sahara et al. 2012) is observed anymore. Nonetheless, there are some weak points about this result. A better identification of GABA should be done with editing techniques as MEGA (Mullins et al. 2014) and since this effect was only observed for this condition for this small group, a larger statistic would be needed in order to discard the possibility of a false positive finding. In any case, the underlying condition (SHORT paradigm after the LONG paradigm) is new compared to previous studies. Moreover, a non-significant tendency of GABA to increase has been observed during activation of human visual cortex (Y. Lin et al. 2012) and a significant increase was found on motor cortex (Chen et al. 2017) Further investigations will help to understand the roles of GABA as a marker of activation.

Apart from the increases in [GABA] at 3 T, the other confounding factor is the increase of the aspartate concentration ([Asp]) during the SHORT paradigm at 7 T. This contradicts our and previous findings of decreased [Asp] during the LONG blocks (see Chapter 7, 7.4 Discussion for a brief discussion about the metabolic relevance of Asp). Again, this might have been an incidental finding only observed in the smaller group that is subjected to SHORT paradigm at 7 T, and again further experiments are needed to clarify this issue.

.

5.5 Conclusion

The aim of this chapter was to compare two stimulation paradigms at two different field strengths and explore the metabolic changes observable by fMRS. We conclude that:

1. Glutamate is confirmed to represent a robust marker of neuronal activation independently of field strength and paradigm used, showing significant increases on the statistical REST to STIM comparisons, and a positive correlation with the amplitude of the BOLD response (as previously observed in the literature at higher fields) on one of the cases of study (larger sample sizes would help to observe this correlation on further studies).
2. With regards to the metabolic response, no significant changes seem to discern stimulation paradigms made of 32 seconds blocks from paradigms made of 5 minutes blocks. Shorter stimulation blocks would identify the limits from which the metabolic changes can be detected by fMRS.
3. Longer blocks and higher field strengths (on which the extent of the observed concentration changes was larger) would help to improve the sensitivity for the detection of very small metabolic changes. Moreover, in the case of glutamate, higher fields would help to discern its overlapping resonance peaks from glutamine.
4. Additional experiments will help to clarify the unexpected changes observed for GABA and aspartate.

Chapter 6

Short-blocks fMRS with Periodic Averaging

6.1 Purpose

On the previous chapter of this dissertation significant metabolic changes were observed during LONG blocks (5 minutes) stimulation paradigms at 3 T and 7 T as formerly published in the literature at 7 T (Mangia, Tkác, et al. 2007; Y. Lin et al. 2012; Schaller et al. 2013; Bednařík et al. 2015). However, shorter stimulation blocks (what we called SHORT, 32 seconds) led to a significant increase of glutamate at 7 T and at 3 T when that paradigm was presented first, but not for the whole group of subjects. The importance of the length of the stimulation relays on the physiological information that we can obtain. To track the metabolic changes that occur during a BOLD response and use fMRS as a more direct measurement of neuronal activation than fMRI, the same paradigm should be used. This has been made possible at 7 T, and at 3 T further experiments need to be done. To explore the limits of the shortest duration of stimulus that we could reach in order to detect significant metabolic changes, we develop here a novel paradigm design. The stimulation lasts a single TR, 4 seconds, and is followed by 8 TRs of REST. To ensure maximal SNR and temporal resolution the signals are averaged

periodically. We called this paradigm of ultra-short stimulation blocks: "uSHORT".

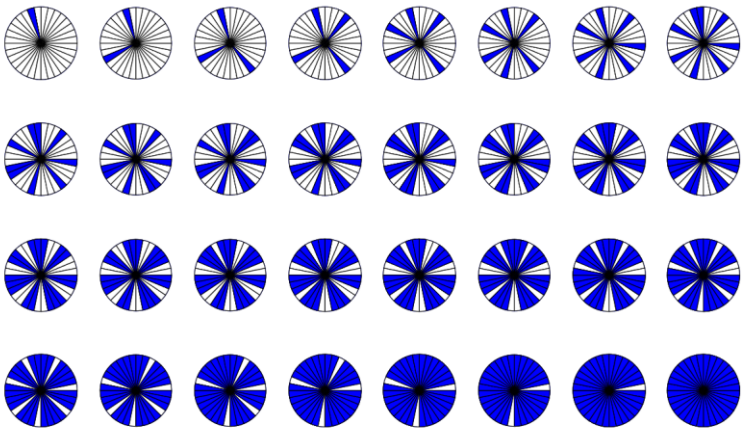

Figure 25: Concept of periodic averaging fulfilling a 32-steps phase cycling. Our visual stimulation paradigm consists of 9 TR on which the first 8 TR are REST condition and the stimulus is shown at TR 9. The STIM condition occurs at TRs: 9, 18, 27, 36… 288 (every 9 TRs, 32 times). Every time the condition STIM occurs a new step of the 32-steps phase cycle is complete, until achieving a full cycle after 9 * 32 = 288 acquisitions. The same applies for the rest of positions of the paradigm. *Position1* averages with the acquisitions: 1, 10, 19, 28… 280; *Position2* with the acquisitions: 11, 20, 29, 38… 281; *Position3* with: 12, 21, 30… 282; etc. At the end a 9-points time course is achieved, each point made of a complete phase cycle of 32 averages.

6.2 Methods

6.2.1 Periodic averaging of an fMRS paradigm

Figure 25 shows a schematic representation of how a periodic averaging of a 4, 8, 16 or up to 32 steps phase cycling acquisition fulfils the complete cycle while averaging always signals of the same position of the paradigm (REST: positions 1 to 8, STIM: position 9). For a 288 averages acquisition, each of the 9 points of the paradigm is averaged 32 times with a complete phase cycle. For our semi-LASER sequence (Öz and Tkáč 2011; Scheenen et al. 2008) with 4-steps phase cycling, each of the 9 points of the paradigm contains the average of 32 signals and 8 complete cycles of phase cycling. As explained in Chapter 4, phase cycling helps to eliminate

spurious signals and improves the quality of the acquired spectrum. This approach improves the temporal resolution to a single TR.

6.2.2 MR acquisitions, post-processing and analysis

12 volunteers (6 women and 6 men, age range 23-31 years) participated in the fMRS study. All participants gave informed written consent prior to the experiments, which had been approved by the Ethics Committee of the University of Leipzig. Scans were performed on a MAGNETOM 7 T scanner (Siemens Healthcare, Erlangen, Germany) with a 32-channel receive head-coil. The visual stimulation paradigm consisted of a full-field radial 25.5% grey/black flickering checkerboard (Chapter 4, 4.9 Visual stimulation paradigms and BOLD response maps, **Figure 20**) during the stimulation (STIM) periods, and a grey background with a centered fixation cross during the rest (REST) periods. To track the attention of the volunteers (via pressing a response button), during the fMRI acquisition a centered fixation point was randomly changing color (red, blue, purple, green, yellow) and during the fMRS acquisition they were asked to press every time the 4-seconds flickering checkerboard appeared. As in Chapter 5, a block design (5 repetitions) with alternation of 30 seconds of rest and 30 seconds of stimulus during gradient-echo EPI scanning (TE 30 ms, TR 2 sec) was used as a functional localizer. A standard SPM12 processing scheme was employed to obtain BOLD activation maps. Localization of a single 8 ml voxel for fMRS was done by co-registration of the thresholder BOLD activation/deactivation map to an MP2RAGE anatomical image.

A semi-LASER sequence (Öz and Tkáč 2011; Scheenen et al. 2008) (TE/TR = 40/4000 ms, 4-step phase cycle) was used for fMRS (288 repetitions, 20:10 min). First- and second-order shims were adjusted using FAST(EST)MAP (Gruetter & Tka 2000; Gruetter 1993), and a water-unsuppressed spectrum (16 repetitions, 1:26 min) was acquired to perform water scaling with LCModel for absolute

quantification. The fMRS paradigm consisted on 8 TRs with the REST condition (32 seconds) followed by 1 TR of the STIM condition (4 seconds), repeated 32 times up to 20 minutes. Each participant was subjected twice to the paradigm.

Siemens raw data (TWIX format) were post-processed in MATLAB as described in detail in the methods chapter of this dissertation (Chapter 4, 4.8 MRS post-processing), i.e. Eddy currents correction, SVD channel coil combination and frequency drift correction. Averaging was done following the concept of periodic averaging explained before. For each participant, the two fMRS acquisitions were treated separately, two 9-points time courses were obtained per volunteer. Each time point was the result of 32 averages of the same condition. The resultant group was n = 24 (twice the number of volunteers) time courses. As in Chapter 5, no data was rejected with the averaging criterion employed here, unlike previous studies (Ip et al. 2017; Mangia et al. 2006; Mangia, Tkác, et al. 2007; Schaller et al. 2013; Bednařík et al. 2015; Just et al. 2013).

Additionally, all individual signals were averaged following the 9-points periodic averaging and quantified with LCModel in order to have an averaged 9-points time course for visualization purposes. Each point was then the average of 32*24 = 768 FIDs (**Figure 26**, **Figure 27**).

Metabolite quantification was performed with LCModel, using water as internal reference by performing water scaling with the unsuppressed water acquisition. We used the same mixed (acquired and simulated) LCModel basis set as described in Chapter 5, the preparation of which is also detailed in: Chapter 4, 4.7.2 Acquired basis set for semi-LASER.

Unlike Chapter 5, where one mean REST to STIM statistical comparison was done for each group, here 8 comparisons in total were done. Each of the 8 REST conditions before the STIM condition were treated independently and compared one by one as REST1 to STIM, REST2 to STIM, … REST8 to STIM. Each comparison underwent a paired-sample t-test (n = 24 at REST vs. n = 24 at STIM for each metabolite, unless some rejection after the aforementioned quality

exclusion criterion). In order to avoid the appearance of false positives owing to multiple comparisons, the significance level was set to p = 0.01. No statistical analysis was performed to the inter-subjects mean time course (**Figure 27**).

6.3 Results

No significant concentration changes were observed for any metabolite for any of the conditions considered. **Figure 26** shows a typical LCModel fit on a single volunteer after the 32-averages periodic averaging and the fit of the mean REST1 after the inter-subject average. **Figure 27** shows the mean inter-individual glutamate concentration time course (FIDs from the different volunteers are averaged before applying LCModel quantification).

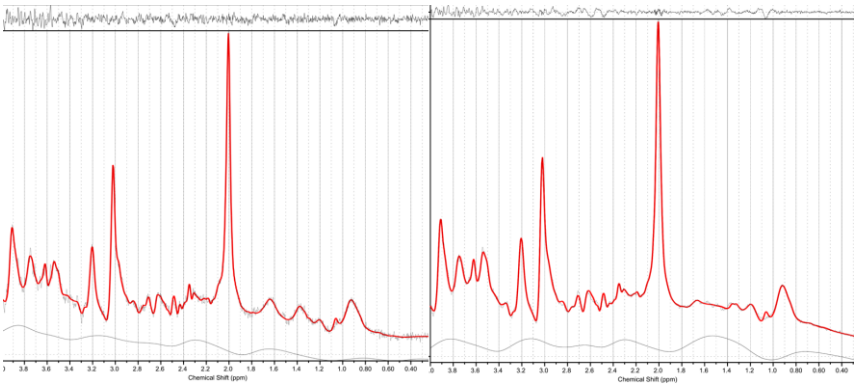

Figure 26: LCModel fits from a representative individual 32-averages mean (LEFT) and the REST1 from the mean inter-subjects averaging (RIGHT).

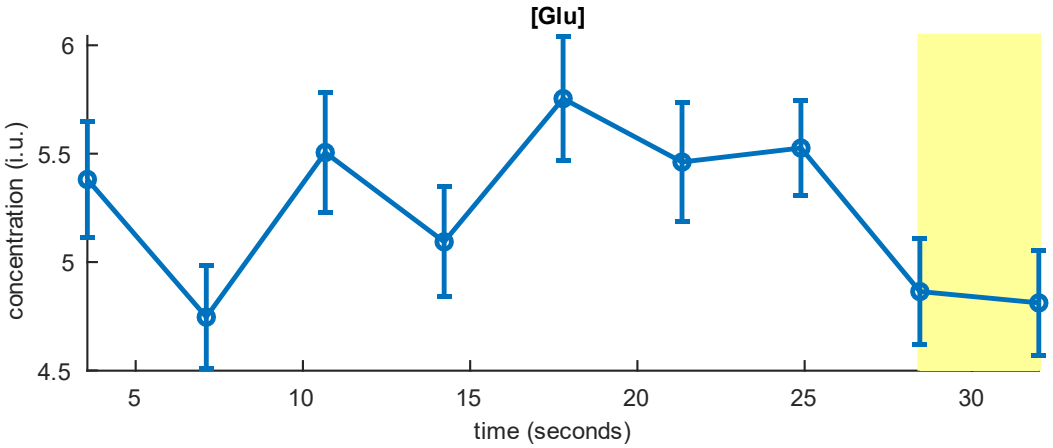

Figure 27: Averaged inter-volunteer glutamate concentration during the 9-steps periodic averaging. The yellow box indicates when the stimulus is presented. Error bars indicate the CRLB of the LCModel fit.

6.4 Discussion

The current experimental set up was not sensitive enough to detect any significant metabolic change. No significant changes of glutamate were observed during the stimulation periods. In light of this result, the stimulation period needed to detect significant changes of glutamate would be between 4 seconds and 32 seconds. An experiment with very short stimulation blocks is hampered by several limitations. In order to have a sufficient SNR and spectral quality for a reliable quantification, a certain number of averages must be acquired. That implies prolonging the acquisition time under a certain block condition (REST or STIM). The current experimental set up overcomes this issue by performing a periodic averaging, therefore the shortest STIM reachable corresponds to a single TR. The second limitation appears with the length of the TR itself. For this 7 T semi-LASER we used a TR = 4 seconds. This is a compromise needed for having a relatively short TE (40 ms) and avoid further signal loss from metabolites of interest with a very short T2. To shorten the TE, the amplitude of the RF refocusing pulses must be increased, leading to an increase in SAR. To avoid exceeding the SAR limits the TR must be increased. A longer TR of 5 or 6 seconds can help to

obtain shorter TE of 30 or 25 ms and get a better detection of metabolites like glutamate. But this would clearly come at the cost of a reduced temporal resolution, that was what this study wanted to improve. The third limitation is physiological. Since the dynamic of the concentration changes previously reported is not completely clear (i.e. in a 5 minutes blocks of STIM paradigm, the delay of the increase of glutamate concentration can happen after n seconds) our periodic averaging can partially dilute the effect. It could be the case that the increase after stimulation lasts more than 4 seconds and is not happening during the 9th step STIM. In any case, since significant changes were detected also during a 32-seconds STIM paradigm at 7 T with semi-LASER (Chapter 5), the hypothetical changes, could happen already in our 32-seconds/9-steps period. A different experimental set up should help to resolve this issue. Regarding the signal loss with a longer TE, sequences as SPECIAL (Mlynárik et al. 2006; Schaller et al. 2013; Schaller et al. 2014; Mekle et al. 2017) could help to get a TE up to 6 ms, but again the TR would probably increase back to 6 seconds or more. In any case, a simple explanation could be that 4 seconds stimulation does not provoke any activation. In this experiment we didn't look at the BOLD effect with an EPI sequence with such 4 seconds STIM and 32 seconds REST paradigm, so the degree of activation (i.e., the percent BOLD signal change) was not assessed. All the information that we had was with the same visual presentation but with longer stimulus (32 seconds).

Furthermore, the present 4-seconds STIM paradigm do not necessarily need to happen under an increase of [Glu]. Previous studies at 3 T observed decrease of glutamate concentration during repeated stimulus paradigms (Apšvalka et al. 2015).

Regarding other metabolites as glucose, for which some concentration changes have been previously discussed (Chapter 5), the fact that here around 30%

of its data is rejected after the quality filter might be one reason why it is difficult to observe significant changes.

6.5 Conclusion

Here we present a novel experimental set up that achieves a temporal resolution of a single TR and stimulation periods of only 4 seconds. No significant glutamate or other metabolite concentration changes were observed as opposed to longer visual stimulus as 32 seconds or 5 minutes. Further experiments would help to elucidate the limits of detection of fMRS.

Chapter 7

Dynamic Metabolic Changes in Human Visual Cortex in Regions with Positive and Negative BOLD Response

7.1 Introduction

As previously mentioned on Chapter 3, 3.2 blood oxygenation level-dependent (BOLD) functional magnetic resonance imaging (fMRI) is the most widely used method for studying human brain activity (Logothetis 2008) In the presence of a suitable stimulation paradigm, a *positive BOLD response* (also referred to as *'activation'*) is observed, defined as an increase of the BOLD signal over a baseline level. Correspondingly, the opposite direction of signal change is referred to as a *negative BOLD response* (or *'deactivation'*), that is, a decrease of the BOLD signal from a baseline level due to a stimulus or task. Deactivations have been observed both in animals and humans (Huber et al. 2014), in regions adjacent to activations during stimulation of motor (Allison et al. 2000; Hamzei et al. 2002; Stefanovic, Warnking, and Pike 2004; Newton, Sunderland, and Gowland 2005),

somatosensory (Hlushchuk and Hari 2006; Kastrup et al. 2008; Klingner, Huonker, et al. 2011), or visual areas (Tootell et al. 1998; Shmuel et al. 2002; Smith, Williams, and Singh 2004; Bressler et al. 2007; Pasley, Inglis, and Freeman 2007; Wade and Rowland 2010). Although initially hypothesized to just represent a mechanism of blood stealing in favor of regions of activation (Woolsey et al. 2017; Harel et al. 2002) later publications showed correlations of the negative BOLD response with neuronal activity (Shmuel et al. 2006) however, with a different neurovascular coupling than the positive response (Huber et al. 2014; Goense, Merkle, and Logothetis 2012).

While BOLD-fMRI, due to its relatively high sensitivity, is the method of choice for the vast majority of functional experiments in humans, it does not provide quantitative information on neuronal activation. When alterations of the neurovascular coupling are suspected, for instance, in comparisons of regions with different baseline physiology (Guidi et al. 2016), or in investigations of neuronal inhibition (Goense, Merkle, and Logothetis 2012), alternative non-invasive non-BOLD contrasts are required for a consistent interpretation of fMRI data or their modeling (Huber, Uludağ, and Möller 2017). Experiments yielding well-defined physiological parameters like cerebral blood flow (CBF) and volume (CBV) or metabolic measures, such as the cerebral metabolic rate of oxygen (CMR_{O2}) are, therefore, receiving increasing attention.

MRS methodologies are sensitive to different aspects of neuronal activation and provide a complementary tool for investigating the human brain at work. As detailed in Chapter 3, 3.4, several functional magnetic resonance spectroscopy (fMRS) studies have been performed in recent years to characterize the relationship between neuronal activation and energy or neurotransmitter metabolism.

To our knowledge, all previous fMRS studies have focused on neurochemical mechanisms accompanying activation. Because stimulus-induced BOLD increases and decreases reflect different hemodynamic mechanisms, it is conceivable that areas with positive and negative BOLD responses may show distinct metabolic signatures in fMRS experiments. In particular, we hypothesized to observe opposite directions of the [Glu] response in view of previous fMRI work linking the negative BOLD response to decreased neuronal activity and/or inhibition. The human visual cortex was targeted in our investigation because it can be readily stimulated to evoke positive or negative BOLD signals by well-established paradigms.

7.2 Methods

7.2.1 Subjects

Due to relatively long acquisition protocols, investigations of activation and deactivation were performed in separate sessions. In total, 14 healthy volunteers (5 women and 9 men, age range 22-33 years) participated in experiments generating a positive BOLD response, and 12 healthy volunteers (6 women, age range 18-31 years) participated in the experiments generating a negative BOLD response. Eight subjects (3 women, age range 22-31 years) participated in both sessions, that is, they were included both in the activation and the deactivation cohort. All participants had given informed written consent prior to the experiments, which had been approved by the Ethics Committee of the University of Leipzig.

7.2.2 Visual stimulation

The visual stimuli (see Chapter 4, 4.9 Visual stimulation paradigms and BOLD response maps, **Figure 20**) had been extensively tested in previous fMRI

studies of the neurovascular coupling in human brain (Huber et al. 2014). They consisted of a full-field radial 25.5% grey/black flickering checkerboard (8 Hz) to evoke a positive BOLD response and a centered small-circle flickering checkerboard (8 Hz) for a negative BOLD response (**Figure 20**). Results from electrophysiology experiments in macaques indicate that such types of stimuli induce predominantly excitatory activity in areas of activation whereas the net neuronal responses are inhibitory in areas of deactivation (Shmuel et al. 2006). An advantage achieved by using the full-field checkerboard is the possibility to investigate the same cortical region during different paradigms. Both checkerboards included a centered fixation point that was randomly changing color (red – blue – purple – green – yellow) to track the volunteer's attention via pressing a response button. During rest periods, a gray background with a centered fixation cross was presented.

7.2.3 Magnetic resonance acquisitions

All investigations were performed on a MAGNETOM 7 T scanner (Siemens Healthcare, Erlangen, Germany) equipped with a single-channel transmit/32-channel receive radiofrequency (RF) head coil (Nova Medical, Wilmington, MA, USA). By executing a landmark-based pre-scan gradient-recalled echo (GRE) sequence (*'Auto-Align Head'*), geometric information was acquired that was automatically applied to all subsequent protocols. An anatomical reference was obtained with a three-dimensional (3D) *'Magnetization-Prepared 2 RApid Gradient Echoes'* (MP2RAGE) sequence (Marques et al. 2010; Metere et al. 2017) and *'GeneRalized Autocalibrating Partially Parallel Acquisitions'* (GRAPPA) (Griswold et al. 2002) along the first phase-encoding direction (acceleration factor 3). Acquisition parameters included TR = 5 sec; flip angles, FA = 4 and 5°; inversion times, TI = 0.8 and 2.7 sec; echo time, TE = 3.33 ms; field of view (FOV) of 256×256×176 mm^3; nominal resolution 1×1×0.85 mm^3 (acquisition time, TA = 6:42

min). Finally, a block design with alternation of 30 sec of rest and 30 sec of stimulus presentation was performed during two-dimensional (2D) single-shot GRE echo-planar imaging (Mansfield 1977) (EPI; α = 70°; TE = 20 ms; TR = 2 sec; GRAPPA acceleration factor 2; 150 repetitions; TA = 5:08 min) used as a functional localizer (30 slices aligned along the calcarine sulcus; thickness 4 mm; no gap; FOV 192×192 mm^2; nominal resolution 3×3×4 mm^3). BOLD activation maps were obtained with a standard SPM12 (http://www.fil.ion.ucl.ac.uk/spm) processing scheme.

Localization of a single 8ml voxel for fMRS was performed by co-registration of the thresholded BOLD activation/deactivation map to the MP2RAGE volume (**Figure 28**). A *'semi-adiabatic Localization by Adiabatic SElective Refocusing'* (semi-LASER) sequence (Öz and Tkáč 2011; Scheenen et al. 2008) (TE = 40 ms; TR = 4 sec) was used for ^{1}H spectroscopy after adjusting first- and second-order voxel shims with *'Fast Automatic Shimming Technique by Mapping Along Projections'* (FAST(est)MAP) (Gruetter 1993; Gruetter and Tkáč 2000). Two blocks of alternating 5:20 min rest versus 5:20 min stimulation were used as paradigm for fMRS (320 repetitions). To perform water scaling for absolute metabolite quantification, further acquisitions were performed without water suppression (16 repetitions).

One volunteer from the deactivation cohort did not properly respond to the fixation-point color change during the fMRS acquisition and was discarded from the analysis.

7.2.4 MRS data post-processing and metabolite quantitation

Non-averaged, time-domain raw data (Siemens TWIX format) were exported after acquisition and post-processed with single precision using MATLAB (ver. 9.3 R2017b; MathWorks, Natick, MA, USA) routines unless otherwise stated. Each free induction decay (FID; i.e. the descending portion of the spin echo) consisted of a 3D array of complex-valued time points (n_t = 4128) ×

receive channels (n_{ch} = 32) × repetitions (n_{rep} = 320 or 16 for the water-suppressed or water-unsuppressed acquisitions, respectively). Eddy currents corrections, channel coil combination and frequency drift corrections were performed as described on Chapter 4 on the section: 4.8 MRS post-processing.

Water-suppressed single-scan acquisitions were averaged over 16 consecutive repetitions yielding 20 spectra per subject, that is, five spectra acquired during each of the alternating conditions rest and sustained stimulus presentation, subsequently labeled as 'REST1', 'STIM1', 'REST2', and 'STIM2'. Considering the number of included subjects, we obtained a total of 280 spectra acquired during activation runs and 220 spectra acquired during deactivation runs.

Metabolite quantification was performed with LCModel (Provencher 1993) within a chemical shift range between 0.2 and 4.0 ppm. The unsuppressed water signal served as an internal concentration reference assuming a brain water content of 78% (T. Ernst, Kreis, and Ross 1993). We used the same mixed (acquired and simulated) LCModel basis set as used on Chapter 5 and Chapter 6, which preparation is explained on: Chapter 4, 4.7.2 Acquired basis set for semi-LASER.

As (de)activation-related metabolic changes were expected to be rather subtle according to previous fMRS studies, the same step-wise procedure described on the methods of Chapter 5 was applied to identify fits of sufficient quality for inclusion in the final analysis.

In addition, the mean stimulus-related percent BOLD-signal change during the functional localizer was calculated with SPM12 in a volume that was adjusted in size to the spectroscopy voxel for each volunteer and (linearly) correlated with metabolic results from the fMRS experiments. These correlation analyses included *(i)* baseline metabolite levels recorded during REST1 as well as *(ii)* averaged metabolite concentration changes during STIM1+STIM2 in comparison to REST1+REST2.

7.3 Results

Figure 29 shows typical acquisitions in activated and deactivated regions and **Figure 30** their LCModel fits. The mean FWHM was 10.6 ± 2.2 Hz (i.e. 0.036 ± 0.007 ppm). Compared to the linewidth, the difference in chemical shifts of the methylene groups of Cr and PCr (0.017 ppm) was regarded insufficient for a reliable quantification of both metabolites (Tkác et al. 2009), and only the sum of their concentration estimates (total creatine, tCr) was included in the further analysis. Along the same line of reasoning, only the sum of the [GPC] and [PCh] estimates (total choline concentration, [tCh]) was considered reliable. Further metabolites that were fitted with sufficient accuracy included Asp, Glc, Gln, Glu, GSH, mI (which also includes an unspecified contribution from Gly), NAA, and NAAG. A summary of the obtained concentration estimates for the different conditions is provided in **Figure 31** and **Tables Table 7** and **Table 8**.

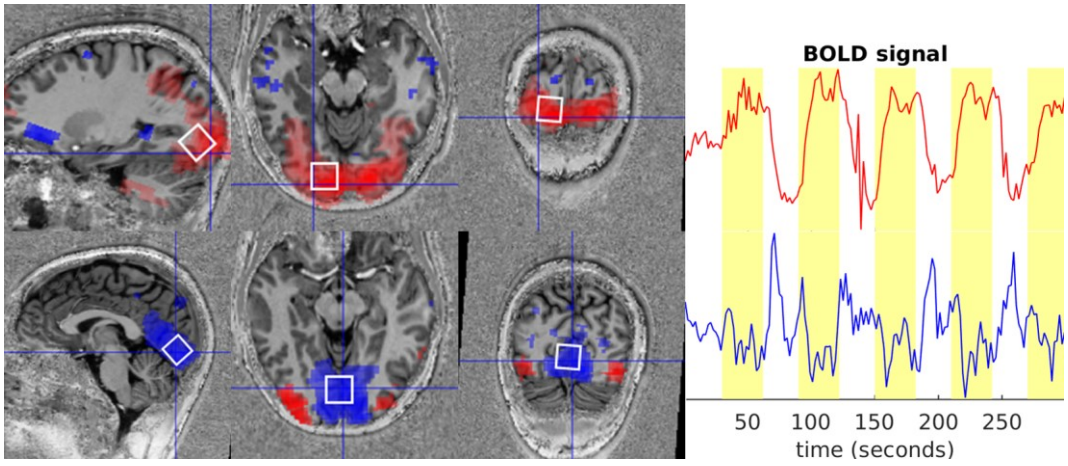

Figure 28: PBR and NBR on visual cortex. LEFT: Overlays of the T1-weighted anatomical images (sagittal, transversal and coronal slices), MRS voxel geometry and PBR and NBR activation maps on a representative volunteer. Activation maps are calculated with SPM12 from the EPI acquisition during a full field checkerboard (top row) and small field checkerboard (bottom row). PBR is shown in red and NBR in blue. White squares indicate the position of the 20x20x20 mm3 MRS voxel. RIGHT: SPM VOI time series extraction of 1st eigenvariate on a 20x20x20 mm3 located at the global maximum, adjusted for effects of interest. Red is the PBR and blue is the NBR. Yellow bars indicate when the stimulus is presented.

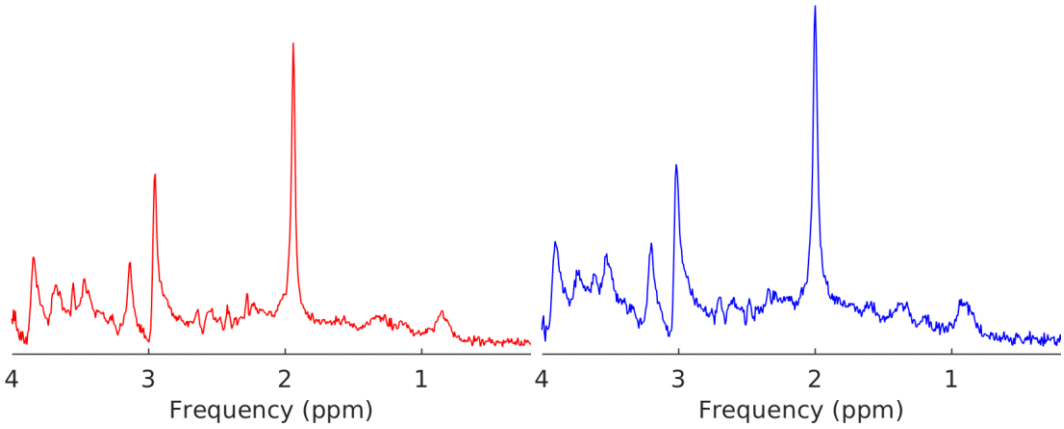

Figure 29: Representative 16-averages spectra acquired during the stimuli full field checkerboard (red) and small checkerboard (blue). 7 T semi-LASER (TE/TR = 40/4000 ms), 8ml voxel on visual cortex.

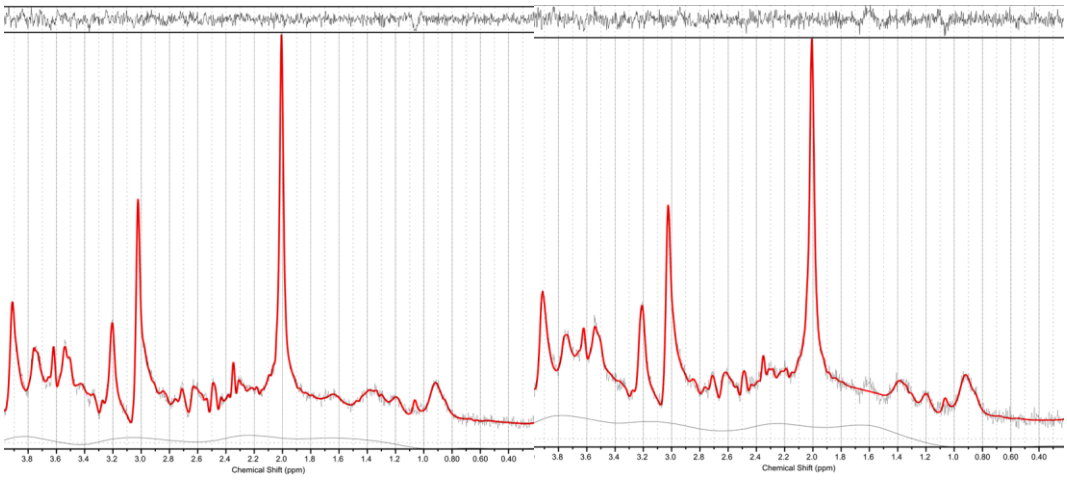

Figure 30: Representative proton spectra (LCModel results) acquired with semi-LASER (TE 40 ms, TR 4 sec, 16 averages) in V1 during stimulation by a full-field flickering checkerboard to produce a positive BOLD response (LEFT) and during stimulation by a small-circle flickering checkerboard (RIGHT) to produce a negative BOLD response.

A statistical evaluation of our main hypothesis revealed a significant *increase* of the average [Glu] by 5.3% (p = 0.007) during full-field stimulation (activation) as compared to the average concentration at baseline (**Figure 32A**). The mean increase was larger for the first than for the second stimulation period (5.7% for STIM1 vs. REST1, p = 0.042 and 5.0% for STIM2 vs. REST2, p = 0.078); however,

this difference was insignificant. The opposite direction of [Glu] changes at a reduced effect size was obtained with the deactivation experiment (**Figure 32B**) yielding a significant average *decrease* (–3.8%, p = 0.017) during stimulation with regards to baseline. Here, the magnitude of the change was smaller during the first (–3.5% for STIM1 vs. REST1, p = 0.16) as compared to the second stimulation period (–4.2% for STIM2 vs. REST2, p = 0.045).

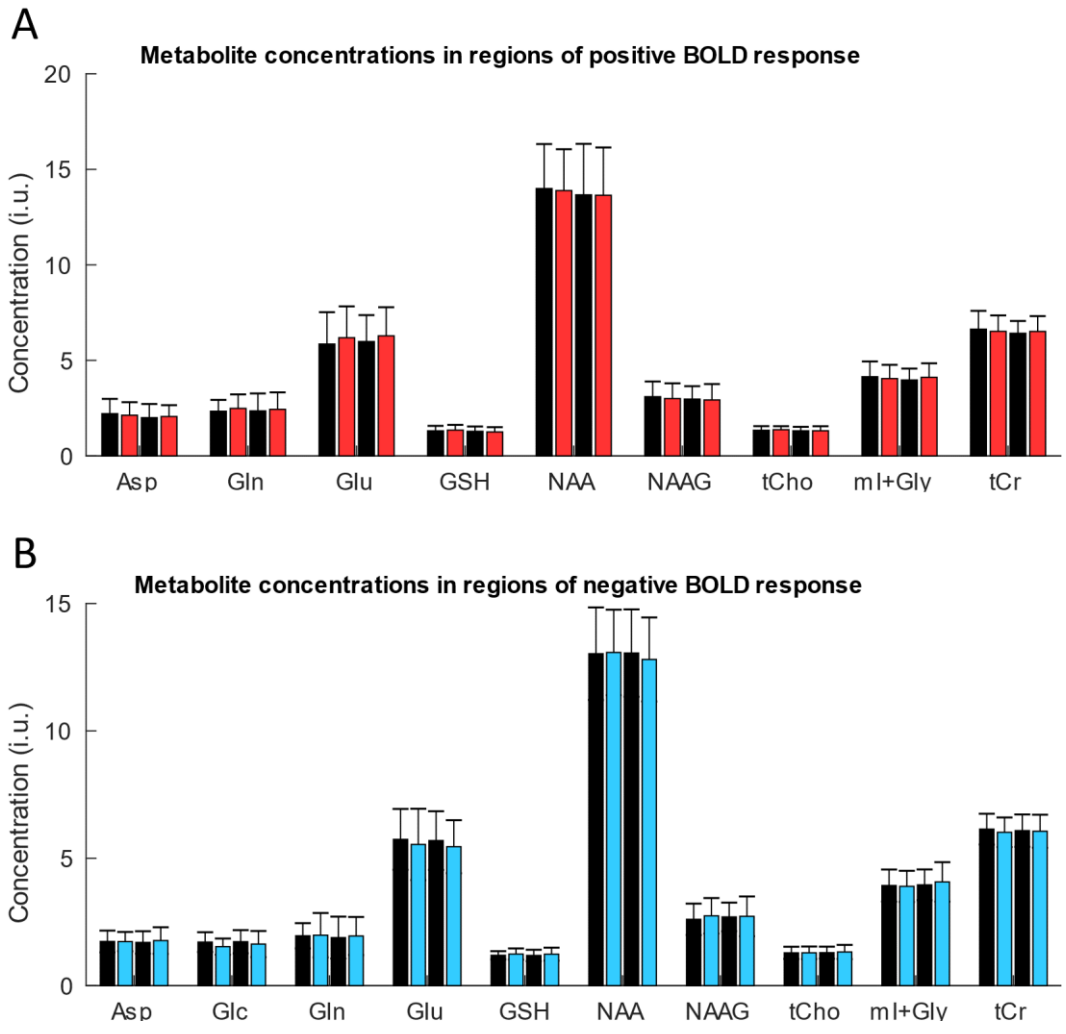

Figure 31: Metabolite concentration during activation and deactivation. The mean metabolite concentrations in 'institutional units' (i.u.) represent the average across subjects obtained in regions of a positive BOLD response upon stimulation by a full-field flickering checkerboard **(A)** and in regions of a negative BOLD response upon stimulation by a small-circle flickering checkerboard **(B)**. Black bars correspond to the REST1 and REST2 periods and colored bars correspond to STIM1 and STIM2 periods. Error bars indicate one standard deviation of the mean values.

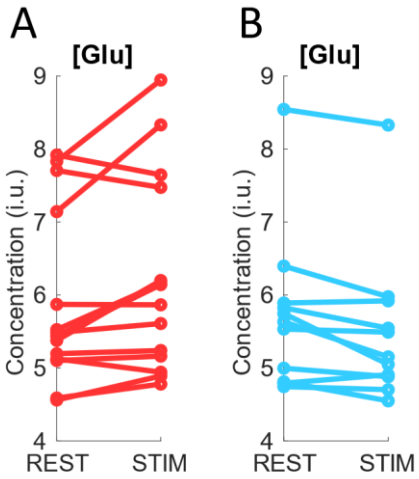

Figure 32: Individual glutamate concentration ([Glu]) changes during activation and deactivation. Concentration changes (institutional units, i.u.) in regions of a positive BOLD response to stimulation by a full-field flickering checkerboard in 14 healthy subjects (A) and in regions of a negative BOLD response to stimulation by a small-circle flickering checkerboard in 11 healthy subjects (B). Line connect the individual mean values of all spectra acquired in an individual subject during REST1+REST2 and the individual mean values of all spectra acquired in the same subject during STIM1+STIM2. Paired t-tests yielded significant changes of 5.3% (p = 0.007) during the positive and of–3.8% (p = 0.017) during the negative BOLD response.

The exploratory analysis of the other metabolite concentrations yielded decreased [Glc] (–7.9%, p = 0.025) as well as increased [GSH] (+4.2%, p = 0.023) in the deactivation experiments. We note that the number of rejected estimates for [Glc] according to our quality-control criteria was too high (58.6%) for a meaningful evaluation of changes during the activation experiments. Changes of [GSH] associated with activation were insignificant (p = 0.95).

Figure 33 summarizes the results from correlation analyses of BOLD signal changes and metabolic parameters. The increases and decreases of [Glu] correlated positively (R = 0.60, p = 0.002) with the percent BOLD signal changes from the combined data of the activation and deactivation experiments (**Figure 33**A) whereas a negative correlation (R = −0.49, p = 0.012) was obtained for [GSH] changes (**Figure 33**B). Additional significant positive correlations of percent BOLD

signal changes were found for the baseline concentrations of Asp (R = 0.44, p = 0.035; **Figure 33**C) and NAAG (R = 0.42, p = 0.035; **Figure 33**D).

metabolite	REST1	STIM1	REST2	STIM2	mean % change	p
Asp	2,21 ± 0,77	2,13 ± 0,68	2,00 ± 0,72	2,06 ± 0,60	-0,57	0,824
Gln	2,34 ± 0,59	2,49 ± 0,73	2,36 ± 0,91	2,44 ± 0,89	4,84	0,267
Glu	5,85 ± 1,67	6,19 ± 1,64	5,99 ± 1,38	6,29 ± 1,50	**5,32**	0,007
GSH	1,31 ± 0,26	1,35 ± 0,27	1,29 ± 0,25	1,26 ± 0,25	-0,15	0,952
NAA	13,99 ± 2,33	13,89 ± 2,16	13,66 ± 2,67	13,64 ± 2,50	-0,44	0,543
NAAG	3,10 ± 0,79	3,00 ± 0,80	2,97 ± 0,68	2,93 ± 0,83	-2,29	0,320
tCh	1,34 ± 0,21	1,37 ± 0,18	1,31 ± 0,21	1,32 ± 0,24	1,18	0,241
mI+Gly	4,14 ± 0,80	4,05 ± 0,72	3,97 ± 0,60	4,11 ± 0,74	0,71	0,598
tCr	6,63 ± 0,96	6,52 ± 0,83	6,42 ± 0,65	6,51 ± 0,80	-0,05	0,959

Table 7: Metabolites' mean concentration during the 4 blocks of the Positive BOLD Response (PBR) fMRS paradigm and mean percentage of concentration change STIM-REST. Significant changes (p < 0.05) are highlighted in bold.

metabolite	REST1	STIM1	REST2	STIM2	mean % change	p
Asp	1,73 ± 0,43	1,73 ± 0,38	1,70 ± 0,44	1,77 ± 0,52	2,00	0,405
Glc	1,71 ± 0,39	1,53 ± 0,32	1,72 ± 0,45	1,63 ± 0,51	**-7,88**	0,025
Gln	1,96 ± 0,50	1,98 ± 0,87	1,89 ± 0,82	1,95 ± 0,75	2,28	0,495
Glu	5,74 ± 1,19	5,54 ± 1,40	5,69 ± 1,15	5,45 ± 1,04	**-3,83**	0,017
GSH	1,19 ± 0,16	1,24 ± 0,22	1,19 ± 0,22	1,24 ± 0,25	**4,16**	0,023
NAA	13,03 ± 1,82	13,08 ± 1,68	13,06 ± 1,71	12,80 ± 1,65	-0,78	0,163
NAAG	2,60 ± 0,62	2,74 ± 0,70	2,70 ± 0,56	2,72 ± 0,78	3,09	0,100
GPC+PCh	1,29 ± 0,24	1,29 ± 0,25	1,29 ± 0,24	1,32 ± 0,28	1,19	0,300
mI+Gly	3,93 ± 0,63	3,90 ± 0,61	3,96 ± 0,60	4,07 ± 0,77	1,07	0,477
Cr+PCr	6,14 ± 0,61	6,02 ± 0,58	6,08 ± 0,64	6,06 ± 0,65	-1,20	0,120

Table 8: Metabolites' mean concentration during the 4 blocks of the Negative BOLD Response (NBR) fMRS paradigm and mean percentage of concentration change STIM-REST. Significant changes (p < 0.05) are highlighted in bold.

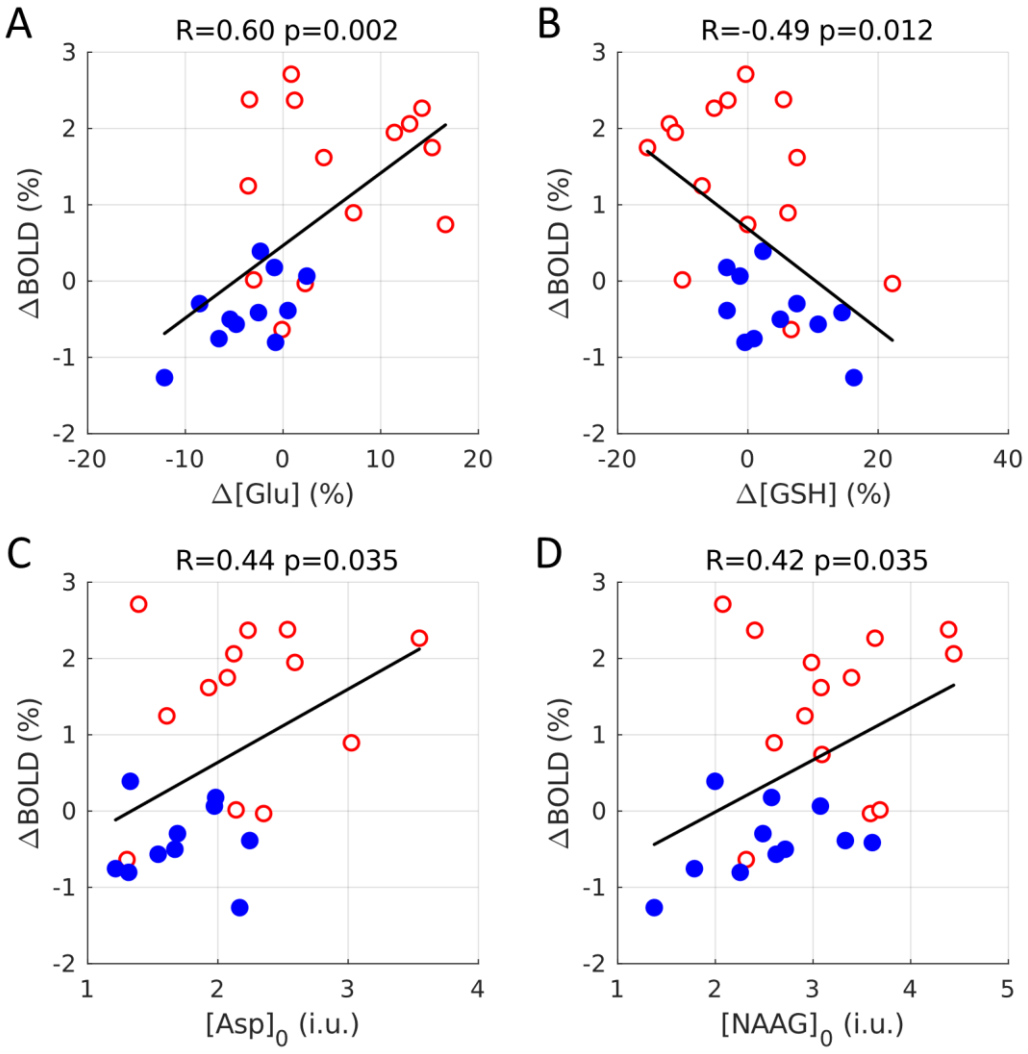

Figure 33: Results from linear correlation analyses (*R*: Pearson correlation coefficient; *p*: error probability) of the percent BOLD signal change, ΔBOLD and metabolic parameters **(A)** percent Glu concentration change, Δ[Glu], **(B)** percent GSH concentration change, Δ[GSH], **(C)** baseline Asp concentration, $[Asp]_0$, (in institutional units, i.u.) and **(D)** baseline NAAG concentration, $[NAAG]_0$, (in i.u.). Each circle corresponds to the result from a single subject. Red empty circles and blue filled circles indicate stimulation experiments producing a positive and a negative BOLD response, respectively. Percent metabolite concentration changes are averaged values (in individual subjects) comparing STIM1+STIM2 and REST1+REST2. The baseline metabolite concentrations refer to averaged results (in individual subjects) measured during REST1 only.

7.4 Discussion

Our observation of a significant mean increase of [Glu] by 5.3% in regions of V1 showing an activation during stimulation with a full-field flickering checkerboard is within the range of 2 to 12% of previously reported fMRS results (Mangia, Tkác, et al. 2007; Y. Lin et al. 2012; Apšvalka et al. 2015; Ip et al. 2017; Schaller et al. 2013). They are also in line with rises by 6 to 8% during activation of rat barrel cortex obtained with ^{14}C labeling (Dienel, Wang, and Cruz 2002) and ^{1}H fMRS (Just et al. 2013), respectively. As mentioned on Chapter 5, besides limitations in the precision of the measurement of relatively small concentration changes, some variability in the results from different studies may be due to differences in the employed stimuli and paradigm design, or differences in MRS acquisitions and post-processing. Varying degrees of partial voluming are further likely contributors to variability both between studies as well as between subjects within the same study.

During activation, CBF and the cerebral metabolic rate of Glc (CMR_{Glc}) increase substantially whereas CMR_{O2} increases only moderately. The resulting mismatch between the amounts of oxygen being supplied by the blood and being consumed by the brain is the physiological reason for the increase of the BOLD signal. While functional hyperemia was initially proposed to be controlled by a negative-feedback loop to fulfill the energy demands during activation (Attwell and Laughlin 2001), there is now evidence of a feedforward mechanism signaled by glutamatergic neurotransmission (Offenhauser et al. 2005; Attwell et al. 2010).

Recent research further suggests that the negative BOLD response occurs in regions where there is a decrease of CBF together with a decrease of CMR_{O2} (Mullinger et al. 2014). As elevated CBF is the result of signaling pathways initiated by increased synaptic [Glu], we may expect a correspondingly reduced [Glu] in regions where CBF is lower during stimulation than during basal conditions. The extrapolation of this prediction for deactivation is, however, not trivial due to the

complex interplay of metabolic and hemodynamic responses leading to the BOLD signal (Lauritzen et al. 2012). Investigations of [Glu] changes during deactivation and their correlation with BOLD signal changes were, hence, the primary goals of the current work. While the activation experiments yielded an increase of [Glu], we observed a mean decrease of –3.8% in deactivated regions upon visual stimulation by a small-circle flickering checkerboard providing further evidence of the neuronal origin of the negative BOLD response.

Besides neurochemical consequences of activation, metabolic compartmentation and MRS 'visibility' are also important for the interpretation of the fMRS responses (Williams 1999; Gruetter 2002). Isotope labeling experiments suggest two Glu pools—a smaller one of less than 10% with relatively rapid turnover assigned to astrocytes and a larger one of slower turnover assigned to neurons (Lukkarinen et al. 1997; Chapa et al. 2000). On the subcellular level, intraterminal Glu is distributed in the cytosol at roughly 10 mM and—at ten-fold higher concentration—sequestered in synaptic vesicles (Maycox, Hell, and Jahn 1990; McMahon and Nicholls 1991; Bergles, Diamond, and Jahr 1999). Baseline concentrations in the extracellular space (ECS) outside synapses are very low, in the order of 3 μM (Barbour and Häusser 1997; Danbolt 2001).

While vesicular [Glu] is particularly high, it is also largely 'invisible' to MRS, presumably due to accelerated T2-relaxation in a tightly packed microenvironment (Kauppinen et al. 1994). This has led to the hypothesis that [Glu] changes observed with fMRS might reflect the transition from the pool of 'invisible' vesicular Glu to 'visible' synaptic, extracellular or astrocytic pools, thereby measuring primarily the process of neurotransmission (Apšvalka et al. 2015). However, this hypothesis cannot be easily brought in line with established data on Glu distribution and metabolic fluxes. For illustration, we consider a volume of cortex (e.g. 1 mm^3) containing 80% cellular structures and 20% ECS (Nicholson and Syková 1998). We further assume that the cellular compartment is evenly distributed between neurons and astroglia (Herculano-Houzel 2014) with

cytosolic baseline [Glu] of 10 mM and 1 mM, respectively (Kanamori, Ross, and Kondrat 2002). Complete exocytotic transmitter release from a vesicle containing 4000 molecules of Glu into the tiny volume of a synaptic cleft (roughly 2×10^{-12} mm^3) would increase intrasynaptic [Glu] by a factor of 1,000 to produce a peak concentration of 3 mM (Bergles, Diamond, and Jahr 1999; Barbour and Häusser 1997; Danbolt 2001). With an average synaptic density around $10^9/mm^3$ in human neocortex (Alonso-Nanclares et al. 2008). the clefts represent 0.2% of the cortical volume (or 1% of the ECS), and even simultaneous release in *all* synapses would change the overall [Glu] in the observed volume element by only 0.14%. However, Glu is not trapped in the cleft but diffuses rapidly (timescale of a few 100 μsec) into the perisynaptic ECS. Mathematical modeling suggests an upper limit of 37 μM for [Glu] in the ECS for simultaneous transmitter release in all synapses (Barbour and Häusser 1997), which would increase the overall [Glu] by 0.15% in agreement with the estimate for the peak cleft concentration. Extracellular variations of [Glu] should, thus, contribute very little to the fMRS results. As low extracellular [Glu] is of critical importance to protect the brain from excitotoxicity, Glu is effectively removed from the ECS by cellular uptake mainly into nearby astrocytes (Bergles, Diamond, and Jahr 1999). Experiments with infusion of ^{13}C-labeled Glc followed by isotope chase with [^{12}C]Glc demonstrate that vesicular Glu retains the label *longer* than the 'metabolic' astroglial and neuronal cytosolic Glu pools (Kanamori, Ross, and Kondrat 2002). Hence, on the timescale of fMRS experiments, released transmitter should not substantially accumulate in the cytosolic compartments as it is effectively recycled to replenish the vesicular pool.

Although these considerations do not capture the complexity of neurotransmitter cycling and metabolism, the estimated orders of magnitude should be realistic. In consequence, the Glu signal observed by MRS primarily results from cytosolic Glu, with a dominant contribution from neurons (as compared to astrocytes), and increases of [Glu] during functional activation do not directly reflect synaptic Glu release but represent adaptations of cerebral Glu

metabolism and production (Mangia, Tkác, et al. 2007; Y. Lin et al. 2012; Schaller et al. 2014; Bednařík et al. 2015; Ip et al. 2017). Elevated [Glu] during neuronal activation indicates an increased tricarboxylic acid (TCA) cycle rate to which Glu is linked via dynamic exchange with α-ketoglutarate (Mangia, Giove, and DiNuzzo 2012). Previously observed opposite changes in [Glu] and [Asp] have been interpreted as an increased flux through the malate-aspartate shuttle (MASh) to maintain the cytosolic redox potential NADH/NAD^+ that is required for oxidative Glc metabolism and neurotransmitter synthesis (Mangia, Tkác, et al. 2007; Y. Lin et al. 2012; Bednařík et al. 2015). These directions of changes in [Glu] and [Asp] were also found in our study both in the activation and (with opposite signs) in the deactivation experiments; however, the [Asp] changes were insignificant as also noted by Schaller et al (Schaller et al. 2014). Increased flux through pyruvate decarboxylase (Schaller et al. 2014) as well as Glu/Gln cycling or GSH synthesis have also been suggested as potential causes of [Glu] elevations (Y. Lin et al. 2012).

Careful investigations of the relationship between the Glu/Gln cycle rate and the rate of Glc oxidation have established that approximately 80% of oxidative Glc consumption is related to signaling at baseline (Hyder et al. 2006; Rothman et al. 2011). As increased [Glu] during sustained activation is regarded as manifestation of an elevated steady state powered mainly by oxidative metabolism, reduced [Glu] observed during deactivation would suggest a TCA cycle rate below baseline. The changes in [Glu] were positively correlated with the percentage positive BOLD response, consistent with results from Bednařík et al. (Bednařík et al. 2015), presumably reflecting enhanced energy production during activation by increases in glycolytic and TCA cycle fluxes. In expansion of these observations, our results indicate that the same positive correlation also exists for the percentage negative BOLD response. Moreover, the entire range of (positive and negative) [Glu] and BOLD signal changes obtained with both stimuli could be fitted to a single regression line (**Figure 33A**). It is to note that within the

experimental accuracy, we did not observe a nonzero intercept in our data, which had been reported by Bednařík et al. (Bednařík et al. 2015).

Whereas the [Glu] changes show a remarkable consistency with the behavior of the BOLD response during activation and deactivation—regarding polarity (positive/negative Δ[Glu] during positive/negative BOLD response; **Figure 32**) and scaling (**Figure 33A**)—[Glc] changes indicate distinct differences between the underlying activities. Previous studies with visual stimuli producing a positive BOLD response yielded reduced [Glc] (Bednařík et al. 2015; Schaller et al. 2013) and increased [Lac] (Mangia, Tkác, et al. 2007; Y. Lin et al. 2012; Mekle et al. 2017; Bednařík et al. 2015; Schaller et al. 2013; Mangia, Tkáč, et al. 2007) reflecting enhanced glycolytic flux and, hence, increased CMR_{Glc}. While we could not reliably quantify [Glc] during activation and [Lac] in both types of experiments, we found a significantly *decreased* [Glc] (indicative of *increased* CMR_{Glc}) along with a negative BOLD signal change (i.e. a presumably inhibitory response), that is, the *same* direction of change as previously observed for a positive (i.e. excitatory) BOLD response.

The inverse relation of enhanced Glc metabolism despite a negative BOLD signal change, indicating a local dissociation of CBF and energy metabolism, does not seem to agree with the 'metabolic hypothesis' that BOLD signal changes are directly linked to local energy needs. Consequently, this supports the assumption that the hemodynamic response is primarily driven by neurotransmitter-related signaling (Logothetis 2008; Lauritzen et al. 2012; Attwell and Iadecola 2002). Consistently, using a combination of optical imaging techniques, two-photon microscopy and autoradiography to study ipsilateral rat somatosensory cortex during unilateral forepaw stimulation, Devor et al. (Devor et al. 2008) observed blood oxygenation and flow *decreases* along with *vasoconstriction* but *increased* 2-deoxyglucose uptake. Boorman et al. (Boorman et al. 2010) found a negative BOLD response resulting from decreased CBV and CBF but increased CMR_{O2} in rat somatosensory cortex, unfortunately, without investigating Glc metabolism.

While it is believed that a positive BOLD response to sensory stimulation reflects excitatory neuronal activity with release of vasodilators, recent evidence suggests a relation of the negative BOLD response to excitation of inhibitory interneurons and release of vasoconstrictors (Lauritzen et al. 2012) In general, the obtained amplitude and sign of the net BOLD signal change result in a context-dependent manner from stimulus-induced modulations of CBF and $CMRO_2$ (Buzsáki, Kaila, and Raichle 2007). As they are (non-linearly) controlled by separate mechanisms (Ca^{2+} rises and ATP turnover, respectively) they cannot be easily predicted from the polarity of the BOLD response (Lauritzen et al. 2012).

While a net activation of GABAergic inhibitory interneurons during a negative BOLD response is a plausible assumption, [Glu] might be still a marker of (oxidative) energy metabolism. There is evidence that GABA does not couple inhibitory neuronal activity with Glc utilization as Glu does for excitatory neurotransmission (Chatton, Pellerin, and Magistretti 2003). However, by activating GABA interneurons, Glu signaling can lead to an overall inhibitory activity in a given cortical area, and Glu release and uptake by astrocytes would stimulate glycolysis in astrocytes. The reduced [Glu] associated with deactivation as observed here would be consistent with a net reduction of excitatory transmission as well as reduced CBF and, hence a negative BOLD response, due to less efficiently triggered vasodilation or indirectly triggered vasoconstriction.

Overall, our finding of concurrently decreased [Glu] and [Glc] during a negative BOLD response could be explained by a net shift towards an enhanced relative contribution from anaerobic metabolism. Considering that the combined changes of [Glu] and [Asp] have been linked to MASh flux, (Mangia, Tkác, et al. 2007) the reversal of [Glu] and [Asp] changes associated with positive in comparison to negative BOLD responses might indicate a reduced MASh flux and, thereby, reduced redox potential during deactivation (McKenna et al. 2006; Bak et al. 2012). Reduced MASh activity due to inhibitor treatment has been shown to impair Glc oxidation (Dienel 2012) In this context, it seems plausible that variations

in baseline [Asp] contribute to the inter-subject variability of the BOLD responses as indicated by their correlation with BOLD signal changes (**Figure 33C**). A similar effect was previously proposed for baseline [GABA] that was found to correlate negatively with the BOLD response (Bednařík et al. 2015; Muthukumaraswamy et al. 2009). Moreover, the scenario seems to apply to baseline [NAAG] which we found to correlate positively with BOLD signal changes (**Figure 33D**). *N*-acetylaspartylglutamate is the third most prevalent neurotransmitter in the central nervous system. Among several functions, it activates presynaptic and glial metabotropic Glu receptor 3 (mGluR3), which reduces Glu release producing a neuroprotective effect (Neale et al. 2011). Moreover, mGluR3 activation triggers astrocyte Ca^{2+} waves inducing vasodilation (Baslow 2008), which is directly linked to the BOLD response (Schulz et al. 2012).

Lin et al. (Y. Lin et al. 2012) reported an activation-induced increase in [GSH] in the visual cortex, which has not yet been corroborated by other fMRS studies. As possible explanations, they discussed the well-established role of GSH in detoxification of reactive oxygen species generated via enhanced electron transport chain activity or the clearance of increased Glu during activation. In our study, we obtained a significant *increase* in [GSH] by 4.2% in the NBR along with *decreased* [Glu] during reduced neuronal activity, which seems paradox in view of the results of Lin et al. However, recent research suggests more actions for GSH besides detoxification or clearance of Glu including a potential role as neuromodulator/neurotransmitter (Janáky et al. 1999; Dringen and Hirrlinger 2003). Inhibition of glutamatergic transmission via GSH has been discussed in the context of sleep regulation (Inoué, Honda, and Komoda 1995) and might provide an explanation of our finding considering the inhibitory nature of neuronal responses in regions with negative BOLD signal changes. The *negative* correlation between the BOLD signal and the [GSH] changes (**Figure 33C**) would be in line with this assumption. However, further research is needed to critically evaluate

different hypotheses about potential [GSH] changes during activation or inhibition.

7.5 Conclusion

The amplitude and direction of stimulus-induced variations in the concentration of Glu correlate with positive and negative BOLD responses in human V1. As suggested by previous studies of brain activation, these alterations probably reflect adaptations of tricarboxylic acid cycle activity. This interpretation may be extrapolated to also include areas of deactivation based on the current results. Surprisingly, a decrease of the concentration of Glc during deactivation, that is, the same direction of change as previously reported for activation, indicated upregulated anaerobic metabolism, which is in line with previous studies employing invasive techniques in rodents. Overall, these observations do not agree well with the 'metabolic hypothesis' of a direct link between Glc utilization and CBF regulation, but support to the so-called 'neurogenic hypothesis' suggesting that the hemodynamic response is mainly driven by feedforward release of vasoactive messengers (Devor et al. 2008). Additional observations include correlations of baseline levels of Asp and NAAG with BOLD signals, possibly contributing to the variability of individual BOLD responses. Changes in GSH concentrations during deactivation might be indicative of a neuromodulatory effect.

Chapter 8

Summary

A good understanding of brain function is today of interest due to the multiple applications in basic and medical sciences. Blood oxygenation level-dependent (BOLD) functional magnetic resonance imaging (fMRI) is the most widely used method for studying human brain activity. However, it does not provide quantitative information on neuronal activation. On the other hand, magnetic resonance spectroscopy (MRS) methodologies are sensitive to different aspects of neuronal activation and provide a complementary tool for investigating the human brain at work. Several functional magnetic resonance spectroscopy (fMRS) studies have been performed in recent years to characterize the relationship between neuronal activation and energy or neurotransmitter metabolism.

Stimulus-induced BOLD signal increases and decreases reflect different hemodynamic mechanisms, and areas with positive and negative BOLD responses may show distinct metabolic signatures in fMRS experiments. The main purpose of this dissertation was to identify and characterize the brain metabolic changes happening during brain activation and deactivation. Since those metabolic changes are expected to be very subtle, a satisfactory quality of the experimental set up needs to be achieved, which depends on a variety of factors, e.g. duration and kind of stimuli, field strength and acquisition protocol used.

A theoretical gain in SNR and resolution is obtained by a simple translation of the experimental acquisition to higher fields, but in order to make those gains effective a set of challenges needs to be solved:

- The standard water suppression scheme employing 3 RF pulses (WET) that incorporates the PRESS sequence at 3 T is insufficient at 7 T due to the broad $\boldsymbol{B}_1$ inhomogeneity (Chapter 4, 4.4 Influence of B1 inhomogeneity on WET water suppression at high field). Numerical simulations showed that at least 5 RF pulses are needed to implement the WET water suppression scheme at 7 T. Lately, the choice of semi-LASER instead of PRESS for the 7 T acquisitions solved the problem by incorporating VAPOR water suppression instead.

- A review of the different shimming techniques to correct $\boldsymbol{B}_0$ inhomogeneities was done (Chapter 4, 4.5 Shimming), in order to select the best strategy for MRS. FASTESTMAP, achieved a very good SNR and linewidth in ca. 2 minutes at 3 T and 7 T. Furthermore, second order interactive shimming by line shape could slightly improve the results at 7 T but requires additional 10 to 15 minutes. Therefore, FASTESTMAP was used in all our experiments.

- The best MRS acquisition sequence at 7 T was investigated (Chapter 4, 4.6 Optimization of single-voxel MRS sequence acquisition parameters at 7T) with the aim of having the shortest TR possible to improve temporal resolution, the shortest TE possible to improve the detection of metabolites of interest, good spectral quality, a well-defined voxel, and reduced Chemical Shift Displacement Artifact

(CSDA). After comparing PRESS, STEAM, LASER and semi-LASER the best performance was given by semi-LASER and STEAM. While STEAM allowed a better water suppression and shorter TE, semi-LASER obtained higher SNR and allowed for shorter TR and was therefore chosen for the rest of the experiments at 7 T.

It is important to use an adequate basis set that includes the profile of the model spectra as close as possible to the acquired data. Therefore, a mixed acquired-simulated basis set was prepared to quantify the semi-LASER spectra (Chapter 4, 4.7.2 Acquired basis set for semi-LASER).

Furthermore, the quality of the acquired spectra was improved by applying the post-processing steps of eddy currents correction, channel coil combination and frequency drift correction (Chapter 4, 4.8 MRS post-processing).

Different visual stimuli (flickering checkerboard and moving stars, **Figure 20**) that produce a Positive BOLD Response (PBR) at different field strength (3 T and 7 T) were tested. And the percentage of concentration change of the metabolites was calculated during SHORT blocks of stimulus paradigms (32 seconds) and LONG blocks of stimulus (5 minutes). An increase of the concentration of glutamate ([Glu]) appeared to be rather consistent independently of stimulus used, durations of the stimulation, and field strength (Chapter 5). However, no significant [Glu] changes were detected with an ultra-SHORT (4 seconds) stimulation paradigm at 7 T (Chapter 6).

The extent of the [Glu] changes detected was higher during the LONG blocks compared to the SHORT blocks, and higher at 7 T compared to 3 T. Additionally, the improved spectral resolution at 7 T allows a better differentiation of glutamate from glutamine. Therefore, we concluded that the best scenario in terms of sensitivity would be to use LONG blocks at 7 T.

The small checkerboard (**Figure 20**) is a visual stimulus that activates the same region of neurons on primary visual cortex (V1) as the full field checkerboard (**Figure 20**) but inducing a negative BOLD Response (NBR). Consequently, LONG blocks paradigms with these two stimuli at 7 T were our choice for the study with fMRS of brain activation and deactivation (Chapter 7).

The metabolic concentration changes observed with fMRS during activation and deactivation (**Figure 31**) were the following:

Compared to baseline, [Glu] increased by 5.3% (p=0.007) during activation and decreased by −3.8% (p=0.017) during deactivation (**Figure 32**). These changes were positively correlated with the amplitude of the BOLD response (R=0.60, p=0.002, **Figure 33**) and probably reflect changes of the tricarboxylic acid cycle activity.

Surprisingly, a decrease of the concentration of glucose ([Glc]) during deactivation (−7.9%, p=0.025), that is, the same direction of change as previously reported for activation, indicated upregulated anaerobic metabolism. This finding is, however, in line with previous studies employing invasive techniques in rodents.

Other findings included an increased concentration of glutathione ([GSH]) (4.2%, p=0.023) during deactivation (possibly indicative of a neuromodulatory effect), a negative correlation of [GSH] and BOLD signal changes (R=−0.49, p=0.012), and positive correlations of aspartate (Asp) (R=0.44, p=0.035) and N-acetylaspartylglutamate (NAAG) (R=0.42, p=0.035) baseline concentrations with the BOLD response (**Figure 33**).

Taken together, the observed effects on glutamate and glucose levels do not agree well with the assumption of a direct link between glucose utilization and regulation of blood flow but give further support to previous hypothesis suggesting that the hemodynamic response is mainly driven by feedforward release of vasoactive messengers.

References

Allison, J. D., K. J. Meador, D. W. Loring, R. E. Figueroa, and J. C. Wright. 2000. "Functional MRI Cerebral Activation and Deactivation during Finger Movement." *Neurology* 54 (1): 135–135. doi:10.1212/WNL.54.1.135.

Alonso-Nanclares, L, J Gonzalez-Soriano, J R Rodriguez, and J DeFelipe. 2008. "Gender Differences in Human Cortical Synaptic Density." *Proceedings of the National Academy of Sciences of the United States of America* 105 (38). National Academy of Sciences: 14615–19. doi:10.1073/pnas.0803652105.

Apšvalka, Dace, Andrew Gadie, Matthew Clemence, and Paul G. Mullins. 2015. "Event-Related Dynamics of Glutamate and BOLD Effects Measured Using Functional Magnetic Resonance Spectroscopy (fMRS) at 3 T in a Repetition Suppression Paradigm." *NeuroImage* 118 (September): 292–300. doi:10.1016/j.neuroimage.2015.06.015.

Araque, A, V Parpura, R P Sanzgiri, P G Haydon, Alfonso Araque, Vladimir Parpura, Rita P. Sanzgiri, and Philip G. Haydon. 1999. "Tripartite Synapses: Glia, the Unacknowledged Partner." *Trends in Neurosciences* 22 (5). Oxford University Press: 208–15. doi:10.1016/S0166-2236(98)01349-6.

Araque, Alfonso, Giorgio Carmignoto, Philip G. Haydon, Stéphane H.R. Oliet, Richard Robitaille, and Andrea Volterra. 2014. "Gliotransmitters Travel in Time and Space." *Neuron* 81 (4): 728–39. doi:10.1016/j.neuron.2014.02.007.

Attwell, David, Alastair M. Buchan, Serge Charpak, Martin Lauritzen, Brian A. MacVicar, and Eric A. Newman. 2010. "Glial and Neuronal Control of Brain Blood Flow." *Nature* 468 (7321). Nature Publishing Group: 232–43. doi:10.1038/nature09613.Glial.

Attwell, David, and Costantino Iadecola. 2002. "The Neural Basis of Functional Brain Imaging Signals." *Trends in Neurosciences* 25 (12). Elsevier: 621–25. doi:10.1016/S0166-2236(02)02264-6.

Attwell, David, and Simon B. Laughlin. 2001. "An Energy Budget for Signaling in the Grey Matter of the Brain." *Journal of Cerebral Blood Flow & Metabolism* 21 (10): 1133–45. doi:10.1097/00004647-200110000-00001.

Bak, Lasse K., Linea F. Obel, Anne B. Walls, Arne Schousboe, Sevan A.A. Faek, Farah S. Jajo, and Helle S. Waagepetersen. 2012. "Novel Model of Neuronal Bioenergetics: Postsynaptic Utilization of Glucose but Not Lactate Correlates Positively with Ca^{2+} Signalling in Cultured Mouse Glutamatergic Neurons." *ASN Neuro* 4 (3): AN20120004. doi:10.1042/AN20120004.

Barbour, B, and M Häusser. 1997. "Intersynaptic Diffusion of Neurotransmitter." *Trends in*

Neurosciences 20 (9). Elsevier: 377–84. doi:10.1016/S0166-2236(96)20050-5.

Baslow, M.H. 2008. "The Astrocyte Surface NAAG Receptor and NAAG Peptidase Signaling Complex as a Therapeutic Target." *Drug News & Perspectives* 21 (5): 251. doi:10.1358/dnp.2008.21.5.1216215.

Bednařík, Petr, Ivan Tkáč, Federico Giove, Mauro Dinuzzo, Dinesh K Deelchand, Uzay E Emir, Lynn E Eberly, and Silvia Mangia. 2015. "Neurochemical and BOLD Responses during Neuronal Activation Measured in the Human Visual Cortex at 7 Tesla." *Journal of Cerebral Blood Flow & Metabolism* 35 (10): 601–10. doi:10.1038/jcbfm.2014.233.

Behm, D. J., A. Ogbonna, C. Wu, C. L. Burns-Kurtis, and S. A. Douglas. 2009. "Epoxyeicosatrienoic Acids Function as Selective, Endogenous Antagonists of Native Thromboxane Receptors: Identification of a Novel Mechanism of Vasodilation." *Journal of Pharmacology and Experimental Therapeutics* 328 (1): 231–39. doi:10.1124/jpet.108.145102.

Bélanger, Mireille, Igor Allaman, and Pierre J. Magistretti. 2011. "Brain Energy Metabolism: Focus on Astrocyte-Neuron Metabolic Cooperation." *Cell Metabolism* 14 (6): 724–38. doi:10.1016/j.cmet.2011.08.016.

Bergles, Dwight E, Jeffrey S Diamond, and Craig E Jahr. 1999. "Clearance of Glutamate inside the Synapse and beyond." *Current Opinion in Neurobiology* 9 (3). Elsevier Current Trends: 293–98. doi:10.1016/S0959-4388(99)80043-9.

Blanco, Víctor M, Javier E Stern, and Jessica A Filosa. 2008. "Tone-Dependent Vascular Responses to Astrocyte-Derived Signals." *American Journal of Physiology. Heart and Circulatory Physiology* 294 (6). American Physiological Society: H2855-63. doi:10.1152/ajpheart.91451.2007.

Bloch, F., W. W. Hansen, and Martin Packard. 1946. "Nuclear Induction." *Physical Review* 69 (3–4). American Physical Society: 127–127. doi:10.1103/PhysRev.69.127.

Boorman, L., A. J. Kennerley, D. Johnston, M. Jones, Y. Zheng, P. Redgrave, and J. Berwick. 2010. "Negative Blood Oxygen Level Dependence in the Rat:A Model for Investigating the Role of Suppression in Neurovascular Coupling." *Journal of Neuroscience* 30 (12): 4285–94. doi:10.1523/JNEUROSCI.6063-09.2010.

Bottomley, P a. 1987. "Spatial Localization in NMR Spectroscopy in Vivo." *Annals of the New York Academy of Sciences* 508 (January): 333–48.

Bressler, David, Nicole Spotswood, David Whitney, A Ishai, and JL Schouten. 2007. "Negative BOLD fMRI Response in the Visual Cortex Carries Precise Stimulus-Specific Information." Edited by Paul Zak. *PLoS ONE* 2 (5). Sinauer Associates: e410. doi:10.1371/journal.pone.0000410.

Brown, Mark A. 2004. "Time-Domain Combination of MR Spectroscopy Data Acquired Using Phased-Array Coils." *Magnetic Resonance in Medicine* 52 (5). Wiley Subscription Services, Inc.,

A Wiley Company: 1207–13. doi:10.1002/mrm.20244.

Busija, David W, Ferenc Bari, Ferenc Domoki, and Thomas Louis. 2007. "Mechanisms Involved in the Cerebrovascular Dilator Effects of N-Methyl-D-Aspartate in Cerebral Cortex." *Brain Research Reviews* 56 (1). NIH Public Access: 89–100. doi:10.1016/j.brainresrev.2007.05.011.

Buxton, Richard B., Kâmil Uludağ, David J. Dubowitz, and Thomas T. Liu. 2004. "Modeling the Hemodynamic Response to Brain Activation." *NeuroImage* 23 (January): S220–33. doi:10.1016/j.neuroimage.2004.07.013.

Buzsáki, György, Kai Kaila, and Marcus Raichle. 2007. "Inhibition and Brain Work." *Neuron* 56 (5). Elsevier: 771–83. doi:10.1016/j.neuron.2007.11.008.

Campbell, W B, D Gebremedhin, P F Pratt, and D R Harder. 1996. "Identification of Epoxyeicosatrienoic Acids as Endothelium-Derived Hyperpolarizing Factors." *Circulation Research* 78 (3): 415–23. http://www.ncbi.nlm.nih.gov/pubmed/8593700.

Cauli, B., Xin-Kang Tong, Armelle Rancillac, Nella Serluca, Bertrand Lambolez, Jean Rossier, and Edith Hamel. 2004. "Cortical GABA Interneurons in Neurovascular Coupling: Relays for Subcortical Vasoactive Pathways." *Journal of Neuroscience* 24 (41): 8940–49. doi:10.1523/JNEUROSCI.3065-04.2004.

Chapa, Francisco, Fátima Cruz, María L. García-Martín, María A. García-Espinosa, and Sebastián Cerdán. 2000. "Metabolism of (1-13C) Glucose and (2-13C, 2-2H3) Acetate in the Neuronal and Glial Compartments of the Adult Rat Brain as Detected by {13C, 2H} NMR Spectroscopy." *Neurochemistry International* 37 (2–3). Pergamon: 217–28. doi:10.1016/S0197-0186(00)00025-5.

Chatton, J Y, L Pellerin, and P J Magistretti. 2003. "GABA Uptake into Astrocytes Is Not Associated with Significant Metabolic Cost: Implications for Brain Imaging of Inhibitory Transmission." *Proc Natl Acad Sci U S A* 100 (21): 12456–61. doi:10.1073/pnas.2132096100.

Chen, Chen, Hilmar P Sigurdsson, Sophia E Pépés, Dorothee P Auer, Penny A Gowland, Paul S Morgan, and Stephen R Jackson. 2017. "Activation Induced Changes in GABA: Functional MRS at 7T with MEGA-SLASER." In *ISMRM 25th Annual Meeting*.

Chmurny, Gwendolyn N., and David I. Hoult. 1990. "The Ancient and Honourable Art of Shimming." *Concepts in Magnetic Resonance* 2 (3). John Wiley & Sons, Inc.: 131–49. doi:10.1002/cmr.1820020303.

Chuquet, J., L. Hollender, and E. A. Nimchinsky. 2007. "High-Resolution In Vivo Imaging of the Neurovascular Unit during Spreading Depression." *Journal of Neuroscience* 27 (15): 4036–44. doi:10.1523/JNEUROSCI.0721-07.2007.

Collins, Christopher M, Bei Yang, Qing X Yang, and Michael B Smith. 2002. "Numerical Calculations of the Static Magnetic Field in Three-Dimensional Multi-Tissue Models of the

Human Head." *Magnetic Resonance Imaging* 20 (5): 413–24. http://www.ncbi.nlm.nih.gov/pubmed/12206867.

Danbolt, Niels C. 2001. "Glutamate Uptake." *Progress in Neurobiology* 65 (1). Pergamon: 1–105. doi:10.1016/S0301-0082(00)00067-8.

Davis, Richard J, Colin E Murdoch, Mozam Ali, Stuart Purbrick, Rivka Ravid, Gordon S Baxter, Nick Tilford, Robert L G Sheldrick, Kenneth L Clark, and Robert A Coleman. 2004. "EP4 Prostanoid Receptor-Mediated Vasodilatation of Human Middle Cerebral Arteries." *British Journal of Pharmacology* 141 (4). Wiley-Blackwell: 580–85. doi:10.1038/sj.bjp.0705645.

De Graaf, R A. 2007. *In Vivo NMR Spectroscopy - 2nd Edition, Principles and Techniques*. *Endeavour*. Vol. 5. doi:10.1016/0160-9327(81)90158-7.

Devor, Anna, Elizabeth M C Hillman, Peifang Tian, Christian Waeber, Ivan C Teng, Lana Ruvinskaya, Mark H Shalinsky, et al. 2008. "Stimulus-Induced Changes in Blood Flow and 2-Deoxyglucose Uptake Dissociate in Ipsilateral Somatosensory Cortex." *The Journal of Neuroscience : The Official Journal of the Society for Neuroscience* 28 (53). Society for Neuroscience: 14347–57. doi:10.1523/JNEUROSCI.4307-08.2008.

Di Salle, F., E. Formisano, D. E J Linden, R. Goebel, S. Bonavita, A. Pepino, F. Smaltino, and G. Tedeschi. 1999. "Exploring Brain Function with Magnetic Resonance Imaging." *European Journal of Radiology* 30 (2): 84–94. doi:10.1016/S0720-048X(99)00047-9.

Dienel, Gerald A. 2012. "Fueling and Imaging Brain Activation." *ASN Neuro* 4 (5). SAGE PublicationsSage CA: Los Angeles, CA: AN20120021. doi:10.1042/AN20120021.

Dienel, Gerald A. 2017. "Lack of Appropriate Stoichiometry: Strong Evidence against an Energetically Important Astrocyte-Neuron Lactate Shuttle in Brain." *Journal of Neuroscience Research* 0 (November 2016). doi:10.1002/jnr.24015.

Dienel, Gerald A., and Nancy F. Cruz. 2004. "Nutrition during Brain Activation: Does Cell-to-Cell Lactate Shuttling Contribute Significantly to Sweet and Sour Food for Thought?" *Neurochemistry International* 45 (2–3): 321–51. doi:10.1016/j.neuint.2003.10.011.

———. 2016. "Aerobic Glycolysis during Brain Activation: Adrenergic Regulation and Influence of Norepinephrine on Astrocytic Metabolism." *Journal of Neurochemistry* 138 (1): 14–52. doi:10.1111/jnc.13630.

Dienel, Gerald A., Robert Y. Wang, and Nancy F. Cruz. 2002. "Generalized Sensory Stimulation of Conscious Rats Increases Labeling of Oxidative Pathways of Glucose Metabolism When the Brain Glucose–Oxygen Uptake Ratio Rises." *Journal of Cerebral Blood Flow & Metabolism* 22 (12). SAGE PublicationsSage UK: London, England: 1490–1502. doi:10.1097/01.WCB.0000034363.37277.89.

DiNuzzo, Mauro, Silvia Mangia, Bruno Maraviglia, and Federico Giove. 2010. "Changes in Glucose

Uptake Rather than Lactate Shuttle Take Center Stage in Subserving Neuroenergetics: Evidence from Mathematical Modeling." *Journal of Cerebral Blood Flow & Metabolism* 30 (3): 586–602. doi:10.1038/jcbfm.2009.232.

Donahue, Manus J., Jamie Near, Jakob U. Blicher, and Peter Jezzard. 2010. "Baseline GABA Concentration and fMRI Response." *NeuroImage* 53 (2): 392–98. doi:10.1016/j.neuroimage.2010.07.017.

Donders, Frans Cornelis. 1851. "Die Bewegungen Des Gehirns Und Die Veränderungen Der Gefässfüllung Der Pia Mater." *Schmid's Fahrbucher* 69: 16–20.

Dringen, R., and J. Hirrlinger. 2003. "Glutathione Pathways in the Brain." *Biological Chemistry* 384 (4): 505–16. doi:10.1515/BC.2003.059.

Ernst, Richard R. 1968. "Measurement and Control of Magnetic Field Homogeneity." *Review of Scientific Instruments* 39 (7). American Institute of Physics: 998–1012. doi:10.1063/1.1683586.

Ernst, T., R. Kreis, and B.D. Ross. 1993. "Absolute Quantitation of Water and Metabolites in the Human Brain. I. Compartments and Water." *Journal of Magnetic Resonance, Series B* 102 (1). Academic Press: 1–8. doi:10.1006/JMRB.1993.1055.

Faro, Scott H., and Feroze B. Mohamed. 2007. *Functional MRI : Basic Principles and Clinical Applications*. Springer.

Fernandez-Klett, F., N. Offenhauser, U. Dirnagl, J. Priller, and U. Lindauer. 2010. "Pericytes in Capillaries Are Contractile in Vivo, but Arterioles Mediate Functional Hyperemia in the Mouse Brain." *Proceedings of the National Academy of Sciences* 107 (51): 22290–95. doi:10.1073/pnas.1011321108.

Filosa, J. A., H. W. Morrison, J. A. Iddings, W. Du, and K. J. Kim. 2016. "Beyond Neurovascular Coupling, Role of Astrocytes in the Regulation of Vascular Tone." *Neuroscience* 323: 96–109. doi:10.1016/j.neuroscience.2015.03.064.

Filosa, Jessica A, Adrian D Bonev, Stephen V Straub, Andrea L Meredith, M Keith Wilkerson, Richard W Aldrich, and Mark T Nelson. 2006. "Local Potassium Signaling Couples Neuronal Activity to Vasodilation in the Brain." *Nature Neuroscience* 9 (11). Nature Publishing Group: 1397–1403. doi:10.1038/nn1779.

Frahm, J., H. Bruhn, M. L. Gyngell, K. D. Merboldt, W. Hänicke, and R. Sauter. 1989. "Localized High-Resolution Proton NMR Spectroscopy Using Stimulated Echoes: Initial Applications to Human Brainin Vivo." *Magnetic Resonance in Medicine* 9 (1). Wiley Subscription Services, Inc., A Wiley Company: 79–93. doi:10.1002/mrm.1910090110.

Frahm, J., T. Michaelis, K. D. Merboldt, H. Bruhn, M. L. Gyngell, and W. Hänicke. 1990. "Improvements in Localized Proton NMR Spectroscopy of Human Brain. Water Suppression, Short Echo Times, and 1 Ml Resolution." *Journal of Magnetic Resonance (1969)* 90 (3): 464–73.

doi:10.1016/0022-2364(90)90051-A.

Garwood, Michael, and Lance DelaBarre. 2001. "The Return of the Frequency Sweep: Designing Adiabatic Pulses for Contemporary NMR." *Journal of Magnetic Resonance* 153 (2): 155–77. doi:10.1006/jmre.2001.2340.

Giapitzakis, Ioannis-Angelos, Tingting Shao, Nikolai Avdievich, Ralf Mekle, Roland Kreis, and Anke Henning. 2018. "Metabolite-Cycled STEAM and Semi-LASER Localization for MR Spectroscopy of the Human Brain at 9.4T." *Magnetic Resonance in Medicine* 79 (4). Wiley-Blackwell: 1841–50. doi:10.1002/mrm.26873.

Girouard, Helene, and Costantino Iadecola. 2006. "Neurovascular Coupling in the Normal Brain and in Hypertension, Stroke, and Alzheimer Disease." *Journal of Applied Physiology (Bethesda, Md. : 1985)* 100 (1): 328–35. doi:10.1152/japplphysiol.00966.2005.

Goense, Jozien, Hellmut Merkle, and Nikos K Logothetis. 2012. "High-Resolution fMRI Reveals Laminar Differences in Neurovascular Coupling between Positive and Negative BOLD Responses." *Neuron* 76 (3). Elsevier: 629–39. doi:10.1016/j.neuron.2012.09.019.

Golay, Marcel J. E. 1958. "Field Homogenizing Coils for Nuclear Spin Resonance Instrumentation." *Review of Scientific Instruments* 29 (4). American Institute of Physics: 313–15. doi:10.1063/1.1716184.

Goldman, M. (Maurice). 1988. *Quantum Description of High-Resolution NMR in Liquids*. Clarendon Press.

Golgi, Camillo. 1903. "Opera." *Omnia* 2: 460.

Gordon, Grant R. J., Hyun B. Choi, Ravi L. Rungta, Graham C. R. Ellis-Davies, and Brian A. MacVicar. 2008. "Brain Metabolism Dictates the Polarity of Astrocyte Control over Arterioles." *Nature* 456 (7223): 745–49. doi:10.1038/nature07525.

Govindaraju, Varanavasi, Karl Young, and Andrew A. Maudsley. 2000. "Proton NMR Chemical Shifts and Coupling Constants for Brain Metabolites." *NMR in Biomedicine* 13 (3): 129–53. doi:10.1002/1099-1492(200005)13:3<129::AID-NBM619>3.0.CO;2-V.

Griswold, Mark A., Peter M. Jakob, Robin M. Heidemann, Mathias Nittka, Vladimir Jellus, Jianmin Wang, Berthold Kiefer, and Axel Haase. 2002. "Generalized Autocalibrating Partially Parallel Acquisitions (GRAPPA)." *Magnetic Resonance in Medicine* 47 (6). Wiley-Blackwell: 1202–10. doi:10.1002/mrm.10171.

Gruetter, Rolf. 1993. "Automatic, Localized in Vivo Adjustment of All First-and Second-order Shim Coils." *Magnetic Resonance in Medicine*, no. 13: 804–11.

———. 2002. "In Vivo 13C NMR Studies of Compartmentalized Cerebral Carbohydrate Metabolism." *Neurochemistry International* 41 (2–3). Pergamon: 143–54. doi:10.1016/S0197-0186(02)00034-7.

Gruetter, Rolf, and Ivan Tkáč. 2000. "Field Mapping without Reference Scan Using Asymmetric Echo-Planar Techniques." *Magnetic Resonance in Medicine* 43 (2): 319–23. doi:10.1002/(SICI)1522-2594(200002)43:2<319::AID-MRM22>3.0.CO;2-1.

Guidi, Maria, Laurentius Huber, Leonie Lampe, Claudine J. Gauthier, and Harald E. Möller. 2016. "Lamina-Dependent Calibrated BOLD Response in Human Primary Motor Cortex." *NeuroImage* 141 (June). Elsevier B.V.: 250–61. doi:10.1016/j.neuroimage.2016.06.030.

Haase, a, J Frahm, W Hänicke, and D Matthaei. 1985. "1H NMR Chemical Shift Selective (CHESS) Imaging." *Physics in Medicine and Biology* 30 (4): 341–44.

Halassa, Michael M., Tommaso Fellin, and Philip G. Haydon. 2009. "Tripartite Synapses: Roles for Astrocytic Purines in the Control of Synaptic Physiology and Behavior." *Neuropharmacology* 57 (4): 343–46. doi:10.1016/j.neuropharm.2009.06.031.

Hall, Catherine N, Clare Reynell, Bodil Gesslein, Nicola B Hamilton, Anusha Mishra, Brad A Sutherland, Fergus M O'Farrell, Alastair M Buchan, Martin Lauritzen, and David Attwell. 2014. "Capillary Pericytes Regulate Cerebral Blood Flow in Health and Disease." *Nature* 508 (7494). Europe PMC Funders: 55–60. doi:10.1038/nature13165.

Hamzei, Farsin, Christian Dettmers, Reinhard Rzanny, Joachim Liepert, Christian Büchel, and Cornelius Weiller. 2002. "Reduction of Excitability ('Inhibition') in the Ipsilateral Primary Motor Cortex Is Mirrored by fMRI Signal Decreases." *NeuroImage* 17 (1): 490–96. doi:10.1006/nimg.2002.1077.

Harel, Noam, Sang-Pil Lee, Tsukasa Nagaoka, Dae-Shik Kim, and Seong-Gi Kim. 2002. "Origin of Negative Blood Oxygenation Level—Dependent fMRI Signals." *Journal of Cerebral Blood Flow & Metabolism* 22 (8): 908–17. doi:10.1097/00004647-200208000-00002.

Helms, Gunther, and Andreas Piringer. 2001. "Restoration of Motion-Related Signal Loss and Line-Shape Deterioration of Proton MR Spectra Using the Residual Water as Intrinsic Reference." *Magnetic Resonance in Medicine* 46 (2). Wiley-Blackwell: 395–400. doi:10.1002/mrm.1203.

Herculano-Houzel, Suzana. 2014. "The Glia/neuron Ratio: How It Varies Uniformly across Brain Structures and Species and What That Means for Brain Physiology and Evolution." *Glia* 62 (9). Wiley-Blackwell: 1377–91. doi:10.1002/glia.22683.

Hertz, Leif, Marie E. Gibbs, and Gerald A. Dienel. 2014. "Fluxes of Lactate Into, From, and among Gap Junction-Coupled Astrocytes and Their Interaction with Noradrenaline." *Frontiers in Neuroscience* 8 (September): 261. doi:10.3389/fnins.2014.00261.

Hillman, Elizabeth M.C. 2014. "Coupling Mechanism and Significance of the BOLD Signal: A Status Report." *Annual Review of Neuroscience* 37 (1): 161–81. doi:10.1146/annurev-neuro-071013-014111.

Hlushchuk, Yevhen, and Riitta Hari. 2006. "Transient Suppression of Ipsilateral Primary

Somatosensory Cortex during Tactile Finger Stimulation." *Journal of Neuroscience* 26 (21): 5819–24. doi:10.1523/JNEUROSCI.5536-05.2006.

Huber, Laurentius, Jozien Goense, Aneurin J. Kennerley, Dimo Ivanov, Steffen N. Krieger, Jöran Lepsien, Robert Trampel, Robert Turner, and Harald E. Möller. 2014. "Investigation of the Neurovascular Coupling in Positive and Negative BOLD Responses in Human Brain at 7T." *NeuroImage* 97 (August): 349–62. doi:10.1016/j.neuroimage.2014.04.022.

Huber, Laurentius, Kâmil Uludağ, and Harald E. Möller. 2017. "Non-BOLD Contrast for Laminar fMRI in Humans: CBF, CBV, and CMRO2." *NeuroImage*, July 20. doi:10.1016/j.neuroimage.2017.07.041.

Huk, Alexander C., Robert F. Dougherty, and David J. Heeger. 2002. "Retinotopy and Functional Subdivision of Human Areas MT and MST." *J. Neurosci.* 22 (16): 7195–7205.

Hyder, Fahmeed, Anant B Patel, Albert Gjedde, Douglas L Rothman, Kevin L Behar, and Robert G Shulman. 2006. "Neuronal–glial Glucose Oxidation and glutamatergic–GABAergic Function." *Journal of Cerebral Blood Flow & Metabolism* 26: 865–77. doi:10.1038/sj.jcbfm.9600263.

Iadecola, Costantino, and Maiken Nedergaard. 2007. "Glial Regulation of the Cerebral Microvasculature." *Nature Neuroscience* 10 (11): 1369–76. doi:10.1038/nn2003.

Inoué, Shojiro, Kazuki Honda, and Yasuo Komoda. 1995. "Sleep as Neuronal Detoxification and Restitution." *Behavioural Brain Research* 69 (1–2). Elsevier: 91–96. doi:10.1016/0166-4328(95)00014-K.

Ip, I.Betina, Adam Berrington, Aaron T. Hess, Andrew J. Parker, Uzay E. Emir, and Holly Bridge. 2017. "Combined fMRI-MRS Acquires Simultaneous Glutamate and BOLD-fMRI Signals in the Human Brain." *NeuroImage*. Elsevier. doi:10.1016/j.neuroimage.2017.04.030.

Janáky, R, K Ogita, B A Pasqualotto, J S Bains, S S Oja, Y Yoneda, and C A Shaw. 1999. "Glutathione and Signal Transduction in the Mammalian CNS." *Journal of Neurochemistry* 73 (3): 889–902. http://www.ncbi.nlm.nih.gov/pubmed/10461878.

Just, Nathalie, Lijing Xin, Hanne Frenkel, and Rolf Gruetter. 2013. "Characterization of Sustained BOLD Activation in the Rat Barrel Cortex and Neurochemical Consequences." *NeuroImage* 74 (July): 343–51. doi:10.1016/j.neuroimage.2013.02.042.

Kanamori, Keiko, Brian D Ross, and Richard W Kondrat. 2002. "Glial Uptake of Neurotransmitter Glutamate from the Extracellular Fluid Studied in Vivo by Microdialysis and 13 C NMR." *J. Neurochem* 83: 682–95. https://onlinelibrary.wiley.com/doi/pdf/10.1046/j.1471-4159.2002.01161.x.

Kastrup, Andreas, Jürgen Baudewig, Sonja Schnaudigel, Ralph Huonker, Lars Becker, Jan Martin Sohns, Peter Dechent, Carsten Klingner, and Otto W. Witte. 2008. "Behavioral Correlates of Negative BOLD Signal Changes in the Primary Somatosensory Cortex." *NeuroImage* 41 (4):

1364–71. doi:10.1016/j.neuroimage.2008.03.049.

Kauppinen, R A, T R Pirttilä, S O Auriola, and S R Williams. 1994. "Compartmentation of Cerebral Glutamate in Situ as Detected by 1H/13C N.m.r." *The Biochemical Journal* 298 (Pt 1) (1). Portland Press Limited: 121–27. doi:10.1042/BJ2980121.

Klingner, Carsten M., Kerstin Ebenau, Caroline Hasler, Stefan Brodoehl, Yvonne Görlich, and Otto W. Witte. 2011. "Influences of Negative BOLD Responses on Positive BOLD Responses." *NeuroImage* 55 (4): 1709–15. doi:10.1016/j.neuroimage.2011.01.028.

Klingner, Carsten M., Caroline Hasler, Stefan Brodoehl, and Otto W. Witte. 2010. "Dependence of the Negative BOLD Response on Somatosensory Stimulus Intensity." *NeuroImage* 53 (1): 189–95. doi:10.1016/j.neuroimage.2010.05.087.

Klingner, Carsten M., Ralph Huonker, Sandra Flemming, Caroline Hasler, Stefan Brodoehl, Christoph Preul, Hartmut Burmeister, Andreas Kastrup, and Otto W. Witte. 2011. "Functional Deactivations: Multiple Ipsilateral Brain Areas Engaged in the Processing of Somatosensory Information." *Human Brain Mapping* 32 (1): 127–40. doi:10.1002/hbm.21006.

Klose, Uwe. 1990. "In Vivo Proton Spectroscopy in Presence of Eddy Currents." *Magnetic Resonance in Medicine* 14 (1). Wiley-Blackwell: 26–30. doi:10.1002/mrm.1910140104.

Knot, H J, and M T Nelson. 1998. "Regulation of Arterial Diameter and Wall [Ca2+] in Cerebral Arteries of Rat by Membrane Potential and Intravascular Pressure." *The Journal of Physiology* 508 (Pt 1) (April): 199–209. http://www.ncbi.nlm.nih.gov/pubmed/9490839.

Knot, H J, P A Zimmermann, and M T Nelson. 1996. "Extracellular K(+)-Induced Hyperpolarizations and Dilatations of Rat Coronary and Cerebral Arteries Involve Inward Rectifier K(+) Channels." *The Journal of Physiology* 492 (Pt 2) (April): 419–30. http://www.ncbi.nlm.nih.gov/pubmed/9019539.

Kowiański, Przemysław, Grażyna Lietzau, Aleksandra Steliga, Monika Waśkow, and Janusz Moryś. 2013. "The Astrocytic Contribution to Neurovascular Coupling – Still More Questions than Answers?" *Neuroscience Research* 75 (3): 171–83. doi:10.1016/j.neures.2013.01.014.

Kreis, R. 1997. "Quantitative Localized 1H MR Spectroscopy for Clinical Use." *Progress in Nuclear Magnetic Resonance Spectroscopy* 31 (2–3): 155–95. doi:10.1016/S0079-6565(97)00014-9.

Kreis, Roland. 2004. "Issues of Spectral Quality in clinical1H-Magnetic Resonance Spectroscopy and a Gallery of Artifacts." *NMR in Biomedicine* 17 (6): 361–81. doi:10.1002/nbm.891.

Landau, William M, Walter H Jr Freygang, Lewis P Roland, Louis Sokoloff, and Seymour S Kety. 1955. "The Local Circulation of the Living Brain; Values in the Unanesthetized and Anesthetized Cat." *Trans Am Neurol Assoc* 80 (125): 125–29. http://www.ncbi.nlm.nih.gov/pubmed/13312020.

Lassen, N.A., K. Hoedt-Rasmussen, S.C. Sorenson, E. Skinhoj, S. Cronquist, B. Bodforss, and D.H.

Ingvar. 1963. “Regional Cerebral Blood Flow in Man Determined by Krypton.” *Neurology* 13 (9). Wolters Kluwer Health, Inc. on behalf of the American Academy of Neurology: 719–27. doi:10.1212/WNL.13.9.719.

Lauritzen, Martin, Claus Mathiesen, Katharina Schaefer, and Kirsten J. Thomsen. 2012. “Neuronal Inhibition and Excitation, and the Dichotomic Control of Brain Hemodynamic and Oxygen Responses.” *NeuroImage* 62 (2). Academic Press: 1040–50. doi:10.1016/J.NEUROIMAGE.2012.01.040.

Lauritzern, Martin J. 2005. “Reading Vascular Changes in Brain Imaging: Is Dendritic Calcium the Key?” *Journal of Cerebral Blood Flow & Metabolism* 25 (1_suppl): S684–S684. doi:10.1038/sj.jcbfm.9591524.0684.

Lauterbur, P. C. 1973. “Image Formation by Induced Local Interactions: Examples Employing Nuclear Magnetic Resonance.” *Nature* 242 (5394): 190–91. doi:10.1038/242190a0.

Lecrux, C., and E. Hamel. 2011. “The Neurovascular Unit in Brain Function and Disease.” *Acta Physiologica* 203 (1). Blackwell Publishing Ltd: 47–59. doi:10.1111/j.1748-1716.2011.02256.x.

Li, Shizhe, Bernard J. Dardzinski, Christopher M. Collins, Qing X. Yang, and Michael B. Smith. 1996. “Three-Dimensional Mapping of the Static Magnetic Field inside the Human Head.” *Magnetic Resonance in Medicine* 36 (5). Wiley Subscription Services, Inc., A Wiley Company: 705–14. doi:10.1002/mrm.1910360509.

Lin, A.-L., P. T. Fox, J. Hardies, T. Q. Duong, and J.-H. Gao. 2010. “Nonlinear Coupling between Cerebral Blood Flow, Oxygen Consumption, and ATP Production in Human Visual Cortex.” *Proceedings of the National Academy of Sciences* 107 (18): 8446–51. doi:10.1073/pnas.0909711107.

Lin, Yan, Mary C Stephenson, Lijing Xin, Antonio Napolitano, and Peter G Morris. 2012. “Investigating the Metabolic Changes due to Visual Stimulation Using Functional Proton Magnetic Resonance Spectroscopy at 7 T.” *Journal of Cerebral Blood Flow and Metabolism : Official Journal of the International Society of Cerebral Blood Flow and Metabolism* 32 (8): 1484–95. doi:10.1038/jcbfm.2012.33.

Lindauer, U, D Megow, H Matsuda, and U Dirnagl. 1999. “Nitric Oxide: A Modulator, but Not a Mediator, of Neurovascular Coupling in Rat Somatosensory Cortex.” *The American Journal of Physiology* 277 (2 Pt 2): H799-811. http://www.ncbi.nlm.nih.gov/pubmed/10444508.

Lisman, John. 2015. “The Challenge of Understanding the Brain: Where We Stand in 2015.” *Neuron* 86 (4). NIH Public Access: 864–82. doi:10.1016/j.neuron.2015.03.032.

Logothetis, Nikos K. 2002. “The Neural Basis of the Blood-Oxygen-Level-Dependent Functional Magnetic Resonance Imaging Signal.” *Philos Trans R Soc Lond B Biol Sci* 357 (1424): 1003–37. doi:10.1098/rstb.2002.1114.

Logothetis, Nikos K. 2008. “What We Can Do and What We Cannot Do with fMRI.” *Nature Reviews*

Neuroscience 453 (June): 869–78. doi:10.1038/nature06976.

———. 2010. "Neurovascular Uncoupling: Much Ado about Nothing." *Frontiers in Neuroenergetics* 2 (June). Frontiers Media SA: 1–4. doi:10.3389/fnene.2010.00002.

Logothetis, Nikos K., and Brian A. Wandell. 2004. "Interpreting the BOLD Signal." *Annual Review of Physiology* 66 (1): 735–69. doi:10.1146/annurev.physiol.66.082602.092845.

Lourenço, Cátia F., Ana Ledo, Rui M. Barbosa, and João Laranjinha. 2017. "Neurovascular-Neuroenergetic Coupling Axis in the Brain: Master Regulation by Nitric Oxide and Consequences in Aging and Neurodegeneration." *Free Radical Biology and Medicine* 108 (July): 668–82. doi:10.1016/j.freeradbiomed.2017.04.026.

Lukkarinen, J, J M Oja, M Turunen, and R A Kauppinen. 1997. "Quantitative Determination of Glutamate Turnover by 1H-Observed, 13C-Edited Nuclear Magnetic Resonance Spectroscopy in the Cerebral Cortex Ex Vivo: Interrelationships with Oxygen Consumption." *Neurochemistry International* 31 (1): 95–104. http://www.ncbi.nlm.nih.gov/pubmed/9185169.

Ma, J, C Ayata, P L Huang, M C Fishman, and M A Moskowitz. 1996. "Regional Cerebral Blood Flow Response to Vibrissal Stimulation in Mice Lacking Type I NOS Gene Expression." *The American Journal of Physiology* 270 (3 Pt 2): H1085-90. http://www.ncbi.nlm.nih.gov/pubmed/8780207.

Maddock, Richard J, Michael H Buonocore, Shawn P Lavoie, Linda E Copeland, Shawn J Kile, Anne L Richards, and John M Ryan. 2006. "Brain Lactate Responses during Visual Stimulation in Fasting and Hyperglycemic Subjects: A Proton Magnetic Resonance Spectroscopy Study at 1.5 Tesla." *Psychiatry Research* 148 (1). NIH Public Access: 47–54. doi:10.1016/j.pscychresns.2006.02.004.

Madsen, Peter Lund, Nancy F. Cruz, Louis Sokoloff, and Gerald A. Dienel. 1999. "Cerebral Oxygen/Glucose Ratio Is Low during Sensory Stimulation and Rises above Normal during Recovery: Excess Glucose Consumption during Stimulation Is Not Accounted for by Lactate Efflux from or Accumulation in Brain Tissue." *Journal of Cerebral Blood Flow & Metabolism* 19 (4): 393–400. doi:10.1097/00004647-199904000-00005.

Magistretti, Pierre J., and Igor Allaman. 2015. "A Cellular Perspective on Brain Energy Metabolism and Functional Imaging." *Neuron* 86 (4): 883–901. doi:10.1016/j.neuron.2015.03.035.

Mangia, Silvia, Federico Giove, and Mauro DiNuzzo. 2012. "Metabolic Pathways and Activity-Dependent Modulation of Glutamate Concentration in the Human Brain." *Neurochemical Research* 37 (11): 2554–61. doi:10.1007/s11064-012-0848-4.

Mangia, Silvia, Federico Giove, Ivan Tkáč, Nikos K Logothetis, Pierre-Gilles Henry, Cheryl A Olman, Bruno Maraviglia, Francesco Di Salle, and Kâmil Uğurbil. 2009. "Metabolic and Hemodynamic Events after Changes in Neuronal Activity: Current Hypotheses, Theoretical

Predictions and *in Vivo* NMR Experimental Findings." *Journal of Cerebral Blood Flow & Metabolism* 29 (3): 441–63. doi:10.1038/jcbfm.2008.134.

Mangia, Silvia, Ivan Tkáč, Rolf Gruetter, Pierre-Francois Van De Moortele, Federico Giove, Bruno Maraviglia, and Kâmil Uğurbil. 2006. "Sensitivity of Single-Voxel 1H-MRS in Investigating the Metabolism of the Activated Human Visual Cortex at 7 T." *Magnetic Resonance Imaging* 24 (4): 343–48. doi:10.1016/j.mri.2005.12.023.

Mangia, Silvia, Ivan Tkác, Rolf Gruetter, Pierre-Francois Van De Moortele, Bruno Maraviglia, Kâmil Uğurbil, Ivan Tkáč, et al. 2007. "Sustained Neuronal Activation Raises Oxidative Metabolism to a New Steady-State Level: Evidence from 1H NMR Spectroscopy in the Human Visual Cortex." *Journal of Cerebral Blood Flow and Metabolism : Official Journal of the International Society of Cerebral Blood Flow and Metabolism* 27 (5): 1055–63. doi:10.1038/sj.jcbfm.9600401.

Mangia, Silvia, Ivan Tkáč, Nikos K. Logothetis, Rolf Gruetter, Pierre Francois Van De Moortele, and Kâmil Uğurbil. 2007. "Dynamics of Lactate Concentration and Blood Oxygen Level-Dependent Effect in the Human Visual Cortex during Repeated Identical Stimuli." *Journal of Neuroscience Research* 85 (15). Wiley Subscription Services, Inc., A Wiley Company: 3340–46. doi:10.1002/jnr.21371.

Mansfield, P. 1977. "Multi-Planar Image Formation Using NMR Spin Echoes." *Journal of Physics C: Solid State Physics* 10 (3). IOP Publishing: L55–58. doi:10.1088/0022-3719/10/3/004.

Marques, José P., Tobias Kober, Gunnar Krueger, Wietske van der Zwaag, Pierre-François Van de Moortele, and Rolf Gruetter. 2010. "MP2RAGE, a Self Bias-Field Corrected Sequence for Improved Segmentation and T1-Mapping at High Field." *NeuroImage* 49 (2): 1271–81. doi:10.1016/j.neuroimage.2009.10.002.

Maudsley, A A, H E Simon, and S K Hilal. 1984. "Magnetic Field Measurement by NMR Imaging." *Journal of Physics E: Scientific Instruments* 17 (3). IOP Publishing: 216–20. doi:10.1088/0022-3735/17/3/013.

Maycox, Peter R., Johannes W. Hell, and Reinhard Jahn. 1990. "Amino Acid Neurotransmission: Spotlight on Synaptic Vesicles." *Trends in Neurosciences* 13 (3). Elsevier Current Trends: 83–87. doi:10.1016/0166-2236(90)90178-D.

McCarron, J G, and W Halpern. 1990. "Potassium Dilates Rat Cerebral Arteries by Two Independent Mechanisms." *The American Journal of Physiology* 259 (3 Pt 2): H902-8. http://www.ncbi.nlm.nih.gov/pubmed/2168682.

McKenna, Mary C., Helle S. Waagepetersen, Arne Schousboe, and Ursula Sonnewald. 2006. "Neuronal and Astrocytic Shuttle Mechanisms for Cytosolic-Mitochondrial Transfer of Reducing Equivalents: Current Evidence and Pharmacological Tools." *Biochemical Pharmacology* 71 (4). Elsevier: 399–407. doi:10.1016/J.BCP.2005.10.011.

McMahon, Harvey T., and David G. Nicholls. 1991. “The Bioenergetics of Neurotransmitter Release.” *Biochimica et Biophysica Acta (BBA) - Bioenergetics* 1059 (3). Elsevier: 243–64. doi:10.1016/S0005-2728(05)80210-5.

Mekle, Ralf, Simone Kühn, Harald Pfeiffer, Semiha Aydin, Florian Schubert, and Bernd Ittermann. 2017. “Detection of Metabolite Changes in Response to a Varying Visual Stimulation Paradigm Using Short-TE 1H MRS at 7 T.” *NMR in Biomedicine* 30 (2): e3672. doi:10.1002/nbm.3672.

Metea, Monica R., and Eric A. Newman. 2006. “Glial Cells Dilate and Constrict Blood Vessels: A Mechanism of Neurovascular Coupling.” *Journal of Neuroscience* 26 (11). http://www.jneurosci.org/content/26/11/2862.

Metere, Riccardo, Tobias Kober, Harald E. Möller, and Andreas Schäfer. 2017. “Simultaneous Quantitative MRI Mapping of T1, T2* and Magnetic Susceptibility with Multi-Echo MP2RAGE.” Edited by Vince Grolmusz. *PLOS ONE* 12 (1). Public Library of Science: e0169265. doi:10.1371/journal.pone.0169265.

Mintun, M a, B N Lundstrom, a Z Snyder, a G Vlassenko, G L Shulman, and M E Raichle. 2001. “Blood Flow and Oxygen Delivery to Human Brain during Functional Activity: Theoretical Modeling and Experimental Data.” *Proceedings of the National Academy of Sciences of the United States of America*. doi:10.1073/pnas.111164398.

Mlynárik, Vladimír, Giulio Gambarota, Hanne Frenkel, and Rolf Gruetter. 2006. “Localized Short-Echo-Time Proton MR Spectroscopy with Full Signal-Intensity Acquisition.” *Magnetic Resonance in Medicine* 56 (5). Wiley Subscription Services, Inc., A Wiley Company: 965–70. doi:10.1002/mrm.21043.

Moonen, Chrit T.W, and Peter C.M Van Zijl. 1990. “Highly Effective Water Suppression for in Vivo Proton NMR Spectroscopy (DRYSTEAM).” *Journal of Magnetic Resonance (1969)* 88 (1). Academic Press: 28–41. doi:10.1016/0022-2364(90)90106-J.

Mosso, Angelo, and Luis Simarro Lacabra. 1881. *Ueber Den Kreislauf Des Blutes Im Menschlichen Gehirn*. Leipzig: Veit. http://www.worldcat.org/title/ueber-den-kreislauf-des-blutes-im-menschlichen-gehirn-untersuchungen/oclc/716184253.

Mulligan, Sean J., and Brian A. MacVicar. 2004. “Calcium Transients in Astrocyte Endfeet Cause Cerebrovascular Constrictions.” *Nature* 431 (7005): 195–99. doi:10.1038/nature02827.

Mullinger, K.J., S.D. Mayhew, A.P. Bagshaw, R. Bowtell, and S.T. Francis. 2014. “Evidence That the Negative BOLD Response Is Neuronal in Origin: A Simultaneous EEG–BOLD–CBF Study in Humans.” *NeuroImage* 94 (July): 263–74. doi:10.1016/j.neuroimage.2014.02.029.

Mullins, Paul G., David J. McGonigle, Ruth L. O’Gorman, Nicolaas A.J. Puts, Rishma Vidyasagar, C. John Evans, Richard A.E. Edden, and Richard A E Edden. 2014. “Current Practice in the

Use of MEGA-PRESS Spectroscopy for the Detection of GABA." *NeuroImage* 86 (February): 43–52. doi:10.1016/j.neuroimage.2012.12.004.

Muthukumaraswamy, Suresh D., C. John Evans, Richard A.E. Edden, Richard G. Wise, and Krish D. Singh. 2012. "Individual Variability in the Shape and Amplitude of the BOLD-HRF Correlates with Endogenous GABAergic Inhibition." *Human Brain Mapping* 33 (2). Wiley Subscription Services, Inc., A Wiley Company: 455–65. doi:10.1002/hbm.21223.

Muthukumaraswamy, Suresh D, Richard A E Edden, Derek K Jones, Jennifer B Swettenham, and Krish D Singh. 2009. "Resting GABA Concentration Predicts Peak Gamma Frequency and fMRI Amplitude in Response to Visual Stimulation in Humans." *Proceedings of the National Academy of Sciences of the United States of America* 106 (20). National Academy of Sciences: 8356–61. doi:10.1073/pnas.0900728106.

Navarrete, Marta, Gertrudis Perea, David Fernandez de Sevilla, Marta Gómez-Gonzalo, Angel Núñez, Eduardo D. Martín, and Alfonso Araque. 2012. "Astrocytes Mediate In Vivo Cholinergic-Induced Synaptic Plasticity." Edited by Peter Scheiffele. *PLoS Biology* 10 (2): e1001259. doi:10.1371/journal.pbio.1001259.

Neale, Joseph H., Rafal T. Olszewski, Daiying Zuo, Karolina J. Janczura, Caterina P. Profaci, Kaleen M. Lavin, John C. Madore, and Tomasz Bzdega. 2011. "Advances in Understanding the Peptide Neurotransmitter NAAG and Appearance of a New Member of the NAAG Neuropeptide Family." *Journal of Neurochemistry* 118 (4). NIH Public Access: 490–98. doi:10.1111/j.1471-4159.2011.07338.x.

Newton, Jennifer M., Alan Sunderland, and Penny A. Gowland. 2005. "fMRI Signal Decreases in Ipsilateral Primary Motor Cortex during Unilateral Hand Movements Are Related to Duration and Side of Movement." *NeuroImage* 24 (4): 1080–87. doi:10.1016/j.neuroimage.2004.10.003.

Nicholson, C, and E Syková. 1998. "Extracellular Space Structure Revealed by Diffusion Analysis." *Trends in Neurosciences* 21 (5). Elsevier: 207–15. doi:10.1016/S0166-2236(98)01261-2.

Offenhauser, Nikolas, Kirsten Thomsen, Kirsten Caesar, and Martin Lauritzen. 2005. "Activity-Induced Tissue Oxygenation Changes in Rat Cerebellar Cortex: Interplay of Postsynaptic Activation and Blood Flow." *The Journal of Physiology* 565 (1): 279–94. doi:10.1113/jphysiol.2005.082776.

Ogawa, S, and T M Lee. 1990. "Magnetic Resonance Imaging of Blood Vessels at High Fields: In Vivo and in Vitro Measurements and Image Simulation." *Magnetic Resonance in Medicine : Official Journal of the Society of Magnetic Resonance in Medicine / Society of Magnetic Resonance in Medicine* 16 (1). Wiley Subscription Services, Inc., A Wiley Company: 9–18. doi:10.1002/mrm.1910160103.

Ogawa, S, T M Lee, A R Kay, and D W Tank. 1990. "Brain Magnetic Resonance Imaging with Contrast Dependent on Blood Oxygenation." *Proceedings of the National Academy of Sciences of the United States of America* 87 (24). National Academy of Sciences: 9868–72. doi:10.1073/pnas.87.24.9868.

Ogawa, S, T M Lee, A S Nayak, and P Glynn. 1990. "Oxygenation-Sensitive Contrast in Magnetic Resonance Image of Rodent Brain at High Magnetic Fields." *Magnetic Resonance in Medicine* 14 (1): 68–78. doi:10.1002/mrm.1910140108.

Ogg, R.J., R.B. Kingsley, and J.S. Taylor. 1994. "WET, a T1- and B1-Insensitive Water-Suppression Method for in Vivo Localized 1H NMR Spectroscopy." *Journal of Magnetic Resonance, Series B* 104 (1). Academic Press: 1–10. doi:10.1006/jmrb.1994.1048.

Orringer, Daniel A, David R Vago, and Alexandra J Golby. 2012. "Clinical Applications and Future Directions of Functional MRI." *Seminars in Neurology* 32 (4). NIH Public Access: 466–75. doi:10.1055/s-0032-1331816.

Öz, Gülin, Jeffry R. Alger, Peter B. Barker, Robert Bartha, Alberto Bizzi, Chris Boesch, Patrick J. Bolan, et al. 2014. "Clinical Proton MR Spectroscopy in Central Nervous System Disorders." *Radiology* 270 (3): 658–79. doi:10.1148/radiol.13130531.

Öz, Gülin, and Ivan Tkáč. 2011. "Short-Echo, Single-Shot, Full-Intensity Proton Magnetic Resonance Spectroscopy for Neurochemical Profiling at 4 T: Validation in the Cerebellum and Brainstem." *Magnetic Resonance in Medicine* 65 (4): 901–10. doi:10.1002/mrm.22708.

Pasley, Brian N., Ben A. Inglis, and Ralph D. Freeman. 2007. "Analysis of Oxygen Metabolism Implies a Neural Origin for the Negative BOLD Response in Human Visual Cortex." *NeuroImage*. doi:10.1016/j.neuroimage.2006.09.015.

Paulson, Olaf B, Steen G Hasselbalch, Egill Rostrup, Gitte Moos Knudsen, and Dale Pelligrino. 2010. "Cerebral Blood Flow Response to Functional Activation." *Journal of Cerebral Blood Flow & Metabolism* 30 (1): 2–14. doi:10.1038/jcbfm.2009.188.

Pellerin, L, and P J Magistretti. 1994. "Glutamate Uptake into Astrocytes Stimulates Aerobic Glycolysis: A Mechanism Coupling Neuronal Activity to Glucose Utilization." *Proceedings of the National Academy of Sciences of the United States of America* 91 (22): 10625–29. http://www.ncbi.nlm.nih.gov/pubmed/7938003.

Pellerin, Luc, and Pierre J Magistretti. 2012. "Sweet Sixteen for ANLS." *Journal of Cerebral Blood Flow and Metabolism : Official Journal of the International Society of Cerebral Blood Flow and Metabolism* 32 (7). SAGE Publications: 1152–66. doi:10.1038/jcbfm.2011.149.

Peng, Xinqi, Juan R. Carhuapoma, Anish Bhardwaj, Nabil J. Alkayed, John R. Falck, David R. Harder, Richard J. Traystman, and Raymond C. Koehler. 2002. "Suppression of Cortical Functional Hyperemia to Vibrissal Stimulation in the Rat by Epoxygenase Inhibitors."

American Journal of Physiology - Heart and Circulatory Physiology 283 (5): H2029–37. doi:10.1152/ajpheart.01130.2000.

Peng, Xinqi, Chenyang Zhang, Nabil J. Alkayed, David R. Harder, and Raymond C. Koehler. 2004. "Dependency of Cortical Functional Hyperemia to Forepaw Stimulation on Epoxygenase and Nitric Oxide Synthase Activities in Rats." *Journal of Cerebral Blood Flow & Metabolism* 24 (5): 509–17. doi:10.1097/00004647-200405000-00004.

Perea, Gertrudis, Marta Navarrete, and Alfonso Araque. 2009. "Tripartite Synapses: Astrocytes Process and Control Synaptic Information." *Trends in Neurosciences* 32 (8): 421–31. doi:10.1016/j.tins.2009.05.001.

Petzold, Gabor C, Dinu F Albeanu, Tomokazu F Sato, and Venkatesh N Murthy. 2008. "Coupling of Neural Activity to Blood Flow in Olfactory Glomeruli Is Mediated by Astrocytic Pathways." *Neuron* 58 (6). NIH Public Access: 897–910. doi:10.1016/j.neuron.2008.04.029.

Phillips, Aaron A, Franco HN Chan, Mei Mu Zi Zheng, Andrei V Krassioukov, and Philip N Ainslie. 2015. "Neurovascular Coupling in Humans: Physiology, Methodological Advances and Clinical Implications." *Journal of Cerebral Blood Flow and Metabolism : Official Journal of the International Society of Cerebral Blood Flow and Metabolism* 36 (4): 0271678X15617954. doi:10.1177/0271678X15617954.

Pohmann, Rolf, Oliver Speck, and Klaus Scheffler. 2016. "Signal-to-Noise Ratio and MR Tissue Parameters in Human Brain Imaging at 3, 7, and 9.4 Tesla Using Current Receive Coil Arrays." *Magnetic Resonance in Medicine* 75 (2): 801–9. doi:10.1002/mrm.25677.

Porter, J T, and K D McCarthy. 1996. "Hippocampal Astrocytes in Situ Respond to Glutamate Released from Synaptic Terminals." *The Journal of Neuroscience : The Official Journal of the Society for Neuroscience* 16 (16): 5073–81. http://www.ncbi.nlm.nih.gov/pubmed/8756437.

Powers, W J, I B Hirsch, and P E Cryer. 1996. "Effect of Stepped Hypoglycemia on Regional Cerebral Blood Flow Response to Physiological Brain Activation." *Am J Physiol*.

Pradhan, Subechhya, Susanne Bonekamp, Joseph S. Gillen, Laura M. Rowland, S. Andrea Wijtenburg, Richard A.E. Edden, and Peter B. Barker. 2015. "Comparison of Single Voxel Brain MRS AT 3T and 7T Using 32-Channel Head Coils." *Magnetic Resonance Imaging* 33 (8). Elsevier: 1013–18. doi:10.1016/j.mri.2015.06.003.

Prichard, J, D Rothman, E Novotny, O Petroff, T Kuwabara, M Avison, A Howseman, C Hanstock, and R Shulman. 1991. "Lactate Rise Detected by 1H NMR in Human Visual Cortex during Physiologic Stimulation." *Proceedings of the National Academy of Sciences of the United States of America* 88 (13). National Academy of Sciences: 5829–31. doi:10.1073/PNAS.88.13.5829.

Provencher, S W. 1993. "Estimation of Metabolite Concentrations from Localized in Vivo Proton NMR Spectra." *Magnetic Resonance in Medicine : Official Journal of the Society of Magnetic*

Resonance in Medicine / Society of Magnetic Resonance in Medicine 30 (6): 672–79.

Purcell, E. M., H. C. Torrey, and R. V. Pound. 1946. "Resonance Absorption by Nuclear Magnetic Moments in a Solid." *Physical Review* 69 (1–2). American Physical Society: 37–38. doi:10.1103/PhysRev.69.37.

Puro, Donald G. 2007. "Physiology and Pathobiology of the Pericyte-Containing Retinal Microvasculature: New Developments." *Microcirculation* 14 (1): 1–10. doi:10.1080/10739680601072099.

Raichle, M E. 1998. "Behind the Scenes of Functional Brain Imaging: A Historical and Physiological Perspective." *Proceedings of the National Academy of Sciences* 95 (3): 765–72. doi:10.1073/pnas.95.3.765.

Rodgers, Christopher T., and Matthew D. Robson. 2010. "Receive Array Magnetic Resonance Spectroscopy: Whitened Singular Value Decomposition (WSVD) Gives Optimal Bayesian Solution." *Magnetic Resonance in Medicine* 63 (4). Wiley Subscription Services, Inc., A Wiley Company: 881–91. doi:10.1002/mrm.22230.

Rothman, Douglas L, Henk M De Feyter, Robin A de Graaf, Graeme F Mason, and Kevin L Behar. 2011. "13C MRS Studies of Neuroenergetics and Neurotransmitter Cycling in Humans." *NMR in Biomedicine* 24 (8). NIH Public Access: 943–57. doi:10.1002/nbm.1772.

Roy, C S, and C S Sherrington. 1890. "On the Regulation of the Blood-Supply of the Brain." *Journal of Physiology-Paris* 11 (1–2). Wiley-Blackwell: 85--158.17. http://eutils.ncbi.nlm.nih.gov/entrez/eutils/elink.fcgi?dbfrom=pubmed&id=16991945&retmode=ref&cmd=prlinks.

Sahara, Setsuko, Yuchio Yanagawa, Dennis D M O'Leary, and Charles F Stevens. 2012. "The Fraction of Cortical GABAergic Neurons Is Constant from near the Start of Cortical Neurogenesis to Adulthood." *The Journal of Neuroscience : The Official Journal of the Society for Neuroscience* 32 (14). NIH Public Access: 4755–61. doi:10.1523/JNEUROSCI.6412-11.2012.

Sappey-Marinier, D, G Calabrese, G Fein, J W Hugg, C Biggins, and M W Weiner. 1992. "Effect of Photic Stimulation on Human Visual Cortex Lactate and Phosphates Using 1H and 31P Magnetic Resonance Spectroscopy." *Journal of Cerebral Blood Flow and Metabolism : Official Journal of the International Society of Cerebral Blood Flow and Metabolism* 12 (4): 584–92. doi:10.1038/jcbfm.1992.82.

Schaller, Benoît, Ralf Mekle, Lijing Xin, Nicolas Kunz, and Rolf Gruetter. 2013. "Net Increase of Lactate and Glutamate Concentration in Activated Human Visual Cortex Detected with Magnetic Resonance Spectroscopy at 7 Tesla." *Journal of Neuroscience Research* 91 (8): 1076–83. doi:10.1002/jnr.23194.

Schaller, Benoît, Lijing Xin, Kieran O'Brien, Arthur W. Magill, and Rolf Gruetter. 2014. "Are

Glutamate and Lactate Increases Ubiquitous to Physiological Activation? A 1H Functional MR Spectroscopy Study during Motor Activation in Human Brain at 7Tesla." *NeuroImage* 93 (P1). Academic Press: 138–45. doi:10.1016/j.neuroimage.2014.02.016.

Scheenen, Tom W. J., Dennis W. J. Klomp, Jannie P. Wijnen, and Arend Heerschap. 2008. "Short Echo time1H-MRSI of the Human Brain at 3T with Minimal Chemical Shift Displacement Errors Using Adiabatic Refocusing Pulses." *Magnetic Resonance in Medicine* 59 (1): 1–6. doi:10.1002/mrm.21302.

Schlenke, Jan, Lars Hildebrand, Susanne Felsinger, Bernd Reusch, and Lothar Brecker. 2013. "Automated Signal Detection as Tool to Evaluate Magnetic Field Homogeneity from Fourier Transformed Proton NMR Spectra." *Applied Magnetic Resonance* 44 (6). Springer Vienna: 745–58. doi:10.1007/s00723-013-0442-1.

Schulz, Kristina, Esther Sydekum, Roland Krueppel, Christoph J Engelbrecht, Felix Schlegel, Aileen Schröter, Markus Rudin, and Fritjof Helmchen. 2012. "Simultaneous BOLD fMRI and Fiber-Optic Calcium Recording in Rat Neocortex." *Nature Methods* 9 (6): 597–602. doi:10.1038/nmeth.2013.

Schummers, J., H. Yu, and M. Sur. 2008. "Tuned Responses of Astrocytes and Their Influence on Hemodynamic Signals in the Visual Cortex." *Science* 320 (5883): 1638–43. doi:10.1126/science.1156120.

Seifert, Frank, Gerd Wübbeler, Sven Junge, Bernd Ittermann, and Herbert Rinneberg. 2007. "Patient Safety Concept for Multichannel Transmit Coils." *Journal of Magnetic Resonance Imaging* 26 (5). Wiley Subscription Services, Inc., A Wiley Company: 1315–21. doi:10.1002/jmri.21149.

Sengupta, Saikat, E. Brian Welch, Yansong Zhao, David Foxall, Piotr Starewicz, Adam W. Anderson, John C. Gore, and Malcolm J. Avison. 2011. "Dynamic B0 Shimming at 7 T." *Magnetic Resonance Imaging* 29 (4). Elsevier: 483–96. doi:10.1016/J.MRI.2011.01.002.

Serebryakov, V, S Zakharenko, V Snetkov, and K Takeda. 1994. "Effects of Prostaglandins E1 and E2 on Cultured Smooth Muscle Cells and Strips of Rat Aorta." *Prostaglandins* 47 (5): 353–65. http://www.ncbi.nlm.nih.gov/pubmed/8066184.

Shepherd, G.M. 2004. *The Synaptic Organization of the Brain*. *Journal of Psychiatry and Neuroscience*. Vol. 5th ed. doi:10.1093/acprof.

Shmuel, Amir, Mark Augath, Axel Oeltermann, and Nikos K Logothetis. 2006. "Negative Functional MRI Response Correlates with Decreases in Neuronal Activity in Monkey Visual Area V1." *Nature Neuroscience* 9 (4). Nature Publishing Group: 569–77. doi:10.1038/nn1675.

Shmuel, Amir, Essa Yacoub, Josef Pfeuffer, Pierre-Francois Van de Moortele, Gregor Adriany, Xiaoping Hu, and Kamil Ugurbil. 2002. "Sustained Negative BOLD, Blood Flow and Oxygen Consumption Response and Its Coupling to the Positive Response in the Human Brain."

Neuron 36 (6): 1195–1210. doi:10.1016/S0896-6273(02)01061-9.

Siegel, George J. 2006. *Basic Neurochemistry : Molecular, Cellular and Medical Aspects*. Elsevier.

Sirotin, Yevgeniy B, and Aniruddha Das. 2009. "Anticipatory Haemodynamic Signals in Sensory Cortex Not Predicted by Local Neuronal Activity." *Nature* 457 (7228): 475–79. doi:10.1038/nature07664.

Smith, Andrew T., Adrian L. Williams, and Krishna D. Singh. 2004. "Negative BOLD in the Visual Cortex: Evidence against Blood Stealing." *Human Brain Mapping* 21 (4). Wiley Subscription Services, Inc., A Wiley Company: 213–20. doi:10.1002/hbm.20017.

Starck, G., Å. Carlsson, M. Ljungberg, and E. Forssell-Aronsson. 2009. "K-Space Analysis of Point-Resolved Spectroscopy (PRESS) with Regard to Spurious Echoes in *in Vivo* ^{1}H MRS." *NMR in Biomedicine* 22 (2): 137–47. doi:10.1002/nbm.1289.

Stefanovic, Bojana, Jan M Warnking, and G.Bruce Pike. 2004. "Hemodynamic and Metabolic Responses to Neuronal Inhibition." *NeuroImage* 22 (2): 771–78. doi:10.1016/j.neuroimage.2004.01.036.

Stelzer, Johannes, Gabriele Lohmann, Karsten Mueller, Tilo Buschmann, and Robert Turner. 2014. "Deficient Approaches to Human Neuroimaging." *Frontiers in Human Neuroscience* 8 (July): 462. doi:10.3389/fnhum.2014.00462.

Takano, Takahiro, Guo-Feng Tian, Weiguo Peng, Nanhong Lou, Witold Libionka, Xiaoning Han, and Maiken Nedergaard. 2017. "Astrocyte-Mediated Control of Cerebral Blood Flow." Accessed August 21. doi:10.1038/nn1623.

Takata, N., T. Mishima, C. Hisatsune, T. Nagai, E. Ebisui, K. Mikoshiba, and H. Hirase. 2011. "Astrocyte Calcium Signaling Transforms Cholinergic Modulation to Cortical Plasticity In Vivo." *Journal of Neuroscience* 31 (49): 18155–65. doi:10.1523/JNEUROSCI.5289-11.2011.

Tian, R, P Vogel, N A Lassen, M J Mulvany, F Andreasen, and C Aalkjaer. 1995. "Role of Extracellular and Intracellular Acidosis for Hypercapnia-Induced Inhibition of Tension of Isolated Rat Cerebral Arteries." *Circulation Research* 76 (2): 269–75. doi:10.1161/01.RES.76.2.269.

Tkác, Ivan, Gülin Oz, Gregor Adriany, Kamil Uğurbil, and Rolf Gruetter. 2009. "In Vivo 1H NMR Spectroscopy of the Human Brain at High Magnetic Fields: Metabolite Quantification at 4T vs. 7T." *Magnetic Resonance in Medicine* 62 (4). NIH Public Access: 868–79. doi:10.1002/mrm.22086.

Tkáč, Ivan, Z. Starčuk, I. Y. Choi, and R. Gruetter. 1999. "In Vivo 1H NMR Spectroscopy of Rat Brain at 1 Ms Echo Time." *Magnetic Resonance in Medicine* 41 (4): 649–56. doi:10.1002/(SICI)1522-2594(199904)41:4<649::AID-MRM2>3.0.CO;2-G.

Tootell, Roger B.H, Nouchine Hadjikhani, E.Kevin Hall, Sean Marrett, Wim Vanduffel, J.Thomas

Vaughan, and Anders M Dale. 1998. "The Retinotopy of Visual Spatial Attention." *Neuron* 21 (6): 1409–22. doi:10.1016/S0896-6273(00)80659-5.

Volterra, Andrea, and Jacopo Meldolesi. 2005. "Astrocytes, from Brain Glue to Communication Elements: The Revolution Continues." *Nature Reviews Neuroscience* 6 (8): 626–40. doi:10.1038/nrn1722.

Wade, Alex R., and Jess Rowland. 2010. "Early Suppressive Mechanisms and the Negative Blood Oxygenation Level-Dependent Response in Human Visual Cortex." *Journal of Neuroscience* 30 (14): 5008–19. doi:10.1523/JNEUROSCI.6260-09.2010.

Walls, Anne B., Helle S. Waagepetersen, Lasse K. Bak, Arne Schousboe, and Ursula Sonnewald. 2015. "The Glutamine–Glutamate/GABA Cycle: Function, Regional Differences in Glutamate and GABA Production and Effects of Interference with GABA Metabolism." *Neurochemical Research* 40 (2). Springer US: 402–9. doi:10.1007/s11064-014-1473-1.

Wang, Xiaohai, Nanhong Lou, Qiwu Xu, Guo-Feng Tian, Wei Guo Peng, Xiaoning Han, Jian Kang, Takahiro Takano, and Maiken Nedergaard. 2006. "Astrocytic Ca2+ Signaling Evoked by Sensory Stimulation in Vivo." *Nature Neuroscience* 9 (6): 816–23. doi:10.1038/nn1703.

Weiger, Markus, Thomas Speck, and Michael Fey. 2006. "Gradient Shimming with Spectrum Optimisation." *Journal of Magnetic Resonance* 182 (1). Academic Press: 38–48. doi:10.1016/J.JMR.2006.06.006.

Williams, S. 1999. "Cerebral Amino Acids Studied by Nuclear Magnetic Resonance Spectroscopy in Vivo." *Progress in Nuclear Magnetic Resonance Spectroscopy* 34 (3–4). Pergamon: 301–26. doi:10.1016/S0079-6565(99)00004-7.

Woolsey, T A, C M Rovainen, S B Cox, M H Henegar, G E Liang, D Liu, Y E Moskalenko, J Sui, and L Wei. 2017. "Neuronal Units Linked to Microvascular Modules in Cerebral Cortex: Response Elements for Imaging the Brain." *Cerebral Cortex (New York, N.Y. : 1991)* 6 (5): 647–60. Accessed May 29. http://www.ncbi.nlm.nih.gov/pubmed/8921201.

y Cajal, S. 1897. "Algo Sobre La Significación Fisiológica de La Neuroglia." *Rev. Trimes. Microgr* 2: 33–47.

y Cajal, Santiago Ramón. 1895. *Algunas Conjeturas Sobre El Mecanismo Anatómico de La Ideación, Asociación Y Atención*.

Zaritsky, J J, D M Eckman, G C Wellman, M T Nelson, and T L Schwarz. 2000. "Targeted Disruption of Kir2.1 and Kir2.2 Genes Reveals the Essential Role of the Inwardly Rectifying K(+) Current in K(+)-Mediated Vasodilation." *Circulation Research* 87 (2): 160–66. http://www.ncbi.nlm.nih.gov/pubmed/10904001.

Zehendner, Christoph M, Hannah E Wedler, and Heiko J Luhmann. 2013. "A Novel in Vitro Model to Study Pericytes in the Neurovascular Unit of the Developing Cortex." *PloS One* 8 (11).

Public Library of Science: e81637. doi:10.1371/journal.pone.0081637.

Zonta, Micaela, María Cecilia Angulo, Sara Gobbo, Bernhard Rosengarten, Konstantin-A. Hossmann, Tullio Pozzan, and Giorgio Carmignoto. 2002. "Neuron-to-Astrocyte Signaling Is Central to the Dynamic Control of Brain Microcirculation." *Nature Neuroscience* 6 (1): 43–50. doi:10.1038/nn980.

Erklärung über die eigenständige Abfassung der Arbeit

Hiermit erkläre ich, dass ich die vorliegende Arbeit selbstständig und ohne unzulässige Hilfe oder Benutzung anderer als der angegebenen Hilfsmittel angefertigt habe. Ich versichere, dass Dritte von mir weder unmittelbar noch mittelbar eine Vergütung oder geldwerte Leistungen für Arbeiten erhalten haben, die im Zusammenhang mit dem Inhalt der vorgelegten Dissertation stehen, und dass die vorgelegte Arbeit weder im Inland noch im Ausland in gleicher oder ähnlicher Form einer anderen Prüfungsbehörde zum Zweck einer Promotion oder eines anderen Prüfungsverfahrens vorgelegt wurde. Alles aus anderen Quellen und von anderen Personen übernommene Material, das in der Arbeit verwendet wurde oder auf das direkt Bezug genommen wird, wurde als solches kenntlich gemacht. Insbesondere wurden alle Personen genannt, die direkt an der Entstehung der vorliegenden Arbeit beteiligt waren. Die aktuellen gesetzlichen Vorgaben in Bezug auf die Zulassung der klinischen Studien, die Bestimmungen des Tierschutzgesetzes, die Bestimmungen des Gentechnikgesetzes und die allgemeinen Datenschutzbestimmungen wurden eingehalten. Ich versichere, dass ich die Regelungen der Satzung der Universität Leipzig zur Sicherung guter wissenschaftlicher Praxis kenne und eingehalten habe.

....

Datum Unterschrift

Publications

8.1 Articles

1. **Miguel Martínez-Maestro**, Christian Labadie and Harald E. Möller. Dynamic Metabolic Changes in Human Visual Cortex in Regions with Positive and Negative BOLD Response. ***In preparation, submitted to JCBFM on April 13th 2018.***

8.2 Oral presentations

1. **Miguel Martínez-Maestro**, Christian Labadie, Ioannis Angelos Giapitzakis and Harald E. Möller. Dynamic changes of glutamate detected by functional MR spectroscopy in human visual cortex in regions with positive and negative BOLD response. *Proceedings of the 25th Annual Meeting of the International Society for Magnetic Resonance in Medicine (ISMRM), Honolulu, HI, USA, 2017.*

2. **M**iguel **Martínez-Maestro,** Christian Labadie, Karsten Müller and Harald E. Möller. Potential of 3T fMRS to detect dynamic changes of glutamate related to activation in visual cortex. *3rd Annual Meeting TRANSACT ITN, Nijmegen, Netherlands, 2016.*

3. **Miguel Martínez-Maestro,** Maria Guidi, Laurentius Huber, Štefan Holiga, Henrik Marschner, and Harald E. Möller. fMRS of visual cortex at 3T with periodic averaging of a block design paradigm. *Mid Term Review TRANSACT ITN, Barcelona, Spain, 2014.*

4. **Miguel Martínez-Maestro**, Pilar López-Larrubia. In vivo and ex vivo MR methodologies to assess the evolution of a traumatic brain injury model. *Proceedings of the 30th Annual Scientific Meeting of the European Society of Magnetic Resonance in Medicine and Biology (ESMRMB), Toulouse, France, 2013.*

5. **Miguel Martínez-Maestro**, Pilar López-Larrubia. Early functional and metabolic cerebral alterations in a traumatic brain injury rat model by Magnetic Resonance approaches. *Proceedings of the 29th Annual Scientific Meeting of the European Society of Magnetic Resonance in Medicine and Biology (ESMRMB), Lisbon, Portugal, 2012.*

8.3 Posters

1. **Miguel Martínez-Maestro,** Christian Labadie, Karsten Müller and Harald E. Möller. Potential of 3T fMRS to detect dynamic changes of glutamate related to activation in visual cortex. *Proceedings of the 24th Annual Meeting of the International Society for Magnetic Resonance in Medicine (ISMRM), Singapore, 2016.*

2. **Miguel Martínez-Maestro**, Maria Guidi, Laurentius Huber, Štefan Holiga, Henrik Marschner, and Harald E. Möller. fMRS of visual cortex at 3T with periodic averaging of a block design paradigm. *Proceedings of the 23rd Annual Meeting of the International Society for Magnetic Resonance in Medicine (ISMRM), Toronto, ON, Canada, 2015.*

3. **Miguel Martínez-Maestro**, Maria Guidi, Christian Labadie, and Harald E. Möller. Should beginners revisit the ancient and honourable art of shimming at high fields? *Proceedings of the 22nd Annual Meeting of the*

International Society for Magnetic Resonance in Medicine (ISMRM), Milano, Italy , 2014.

4. Christian Labadie, Tomas Siegert, Enrico Reimer, Maria Guidi, **Miguel Martínez-Maestro**, Harald E. Möller, Robert Turner, and Jessica Schulz. Adaptive motion correction of single-voxel spectroscopy with real-time frequency correction at 3T and 7T. *Proceedings of the 22nd Annual Meeting of the International Society for Magnetic Resonance in Medicine (ISMRM), Milano, Italy, 2014.*

5. **Miguel Martínez-Maestro** and Harald E. Möller. Problems with Water Suppression and Ghost Signals. *2nd TRANSACT Workshop: Quality Issues in Clinical MR Spectroscopy, Bern, Swizerland, 2014.*

6. **Miguel M Martínez-Maestro** and Pilar López-Larrubia. MRI study of a traumatic brain injury model from short to long time evolution. *Proceedings of the 28th Annual Scientific Meeting of the European Society of Magnetic Resonance in Medicine and Biology (ESMRMB), Leipzig, Germany, 2011.*

8.4 Awards and stipends

1. ISMRM Summa Cum Laude Merit Award for the conference talk: Dynamic changes of glutamate detected by functional MR spectroscopy in human visual cortex in regions with positive and negative BOLD response. 25th Annual Meeting of the International Society for Magnetic Resonance in Medicine (ISMRM), Honolulu, HI, USA, 2017.
2. ISMRM Magna cum Laude Merit Award for the conference poster: Should beginners revisit the ancient and honourable art of shimming at high fields? 22nd Annual Meeting of the International Society for Magnetic Resonance in Medicine (ISMRM), Milano, Italy, 2014.

3. MARIE CURIE Fellowship. Department 'Excellent Science', Research Executive Agency, European Commission, 2013.
4. ISMRM Trainee Educational Stipend, for the 24th Annual Meeting of the International Society for Magnetic Resonance in Medicine, Singapore, 2016.
5. ISMRM Trainee Educational Stipend, for the 23rd Annual Meeting of the International Society for Magnetic Resonance in Medicine, Toronto, ON, Canada, 2015.
6. ISMRM Trainee Educational Stipend, for the 22nd Annual Meeting of the International Society for Magnetic Resonance in Medicine, Milano, Italy, 2014.

8.5 Chapters in books

2. Pilar López-Larrubia, Eva Cañadillas-Cárdenas, Ana M. Metelo, Nuria Arias, **Miguel Martínez-Maestro** , Aire Salguero and Sebastián Cerdán. Electronic book: Advances in the biology, imaging and therapies for glioblastoma. Chapter: Magnetic Resonance Imaging of gliomas. *ISBN 979-953-307-197-7. INTECH. 2011. Clark C. Chen, M.D., Ph.D.*

Acknowledgments

Realizing this PhD has been a remarkable journey, and it wouldn't have been possible without the support from so many people that I was lucky to have by my side the full time or during some parts of it. I thank them all, but I would like to highlight a few below.

First, I would like to thank my supervisor and co-supervisor Prof. Dr. Hellmuth Obrig and Prof. Dr. Harald E. Möller for giving me the opportunity of performing this PhD. I thank Harald for the complete freedom given to develop my project in the directions I wanted and being always available for fruitful discussions. I also thank him for the continues motivation for pursuing the best quality of work. Under his supervision, I have grown professionally and personally. Secondly, I would like to thank my former college, Dr. Christian Labadie, for encouraging me to always strength my weak skills, learn by myself, and be independent. Also, I thank him for the training in the Siemens IDEA environment, the initial help with MATLAB and the interesting discussions about my project or any topic.

I would like to thank the full NMR and Neurophysics groups for the camaraderie during these years. Special thanks to Dr. Laurentius Huber for sharing part of the visual stimulation paradigms and the initial support for scanning at 7 T. Also, thanks to Dr. Jöran Lepsien and Dr. Karsten Müller, for the tips about SPM, and Domenica Wilfling, Anke Kummer, Simone Wipper, Mandy Jochemko, Silvie Neubert and Manuela Hofmann, for having always schedule and handle so efficiency every participant for the MR experiments. Also, I thank the participants, especially those most compliant that helped me to obtain good measurements.

I thank the ISMRM society, for such amazing conferences in Milan, Toronto, Singapore and Honolulu, that brought the opportunity to connect with scientist all around the world. Among my "ISMRM friends" I especially thank Dr. Ioannis-Angelos Giapitzakis and his supervisor Dr. Anke Henning from the MPI for Biological Cybernetics for advice on the post-processing of spectroscopy data, and Dr. Małgorzata Marjańska from the University of Minnesota CMRR for sharing the semi-LASER sequence.

I have to thank all my MPI lunch mates for hours of entertainment: Kornelius, Susanne, Tomáš, Jens, Franz, Jakob, Štefan, Robert… And especially Manoj, Kathrin, Tobias, Henrik and Maria, for the fun inside and outside the institute. Thanks to Henrik for the unforgettable moments in Asia and America. Also, thanks to Maria for being always a great moral support for my personal and professional life, my connection with my mother tongue in Germany, and for proofreading my dissertation.

I could not miss acknowledging the European Union for funding the TRANSACT ITN Project, where I found an amazing network of researchers. Among them, the ESRs, the other PhD candidates that became more than just colleagues: Saurabh, Claudio, Akila, Iveta, Victor, Nuno, Michal, Adrian, Nassim, Veronika, Ross, Pruthvi and Sana. Thanks to Nuno for the friendship and the company in the Big Island of Hawaii. Thanks to Michal for being such a good friend, always helpful, from mental motivation to basic programming assistance at the beginning. Thanks to Adrian for the memorable times in Croatia and for being there when my arm got broken. Most of all, thanks to *the cool guys* Nassim, Veronika and Ross, and to *the FPS* Pruthvi and Sana, for endless moments of joy, the vacations, the parties, and the love.

My life in Leipzig wouldn't have been the same without my beloved locals, especially Sebastian, Abel, Narumol, Kolja, Toyo (and Lio), Jarek (and Family), Simone, Fede, and my favorite german: Florian. I really thank him for the psychological help in the hard times, and the fun in the good ones.

Thanks to WhatsApp for helping to keep close those who are far, and thanks to those for staying with me through time and space. Thanks to my friends from Cuenca and Madrid: Carlos, Silvia, Antonio, Omar, Amanda, Aida and Mirian for the good moments. Thanks to Mirian for being my oldest and most loyal friend, for the continuous cheering, and for being always ready to come with me to any corner of the world. Thanks to my best friend from Vienna Marta, for the wonderful travels around Europe, and again, the mental support.

Finally, I thank my family, my best group of fans that make me feel like a Rockstar every time I come back to Spain: Angel, Mari Tere, Paula, Juan Pablo, Conchi, Pablo, Marta, Juan Antonio, Henar, Luci, Pepe and Sebe. Thanks to my sister Laura, a role model in science, that gave me advice when I was lost. And above all, thanks to my parents Jose Vicente and Gloria, for their unconditional love and support through my entire life to achieve any goal, and thanks to my Grandmother Eloisa, who would have loved to witness the end of my trip but sadly left us last October. Her love, memory and values will always live with me and I would like to dedicate this dissertation to her.